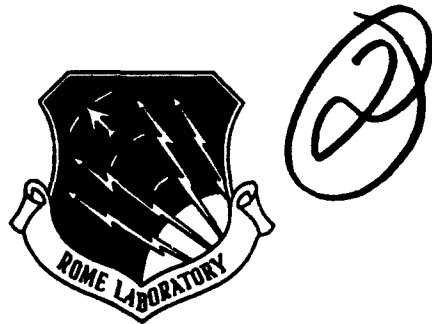


AD-A253 941



RL-TR-92-29
Final Technical Report
February 1992



MODELING OF HF PROPAGATION AND HEATING IN THE IONOSPHERE

TRW Space and Technology Group

Denise Hinkel, Merit Shoucri, Timothy Smith, Thomas Wagner



APPROVED FOR PUBLIC RELEASE; DISTRIBUTION UNLIMITED.

92-22318



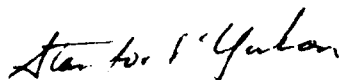
**Rome Laboratory
Air Force Systems Command
Griffiss Air Force Base, NY 13441-5700**

92 8 7 040

This report has been reviewed by the Rome Laboratory Public Affairs Office (PA) and is releasable to the National Technical Information Service (NTIS). At NTIS it will be releasable to the general public, including foreign nations.

RL-TR-92-29 has been reviewed and is approved for publication.

APPROVED:



STANFORD YUKON
Project Engineer

FOR THE COMMANDER:



JOHN K. SCHINDLER
Director
Electromagnetics & Reliability Directorate

If your address has changed or if you wish to be removed from the Rome Laboratory mailing list, or if the addressee is no longer employed by your organization, please notify RL(ERCP) Hanscom AFB MA 01731-5000. This will assist us in maintaining a current mailing list.

Do not return copies of this report unless contractual obligations or notices on a specific document require that it be returned.

REPORT DOCUMENTATION PAGE

Form Approved
OMB No. 0704-0188

Public reporting burden for this collection of information is estimated to average 1 hour per response, including the time for reviewing instructions, searching existing data sources, gathering and maintaining the data needed, and completing and reviewing the collection of information. Send comments regarding this burden estimate or any other aspect of this collection of information, including suggestions for reducing this burden, to Washington Headquarters Services, Directorate for Information Operations and Reports, 1215 Jefferson Davis Highway, Suite 1204, Arlington, VA 22202-4302, and to the Office of Management and Budget, Paperwork Reduction Project (0704-0188), Washington, DC 20503.

1. AGENCY USE ONLY (Leave Blank)		2. REPORT DATE February 1992	3. REPORT TYPE AND DATES COVERED Final Apr 89 - Nov 91
4. TITLE AND SUBTITLE MODELING OF HF PROPAGATION AND HEATING IN THE IONOSPHERE		5. FUNDING NUMBERS C - F19628-89-C-0031 PE - 62702F PR - 4600 TA - 16 WU - 32	
6. AUTHOR(S) Denise Hinkel, Merit Shoucri, Timothy Smith, Thomas Wagner		8. PERFORMING ORGANIZATION REPORT NUMBER N/A	
7. PERFORMING ORGANIZATION NAME(S) AND ADDRESS(ES) TRW Space and Technology Group Applied Technology Division One Space Park Redondo Beach CA 90278		9. SPONSORING/MONITORING AGENCY NAME(S) AND ADDRESS(ES) Rome Laboratory (ERCP) Hanscom AFB MA 01731-5000	
10. SPONSORING/MONITORING AGENCY REPORT NUMBER RL-TR-92-29			
11. SUPPLEMENTARY NOTES Rome Laboratory Project Engineer: Stanford Yukon/ERCP/(617) 893-5353			
12a. DISTRIBUTION/AVAILABILITY STATEMENT Approved for public release; distribution unlimited.		12b. DISTRIBUTION CODE	
13. ABSTRACT (Maximum 200 words) The purpose of the program of research reported here is to develop and demonstrate a realistic numerical model for self-consistent ionospheric propagation and heating of powerful frequency (HF) waves by conjoining existing, separate numerical models for high frequency wave propagation and ionospheric transport. A comprehensive numerical implementation of plasma geometric optics has been enhanced and adapted to the problem of self-consistent ionospheric propagation of high power, high frequency radar signals. The emphasis in this work is on the realistic and rigorous description of the propagation waves so that geometric and spectral characteristics of nonlinear ionospheric effects can be predicted in detail. The plasma geometric optics code has been used in conjunction with an ionospheric transport code to determine self-consistently the HF radiation field and quasilinear modifications of ionospheric plasma properties due to ohmic dissipation of the HF radiation. This allows detailed study of nonlinear phenomena such as beam self-focusing formation of large-scale density cavities and striations, and induced wave ducting. Overviews of the theory underlying the existing models of radiation propagation and ohmic power deposition are given, and enhancements to these models are described. New results achieved using the enhanced models are shown and the treatment of a self-consistent propagation and heating problem is presented. Ionospheric propagation effects on HF radar signals are discussed. (See reverse)			
14. SUBJECT TERMS Ray Tracing, Ionospheric Modification, Over-the-Horizon Radar Propagation, Ionospheric HF Propagation, HF Heating of Ionosphere, Ionospheric Clutter		15. NUMBER OF PAGES 118	16. PRICE CODE
17. SECURITY CLASSIFICATION OF REPORT UNCLASSIFIED	18. SECURITY CLASSIFICATION OF THIS PAGE UNCLASSIFIED	19. SECURITY CLASSIFICATION OF ABSTRACT UNCLASSIFIED	20. LIMITATION OF ABSTRACT UL

Block 13 (Cont'd)

and possible applications of the self-consistent modeling capability to radar technical issues are identified. These issues are especially pertinent to existing and planned high power HF radars.

DTIC QUALITY INSPECTED **B**

Accession For	
NTIS GRA&I	<input checked="" type="checkbox"/>
DTIC TAB	<input type="checkbox"/>
Unannounced	<input type="checkbox"/>
Justification	
By _____	
Distribution/	
Availability Codes	
Dist	Avail and/or Special
X	

CONTENTS

1. SUMMARY	1
2. INTRODUCTION	1
3. OVERVIEW OF THE RADIATION DESCRIPTION	4
4. ADAPTATION OF THE WAVE PROPAGATION COMPUTER CODE TO IONOSPHERIC MEDIA	12
5. MODELING OF OBLIQUE IONOSPHERIC PROPAGATION	19
6. OVERVIEW OF THE IONOSPHERIC TRANSPORT DESCRIPTION	25
7. UPGRADE OF THE IONOSPHERIC TRANSPORT COMPUTER CODE	27
8. COUPLING OF THE WAVE PROPAGATION AND TRANSPORT CODES	39
9. IONOSPHERIC MODIFICATION STUDY	82
10. PROPAGATION EFFECTS ON RADAR SIGNALS	98
11. CONCLUSIONS	100
12. REFERENCES	102
APPENDIX A. COLLISIONAL RATES	104
APPENDIX B. ELECTRON COOLING RATES	106
APPENDIX C. CONFERENCE PRESENTATIONS	109
APPENDIX D. COMPUTER CODES	110

1. SUMMARY

The purpose of the program of research reported here is to develop and demonstrate a realistic numerical model for self-consistent ionospheric propagation and heating of powerful high frequency (HF) waves by conjoining existing, separate numerical models for high frequency wave propagation and ionospheric transport. A comprehensive numerical implementation of plasma geometric optics has been enhanced and adapted to the problem of self-consistent ionospheric propagation of high power, high frequency radar signals. The emphasis in this work is on the realistic and rigorous description of the propagating waves so that geometric and spectral characteristics of nonlinear ionospheric effects can be predicted in detail. The plasma geometric optics code has been used in conjunction with an ionospheric transport code to determine self-consistently the HF radiation field and quasilinear modifications of ionospheric plasma properties due to ohmic dissipation of the HF radiation. This allows detailed study of nonlinear phenomena such as beam self-focusing, formation of large-scale density cavities and striations, and induced wave ducting. Overviews of the theory underlying the existing models of radiation propagation and ohmic power deposition are given, and enhancements to these models are described. New results achieved using the enhanced models are shown, and the treatment of a self-consistent propagation and heating problem is presented. Ionospheric propagation effects on HF radar signals are discussed, and possible applications of the self-consistent modeling capability to radar technical issues are identified. These issues are especially pertinent to existing and planned high-power HF radars.

2. INTRODUCTION

The ionosphere is an inhomogeneous, anisotropic, and dissipative medium which is frequently used as a propagation channel by electromagnetic waves. When the wave power is low, little interaction with the plasma occurs, and the propagation is qualified as linear. When the wave power is high, the wave interacts with the medium and changes its properties, and a nonlinear theory is required to describe the process. This nonlinear action can be either disruptive to an operating system using the ionosphere, or it can be intentionally produced, as is done in ionospheric modification experiments.

In the HF frequency regime, nonlinear phenomena have been identified both theoretically and experimentally. They can be categorized according to their length and time scales into two distinct regimes: large scale electromagnetic phenomena, occurring on scales on the order of kilometers and seconds, and small scale electrostatic phenomena, occurring on scales of the order of centimeters and milliseconds. It is useful to assess the contribution of each phenomenon to the nonlinear HF heating of the ionosphere and to determine which mechanism is more likely to dominate under given HF parameters and ionospheric conditions. For example, parametric instabilities have long been thought to play a major role in plasma heating^[1]. Specifically, two major instabilities, parametric decay and thermal self-focusing, have been frequently invoked to account for experimental results. Although the former belongs to the category of small scale electrostatic phenomena^[2], the latter is observed as large scale structures (1 - 5 kilometers) drifting across the ionosphere with a time scale of the order of one minute^[3]. Different theories of thermal self-focusing provide different estimates of scale length for the

resulting striations, varying from meters to kilometers^[4]. To date, the relative contribution of electrostatic and electromagnetic phenomena in producing the observed striations is still unclear. More recently, strong turbulence theory of caviton collapse and burnout^[5] has been used with new experimental data to put forward a mechanism for early-time HF energy absorption which is finding favor over the more traditional assumption of weak turbulence. Because of the collisional nature of the ionosphere, it is estimated that a large amount of the energy carried by the HF waves is dissipated ohmically^[6], first in the highly collisional D and E regions, and then in the F region. In the F region ohmic heating produces plasma transport primarily along the magnetic field lines. This can create, among other things, large scale, field-aligned thermal density cavities which can also cause self-focusing and can induce wave ducting.

For all the processes mentioned above, a self-consistent analysis which relates the HF waves emanating from the transmitter antenna to the local region in the plasma where the energy is deposited is crucial. Such an analysis permits a true estimation of the pump field amplitude, polarization, and phase needed to initiate the instabilities discussed. A self-consistent analysis also traces the different mechanisms to a common HF beam injected into the ionosphere so that the relative importance of the competing processes can be correctly assessed. Calculation of wave-plasma interaction processes can be made more meaningful in the context of consistent wave and background plasma information. The results provide valuable information for design and performance evaluation of HF radars.

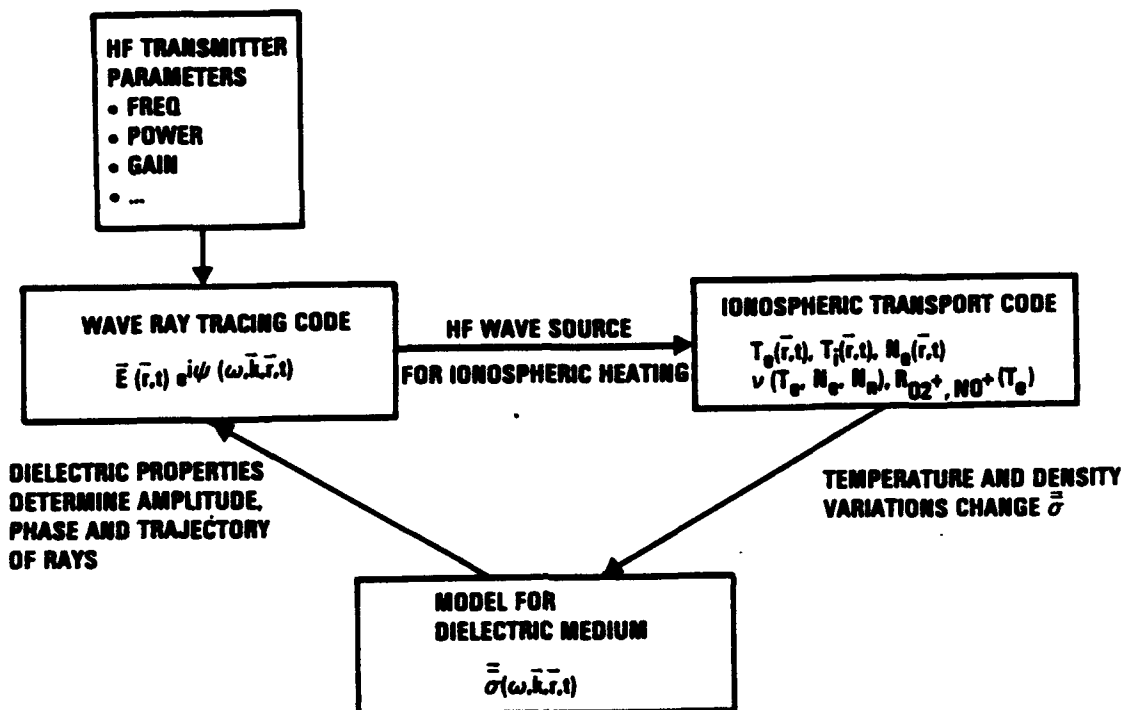
In the current work, these issues have been addressed by enhancing and adapting a numerical implementation of plasma geometric optics, initially developed at Yale University^[7], which uses the geometric optics approximation to calculate wave amplitude, phase, and polarization in inhomogeneous, anisotropic, three-dimensional media. This code is applied to the specific problem of oblique ohmic heating of the ionosphere by powerful HF waves such as those generated by HF radar transmitters. The power dissipation due to the geometric optics wave field is used to determine the heat source in a plasma transport code which predicts ohmic heating of the ionosphere. This heating in turn affects the dielectric tensor of the ionosphere and the propagation of waves is influenced. A block diagram outlining the procedure for self-consistent analysis of ionospheric HF heating is shown in Figure 2-1.

The plasma dielectric tensor is implemented as a separate module invoked by the geometric optics code. This modular aspect permits the use of various types of background plasma models in the radiation calculations. For the current effort an inhomogeneous, magnetized and dissipative cold plasma model is used for the dielectric tensor. The necessary ionospheric parameters are obtained from existing standard models.

In Section 3, a description of the theory underlying the plasma geometric optics code is presented. Section 4 indicates improvements which have been made in the wave propagation model, including the models used for the background ionosphere. Some results of computations for oblique ionospheric propagation in the presence of realistic ionospheric parameters are presented in Section 5. Section 6 gives an overview of the existing ionospheric transport model. In Section 7, upgrades to the ionospheric transport code which extend its applicability into the lower ionosphere are explained. In Section 8 the procedures used to couple the wave propagation and transport codes are set forth. Both linear and self-consistent, nonlinear heating calculations are presented in Section 9.

Section 10 offers a summary of propagation effects on radar signals. Overall conclusions are given in Section 11, along with anticipation of specific applications of this work to radar performance.

Figure 2-1. Block Diagram for the HF Ionospheric Propagation Code



3. OVERVIEW OF THE RADIATION DESCRIPTION

Plasma geometric optics is an asymptotic theory of linear electromagnetic waves in plasmas with weak space and time dependence based upon the well-known WKBJ approximation techniques. Despite the relative simplicity of the computational prescription resulting from this asymptotic theory, complications associated with anisotropy of plasma media and vectorial wave fields require that nontrivial fields be generated by numerical rather than analytical means. A technique known as ray tracing is used for numerical description of high frequency wave propagation in the geometric optics limit.

Although many ray tracing computations have been performed and reported^[8], the code utilized here is the first to determine fully the variation of the amplitude and polarization of the field. The code generates boundary data describing transmitted radiation in a form compatible with the asymptotic theory of propagation, launches geometric optics rays, decomposes them into geometric optics modes, and propagates each of these along separate refracted ray trajectories. The amplitudes and polarizations of the radiation modes are calculated along the way, which is essential for the correct determination of power deposition resulting from coherent superposition of several waves. The code is compatible with an arbitrary model of inhomogeneous, anisotropic background plasma properties as they contribute to the local plasma conductivity tensor, since roots of the local plasma wave dispersion relation are tracked through parameter space by performing computations directly with the components of the conductivity tensor itself. In addition, the code admits general weak space and time variation of the background plasma and fields. This latter property allows the direct prediction of spurious radar doppler shifts caused by time-dependent density fluctuations in the ionosphere. The code detects the occurrence of caustics and implements the asymptotic matching which results from a local boundary layer analysis, permitting graceful continuation of the geometric optics calculation as shown in Figure 3-1.

For ionospheric heating calculations, this capability must be extended beyond the limitations of geometric optics so that accurate field values are obtained everywhere near the caustic surfaces. This may be accomplished in a straightforward manner *a posteriori* by patching the geometric optics amplitude in the neighborhood of the caustic singularity with an amplitude obtained from an appropriate boundary layer analysis. Birefringence and Faraday rotation are treated in a fully automated and general fashion. An appropriate modification of the asymptotic theory is automatically implemented in nearly degenerate environments, where two different modes have nearly the same local dispersion relation. Figure 3-2 illustrates the results of this procedure when an electromagnetic wave enters a magnetized plasma.

This procedure results in a correct accounting for linear mode conversion in weakly anisotropic plasmas. It also allows the prediction of large scale spatial modulation of wave dissipation rates due to long wavelength Faraday rotation in the lower ionosphere.

The asymptotic theory upon which the geometric optics code is based may be summarized as follows. An equation governing linear waves in a magnetized, weakly nonuniform plasma follows directly from Maxwell's equations and an appropriate linear constitutive relation,

$$\nabla \times \nabla \times \underline{\underline{E}} + \frac{1}{c^2} \partial_t^2 \underline{\underline{E}} = -\frac{4\pi}{c^2} \partial_t \int d^3 \underline{r}' \hat{\underline{\underline{g}}}(\underline{r} - \underline{r}', t - t'; \underline{r}', t') \cdot \underline{\underline{E}}(\underline{r}', t'). \quad (1)$$

If the dependence of $\hat{\underline{\sigma}}$ on its last two arguments is weak then nearly plane wave solutions to (1) may be sought of the form

$$\underline{E}(\underline{r}, t) = \underline{E}_0(\underline{r}, t)e^{i\psi(\underline{r}, t)} \quad (2)$$

where the complex amplitude vector \underline{E}_0 is slowly varying in space and time and the real phase function ψ is a nearly linear function of space and time. When the *ansatz* (2) is used in the wave equation (1) there results

$$i\underline{\Delta} \cdot \underline{E}_0 = \underline{L}(\underline{E}_0) \quad (3)$$

accurate through first order in small inverse space and time scales. This approximation neglects effects which are of second order in the ratio of wavelength to the length scale of spatial inhomogeneity and also those which are of second order in the ratio of wave period to the time scale of temporal nonuniformity. Here the operator \underline{L} may be written

$$\begin{aligned} \underline{L}(\underline{E}_0) = & \frac{1}{2}\partial_t(\partial_\omega \underline{\Delta}^T \cdot \underline{E}_0) + \frac{1}{2}\hat{\partial}_t(\partial_\omega \underline{\Delta}^T \cdot \underline{E}_0) \\ & - \frac{1}{2}\nabla \cdot (\partial_{\underline{k}} \underline{\Delta}^T \cdot \underline{E}_0) - \frac{1}{2}\hat{\nabla} \cdot (\partial_{\underline{k}} \underline{\Delta}^T \cdot \underline{E}_0) - \Delta \underline{\Delta} \cdot \underline{E}_0 \end{aligned} \quad (4)$$

where

$$\underline{k} \equiv \nabla\psi, \quad \omega \equiv -\partial_t\psi. \quad (5)$$

The operators with hats are understood to act only on explicit space and time dependences, whereas those without hats act on the implicit dependences through \underline{k} and ω as well. If the plasma is perfectly uniform then the right hand side of (3) vanishes. The tensor $\underline{\Delta}$ has the form

$$\underline{\Delta} = \left(\frac{\omega}{c^2} - \frac{1}{\omega}k^2\right)\underline{\underline{I}} + \frac{1}{\omega}\underline{k}\underline{k} + \frac{4\pi i}{c^2}\underline{\sigma}(\underline{k}, \omega, \underline{r}, t), \quad (6)$$

where $\underline{\sigma}$ is the uniform plasma conductivity tensor evaluated using the local space-dependent and time-dependent plasma properties. For HF waves, ions contribute negligibly to the dielectric properties of the ionosphere and thermal dielectric effects are also unimportant. Thus, the ionosphere is modeled as a cold, magnetized electron plasma with Krook type dissipation governed by collision frequency ν_c , for which the conductivity tensor has the form

$$\underline{\sigma} = \frac{i\omega_p^2}{4\pi\tilde{\omega}(\tilde{\omega}^2 - \Omega_c^2)} \left\{ \tilde{\omega}^2 \underline{\underline{I}} - \underline{\Omega}_c \underline{\Omega}_c - i\tilde{\omega} \underline{\Omega}_c \times \underline{\underline{I}} \right\} \quad (7)$$

where

$$\tilde{\omega} = \omega + i\nu_c, \quad \underline{\Omega}_c = \frac{e}{mc}\underline{B}, \quad \omega_p^2 = \frac{4\pi e^2 n}{m} \quad (8)$$

and \underline{B} is the background magnetic field, e is the magnitude of the electron charge, m is the electron mass, c is the speed of light, and n is the electron density. The tensor $\Delta \underline{\Delta}$ vanishes in the cold plasma limit, and in general is not simply expressible in terms of the tensor $\underline{\Delta}$.

A series solution to (3) is developed based upon the smallness of the right hand side, whence

$$i\underline{\Delta} \cdot \underline{E}_0^{(0)} = 0 \quad (9)$$

and

$$i\underline{\Delta} \cdot \underline{E}_0^{(1)} = \underline{L}(\underline{E}_0^{(0)}). \quad (10)$$

In order for the phase function ψ to be real when the conductivity tensor $\underline{\sigma}$ is not completely antihermitian, an additional small term may be consistently introduced in both zero and first order which contains a free parameter ν , so that the system (9)-(10) becomes

$$i\underline{\Delta} \cdot \underline{E}_0^{(0)} = -i\nu\partial_\omega \underline{\Delta} \cdot \underline{E}_0^{(0)} \quad (11)$$

and

$$i\underline{\Delta} \cdot \underline{E}_0^{(1)} = \underline{L}(\underline{E}_0^{(0)}) + i\nu\partial_\omega \underline{\Delta} \cdot \underline{E}_0^{(0)}. \quad (12)$$

The zero order equation (11) has nontrivial solutions only when

$$\det(\underline{\Delta} + i\nu\partial_\omega \underline{\Delta}) = 0 \quad (13)$$

which defines a local dispersion relation

$$\omega = \Omega(\underline{k}, \underline{r}, t), \quad (14)$$

a dissipation parameter $\nu(\underline{k}, \underline{r}, t)$, and a polarization vector \underline{U} such that

$$(\underline{\Delta} + i\nu\partial_\omega \underline{\Delta}) \cdot \underline{U} = 0 \quad (15)$$

where

$$\underline{E}_0^{(0)} = \alpha \underline{U} \quad (16)$$

and α is a complex scalar amplitude. The polarization vector \underline{U} has an adjoint \underline{V} such that

$$\underline{V}^\dagger \cdot (\underline{\Delta} + \nu\partial_\omega \underline{\Delta}) = 0. \quad (17)$$

When the first order equation (12) is projected onto \underline{V} there results, after some manipulations,

$$\partial_t \alpha + (\partial_{\underline{k}} \Omega) \cdot \nabla \alpha + \frac{1}{2}(\nabla \cdot \partial_{\underline{k}} \Omega)\alpha = \beta \alpha \quad (18)$$

where

$$\begin{aligned} \beta \equiv & \nu + \frac{1}{(\partial_\omega \lambda)} \left\{ -\frac{1}{2}(\partial_{\underline{k}} \Omega) \cdot (\nabla \partial_\omega \lambda) - \frac{1}{2}(\partial_t \partial_\omega \lambda) \right. \\ & + \frac{1}{2}[(\hat{\nabla} \underline{U})^T : (\partial_{\underline{k}} \underline{\Delta}^T) \cdot \underline{V}^* - (\hat{\nabla} \underline{V})^\dagger : (\partial_{\underline{k}} \underline{\Delta}) \cdot \underline{U}] \\ & - \frac{1}{2}[(\hat{\partial}_t \underline{U})^T : (\partial_\omega \underline{\Delta}^T) \cdot \underline{V}^* - (\hat{\partial}_t \underline{V})^\dagger : (\partial_\omega \underline{\Delta}) \cdot \underline{U}] \\ & \left. + \frac{1}{2}[\underline{V}^\dagger \cdot (\hat{\nabla} \cdot \partial_{\underline{k}} \underline{\Delta}) \cdot \underline{U} - \underline{V}^\dagger \cdot (\hat{\partial}_t \partial_\omega \underline{\Delta}) \cdot \underline{U}] \right. \\ & \left. - \underline{V}^\dagger \cdot (\Delta \underline{\Delta}) \cdot \underline{U} \right\} \end{aligned} \quad (19)$$

and λ is that singular value of $\underline{\Delta} + i\nu \partial_\omega \underline{\Delta}$ which vanishes when (13) is satisfied. Application of the method of characteristics to (18) yields the ordinary differential equation

$$\partial_\tau \alpha + \frac{1}{2}(\nabla \cdot \partial_{\underline{k}} \Omega) \alpha = \beta \alpha \quad (20)$$

with characteristic curves defined by

$$\partial_\tau \underline{r} = \partial_{\underline{k}} \Omega. \quad (21)$$

Here τ is a time variable which parameterizes the characteristic curves. Consequently its value is propagated through space by the characteristic curves and it may be considered as a curvilinear space coordinate. Differentiation of (13) leads to

$$\partial_\tau \underline{k} = -\hat{\nabla} \Omega \quad (22)$$

which formally completes the system of ray and amplitude equations. The polarization of the wave is transported along the ray by differentiating (15) with respect to τ and solving for the derivative of \underline{U} . Finally, if coordinates s_1 and s_2 are defined which parameterize the boundary surface from which rays are launched, then it can be shown that

$$\partial_\tau \underline{J} = (\nabla \cdot \partial_{\underline{k}} \Omega) \underline{J} \quad (23)$$

where

$$\underline{J} \equiv \partial_{s_1} \underline{r} \times \partial_{s_2} \underline{r} \cdot \partial_\tau \underline{r}. \quad (24)$$

Equation (23) can be used to simplify (20), which becomes

$$\partial_\tau [((\partial_\omega \lambda) \underline{J})^{1/2} \alpha] = \beta' [((\partial_\omega \lambda) \underline{J})^{1/2} \alpha] \quad (25)$$

where

$$\begin{aligned} \beta' \equiv & \nu + \frac{1}{(\partial_\omega \lambda)} \left\{ \frac{1}{2} [(\hat{\nabla} \underline{U})^T : (\partial_{\underline{k}} \underline{\Delta}^T) \cdot \underline{U}^* - (\hat{\nabla} \underline{U})^\dagger : (\partial_{\underline{k}} \underline{\Delta}) \cdot \underline{U}] \right. \\ & - \frac{1}{2} [(\hat{\partial}_t \underline{U})^T : (\partial_{\omega \underline{\Delta}} \underline{\Delta}^T) \cdot \underline{U}^* - (\hat{\partial}_t \underline{U})^\dagger : (\partial_{\omega \underline{\Delta}} \underline{\Delta}) \cdot \underline{U}] \\ & + \frac{1}{2} [\underline{U}^\dagger \cdot (\hat{\nabla} \cdot \partial_{\underline{k}} \underline{\Delta}) \cdot \underline{U} - \underline{U}^\dagger \cdot (\hat{\partial}_t \partial_\omega \underline{\Delta}) \cdot \underline{U}] \\ & \left. - \underline{U}^\dagger \cdot (\Delta \underline{\Delta}) \cdot \underline{U} \right\}. \end{aligned} \quad (26)$$

The divergence of the group velocity appearing in (23) becomes infinite on a caustic surface. In practice, therefore, (25) is integrated along with the ray equations, the jacobian \underline{J} is calculated from (24), and equations determining the partial derivatives in (24) are also integrated,

$$\partial_\tau \underline{\rho} = \underline{\rho} \cdot (\hat{\nabla} \partial_{\underline{k}} \Omega) + \underline{\eta} \cdot (\partial_{\underline{k}} \partial_{\underline{k}} \Omega) \quad (27)$$

and

$$\partial_\tau \underline{\eta} = -\underline{\rho} \cdot (\hat{\nabla} \hat{\nabla} \Omega) - \underline{\eta} \cdot (\partial_{\underline{k}} \hat{\nabla} \Omega) \quad (28)$$

where ρ is any one of the partial derivative vectors appearing in (24) and η is the corresponding partial derivative of k . The advantage of using (25), (27), and (28) is that all of the coefficients and dependent variables are bounded on a caustic surface.

When the background is isotropic or nearly isotropic the foregoing analysis breaks down and the analysis must be repeated for the case in which two singular values of the wave equation tensor vanish or are both small. One result of switching between the two formalisms is the bifurcation of rays on entry into an anisotropic medium.

The ray tracing code described by the block diagram in Figure 3-3 has been constructed using the formalism described above. Examples of its capabilities are displayed in Figure 3-4.

Figure 3-1. Handling of a Caustic Surface by the Plasma Geometric Optics Code

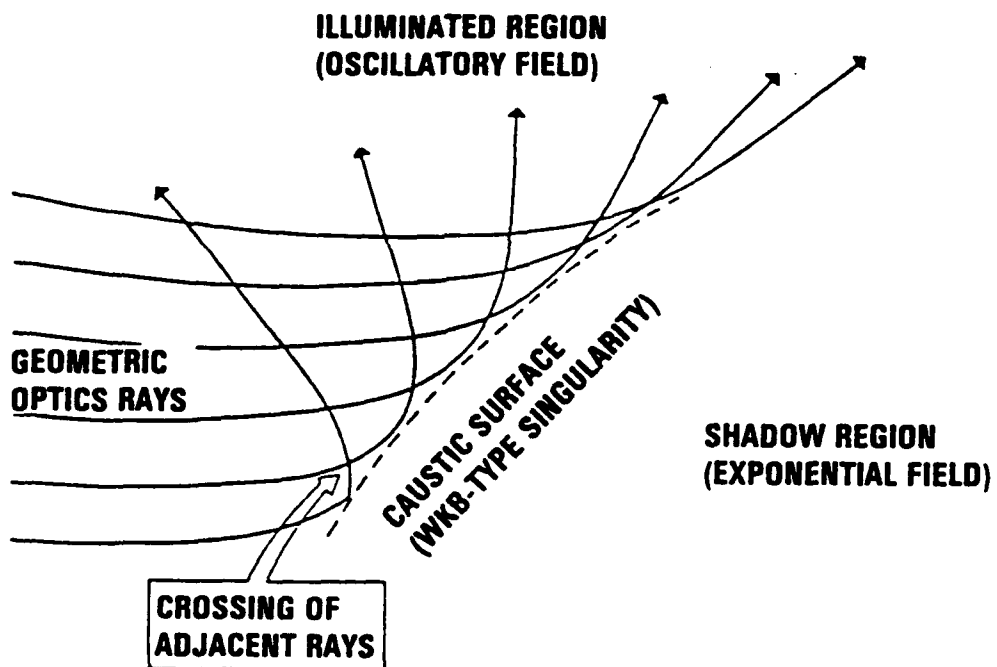


Figure 3-2. Treatment of Birefringence by the Plasma Geometric Optics Code

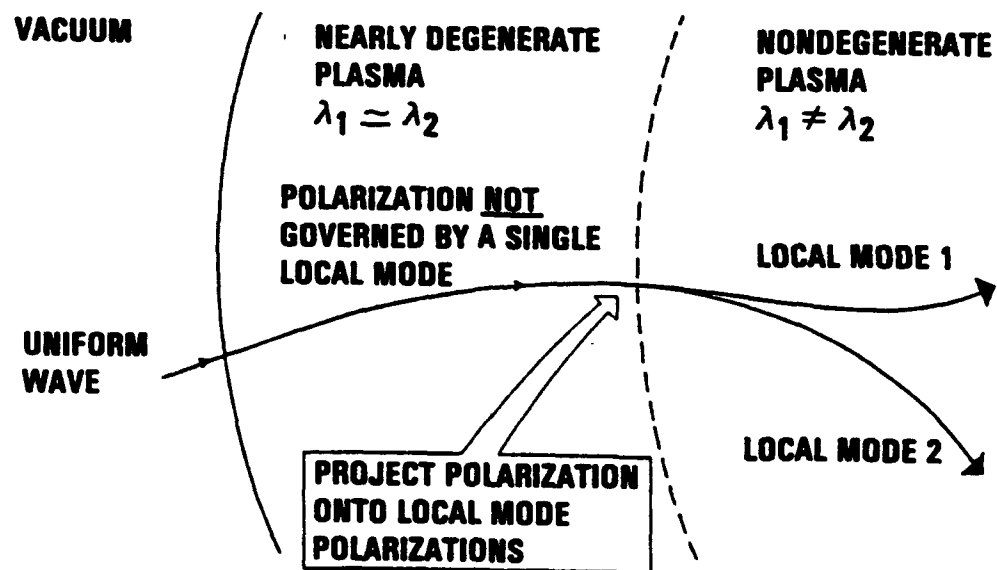


Figure 3-3. Block Diagram for the Plasma Geometric Optics Code and the Transport Code Showing Main Modules, Input and Output Routines, and Coupling Interfaces

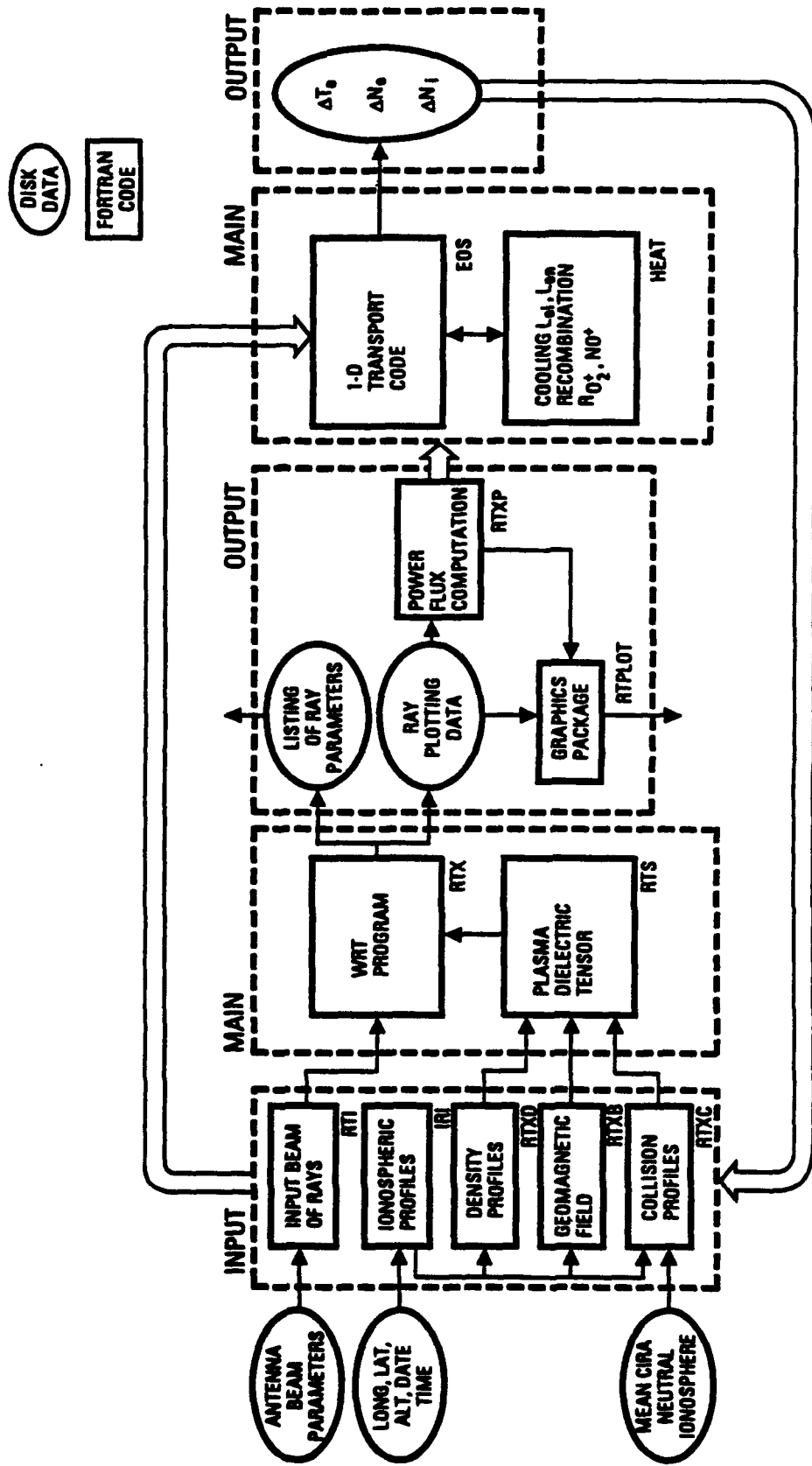
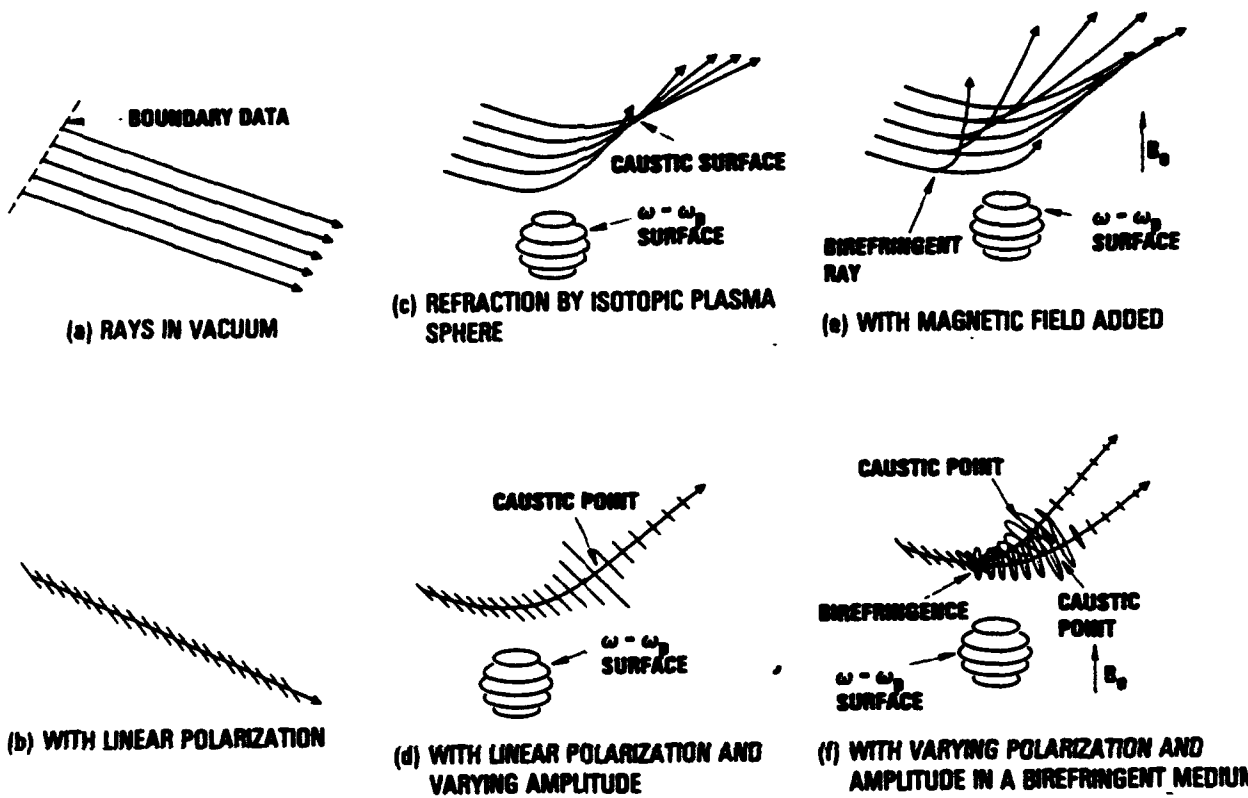


Figure 3-4. Examples of Plasma Geometric Optics Code Capabilities



4. ADAPTATION OF THE WAVE PROPAGATION COMPUTER CODE TO IONOSPHERIC MEDIA

4-1. Antenna Pattern and Radiation Launching

Electromagnetic fields at the boundary surface from which rays are launched must conform to the assumptions of slowly varying amplitude and nearly linear phase which underlie the geometric optics theory. Fields radiated from a transmitting antenna must therefore be expressed in their far field form on the boundary surface. The far field form in conjunction with the local dispersion relation serves to determine the geometric optics phase, amplitude, polarization, and associated properties of the transmitted wave on the exterior of a sphere surrounding the antenna.

An idealized concept of an HF radar antenna has been used to develop a simple, approximate description of a far field antenna radiation pattern. This description has been employed to determine initial data for the ray tracing calculations of HF propagation. The antenna is conceived of as a rectangle on which a uniform, monochromatic surface current has been excited. The uniformity of the surface current may be thought of as the result of a Kirchoff type of approximation. The far field form, derived below, is used to compute amplitude and polarization boundary data for a geometric optics field calculation on the exterior of a sphere surrounding the antenna. The sphere is chosen to be large compared to the antenna but does not extend into the ionosphere. Geometric optics rays are launched from the surface of this sphere and the prescribed amplitude and polarization data are transported into the ionosphere. The arrangement is shown in Figure 4-1.

The magnetic field associated with a surface current \mathbf{K} having harmonic time dependence is

$$\mathbf{B}(\mathbf{r}) = \frac{4\pi}{c} \int_S d^2 \mathbf{r}' \nabla G \times \mathbf{K}(\mathbf{r}') \quad (1)$$

where G is the Green's function

$$G = \frac{e^{ikR}}{4\pi R}, \quad R = |\mathbf{r} - \mathbf{r}'| \quad (2)$$

and $k = \omega/c$. In the far field,

$$\nabla G \simeq ik \frac{e^{ikr}}{r} e^{-ik \cdot \mathbf{r}'} \quad (3)$$

where

$$\underline{k} = k \mathbf{r} / r. \quad (4)$$

In this case the magnetic field due to a uniform current \mathbf{K} becomes

$$\mathbf{B}(\mathbf{r}) = \frac{ie^{ikr}}{cr} \underline{k} \times \mathbf{K} \int_S d^2 \mathbf{r}' e^{-ik \cdot \mathbf{r}'}. \quad (5)$$

This integral may be immediately evaluated over a rectangular antenna surface with dimensions Δx and Δy centered at $\mathbf{r}' = 0$ to give

$$\mathbf{B}(\mathbf{r}) = \Delta x \Delta y \frac{ie^{ikr}}{cr} \underline{k} \times \mathbf{K} \frac{\sin(k_x \Delta x/2)}{k_x \Delta x/2} \frac{\sin(k_y \Delta y/2)}{k_y \Delta y/2} \quad (6)$$

where $k_x = kx/r$ and $k_y = ky/r$. The corresponding electric field is given by

$$\begin{aligned} \mathbf{E} &= -\frac{c}{\omega} \mathbf{k} \times \mathbf{B} \\ &= -\Delta x \Delta y \frac{ie^{ikr}}{\omega r} \mathbf{k} \times \mathbf{k} \times \mathbf{K} \frac{\sin(k_x \Delta x/2)}{k_x \Delta x/2} \frac{\sin(k_y \Delta y/2)}{k_y \Delta x/2}. \end{aligned} \quad (7)$$

These fields have a main lobe and sidelobe patterns in azimuth and elevation. The average power emanating from the antenna is

$$P = c \frac{B_0^2}{8\pi} \Delta x \Delta y \quad (8)$$

where B_0 is the magnetic field at the antenna surface. This field is related to the surface current by

$$\frac{4\pi}{c} \mathbf{K} = \mathbf{n} \times \mathbf{B}_0 \quad (9)$$

whence

$$B_0^2 = \left(\frac{4\pi}{c}\right)^2 K^2. \quad (10)$$

Thus the radiated power is

$$P = \frac{2\pi}{c} \Delta x \Delta y K^2 \quad (11)$$

and the magnitude of the surface current K may be chosen to be consistent with a certain radiated power when the radiated electric field is evaluated on the spherical boundary.

4-2. Evaluation of Wave Power Deposition

The procedure for evaluating the radiation electric field and associated power flux and volumetric power deposition once the ray tracing results are in hand is not trivial. Each geometric optics ray must be considered as a member of a family of rays which describes a single geometric optics mode j having the form

$$\mathbf{E}_j = E_{0j}(\mathbf{r}, t) e^{i\psi_j(\mathbf{r}, t)} \quad (12)$$

where the amplitude vector is nearly constant and the phase function is nearly linear. The transport of the wave phase, amplitude, and polarization along a ray constitutes evaluation of a single geometric optics mode along the ray path. In numerical practice, values of these wave parameters are available at discrete points along the ray path. Thus, for each geometric optics mode there is a three dimensional grid of points at which the wave parameters are available. This grid is generated by tracing rays launched from a two dimensional boundary surface. The field of each mode at an arbitrary point in space and time must be determined by a three dimensional interpolation procedure. The procedure is as follows. Let s_1 and s_2 be coordinates parameterizing the boundary surface, and let τ be a coordinate parameterizing each ray. Then wave parameters for a given mode may be made available on a regular grid in the three dimensional ray space (s_1, s_2, τ) after rays have been traced. Likewise, the position coordinates of these gridpoints are tabulated

as $\underline{r}(s_1, s_2, \tau)$. Suppose that the field of that mode is desired at a point \underline{r}_0 . First it is necessary to determine ray space coordinate values (s_{10}, s_{20}, τ_0) corresponding to the field point \underline{r}_0 such that

$$\underline{r}_0 = \underline{r}(s_{10}, s_{20}, \tau_0). \quad (13)$$

This must be done by inverse interpolation. If interpolation is justifiable, a straightforward three dimensional numerical rootfinding scheme will solve this problem with any reasonable initial guess. In particular, a Newton iteration based on the relation

$$\delta\underline{r} = \delta s_1 \partial_{s_1} \underline{r} + \delta s_2 \partial_{s_2} \underline{r} + \delta \tau \partial_{\tau} \underline{r} \quad (14)$$

where

$$\delta\underline{r} = \underline{r}_0 - \underline{r}(s_1, s_2, \tau) \quad (15)$$

works well. Here the partial derivatives can be evaluated using tabulated ray coordinate data. The increment $\delta\tau$, for example, may be determined by taking the inner product of the total variation $\delta\underline{r}$ above with the vector $\partial_{s_1} \underline{r} \times \partial_{s_2} \underline{r}$. This vector is perpendicular to both $\partial_{s_1} \underline{r}$ and $\partial_{s_2} \underline{r}$, and the result is

$$\delta\tau = (\partial_{s_1} \underline{r} \times \partial_{s_2} \underline{r}) \cdot \delta\underline{r} / (\partial_{s_1} \underline{r} \times \partial_{s_2} \underline{r}) \cdot \partial_{\tau} \underline{r}. \quad (16)$$

Increments δs_1 and δs_2 may be similarly determined. The coordinates s_1 , s_2 , and τ are repeatedly incremented until they reach s_{10} , s_{20} , and τ_0 .

Having determined s_{10} , s_{20} , and τ_0 in this fashion, the wave parameters of the geometric optics mode may be forward interpolated in three dimensions. That is, the phase, amplitude, and polarization at s_{10} , s_{20} , and τ_0 may be found from corresponding values at nearby points in the three dimensional ray space grid determined by the ray tracing. The entire process of inverse interpolation followed by forward interpolation must be repeated for each geometric optics mode which passes across the field point. In a typical oblique propagation scenario there may be four modes passing through a field point: upward launched and downward reflected instances of ordinary and extraordinary magnetized plasma waves. Coherent superposition of these waves is necessary in order to display such features as Faraday rotation of the polarization vector and associated spatial oscillation of the power deposition.

Time-averaged conservation of energy for complex, harmonic fields is expressed as

$$\nabla \cdot \underline{S} = -p \quad (17)$$

where the Poynting vector has the form

$$\underline{S} = \frac{c}{8\pi} \text{Re}[\underline{E}^* \times \underline{B}] \quad (18)$$

and the volumetric power deposition is expressed in terms of the total electric field as

$$p = \frac{1}{2} \text{Re}[\underline{J}^* \cdot \underline{E}]. \quad (19)$$

The total electric field \underline{E} in the geometric optics approximation is a sum over individual geometric optics wave fields

$$\underline{E} = \sum_j \underline{E}_j \quad (20)$$

and the total magnetic field \underline{B} is likewise decomposed,

$$\underline{B} = \sum_j \underline{B}_j. \quad (21)$$

For each geometric optics wave,

$$\underline{B}_j = \frac{c}{\omega} \underline{k}_j \times \underline{E}_j \quad (22)$$

and the total current density \underline{J} is

$$\underline{J} = \sum_j \underline{\sigma}_j \cdot \underline{E}_j. \quad (23)$$

In order to evaluate the power deposition at an arbitrary field point, the conductivity tensor $\underline{\sigma}_j$ must also be interpolated for each radiation mode. When the power deposition is evaluated throughout a volume in the ionosphere, an integral form of the energy conservation equation (17) is routinely computed and checked. The power dissipated in each part of the ionosphere by the HF radiation is compared with the net HF power entering that portion as determined by integrating the Poynting vector over appropriate surfaces.

The power dissipation in (17) is the mechanism of HF ohmic heating in the ionosphere, and is used as a source term in the energy transport analysis discussed in Section 6.

4-3. Model for the Background Ionosphere

As already mentioned, the geometric optics code uses a modular conductivity tensor, that is, the dielectric properties of the medium are incorporated in the code entirely through an isolated module. Of the various ionosphere models currently in usage^[9], we have chosen the International Reference Ionosphere (IRI) model^[10]. It provides electron and ion densities and temperatures as well as neutral temperature as functions of geographic or geomagnetic location and altitude. Parameters are time of day, time of year, and sunspot number. The geomagnetic field is also evaluated by these routines. The IRI is an empirical model that gives the most flexibility and generality for applications of interest. The IRI version used was obtained through the courtesy of D. Bilitza at the National Space Science Data Center at NASA Goddard Space Flight Center. The neutral density model was obtained from the Mean CIRA Reference Atmosphere model^[11] and provides densities of molecular nitrogen and oxygen, atomic oxygen, argon, helium, and hydrogen at various altitudes. The electron collision frequency has contributions from the Coulomb collisions with ions as well as short range collisions with the neutrals. The former is important in the F region, while the latter dominates the D and E regions as well as the lower F region of the ionosphere. The magnetic field is calculated from the 1968 POGO spherical harmonic model^[10]. Together these routines provide a basis for the determination of the electron collision frequency and dielectric properties of the ionosphere. A bicubic spline interpolation scheme is used to smooth out irregularities in the IRI electron and ion density profiles. This procedure ensures continuous first and second derivatives for the electron density and temperature profiles, which are required by the ray tracing code. Figure 4-2 shows densities, temperatures and collision frequency profiles used in our computations and derived from the IRI routines.

Modular design of the software allows easy substitution of models for properties of the ionosphere, and electron density in the ionosphere can also be modeled with an analytical Chapman profile. Chapman profiles are tailored with either a single or double hump to model specific nighttime (F region) or daytime (E and F regions) cases of interest. This simpler model of the ionosphere is computationally much less onerous than the IRI model, and provides a convenient means to quickly predict results of an oblique HF heating experiment. Parameters in the Chapman profile may be determined using knowledge of peak density and its altitude and scale length, usually measured during experiments with a digisonde or a backscatter radar.

4-4. Other Code Improvements

A variety of minor but important improvements were made during the course of work on other tasks. These include elimination of the computation of unimportant dissipation rate derivatives for the ray tracing and correction of an inappropriate form of the vacuum wave equation tensor. Spurious trajectory variation terms were eliminated from the plasma constitutive relation, and the definition of the computed phase function was changed from an absolute to a relative one for numerical reasons. Two coding errors in the conductivity routine and one in the caustic phase jump implementation were corrected, and the procedure for handling change of degeneracy of the background was modified for convenience in subsequently constructing the total wave field. Source code documentation was revised and improved.

In the vicinity of caustic surfaces, where radiation modes reverse their upward propagation and begin to return to earth, the field amplitudes are locally enhanced and the ionospheric plasma density has its largest values along the propagation path. Therefore, the strongest radiation ohmic heating effects occur in these regions and it is particularly important for self-consistent radiation propagation calculations to have an accurate description of the field strengths near caustic surfaces. Unfortunately, the geometric optics approximation breaks down near a caustic surface, and the geometric optics field amplitude actually diverges at the caustic surface. Presently, the geometric optics code computes the field amplitude using a technique which completely avoids numerical difficulties at this singularity and implements a jump condition, derived from a special boundary layer analysis, for the geometric optics field at caustic surfaces. This allows the ray tracing calculation to proceed accurately in the region beyond the occurrence of the caustic singularity but does not give accurate values of the field amplitude near the caustic surface. This defect must be remedied in the future.

Other improvements to be made in the future include the following. The field interpolation procedure described in Section 5 must be improved near the caustic, and a method for predicting the fields in the shadow region near the caustic must be devised. Also, the interpolation algorithm must be improved in order to handle the special situations at transitions between isotropic (degenerate) and anisotropic (nondegenerate) media. In order to accurately predict spurious Doppler shifts due to time-dependent plasma nonuniformities, the location of the surfaces which separate degenerate and nondegenerate regions must be precisely determined. A simple Newton iteration can be applied when crossing such a surface to solve this problem. Reviews of the treatment of reflection of radiation from the earth surface and of the program logic associated with transitions

between degenerate and nondegenerate regions are planned. If calculations of nearly vertical propagation are required, an improvement in the ray tracing algorithm is called for; however, we do not anticipate such requirements immediately since nearly vertical propagation is of little interest in the context of HF radar apart from the modeling of HF ionospheric sounding by peripheral systems in an HF radar installation. A special case, which has never yet occurred in practice but may occur in HF skywave calculations, is the simultaneous occurrence of mode separation due to the onset of plasma anisotropy and caustic reflection. The ray tracing code cannot handle this event and it may become necessary to improve the code accordingly.

Figure 4-1. HF Antenna Model

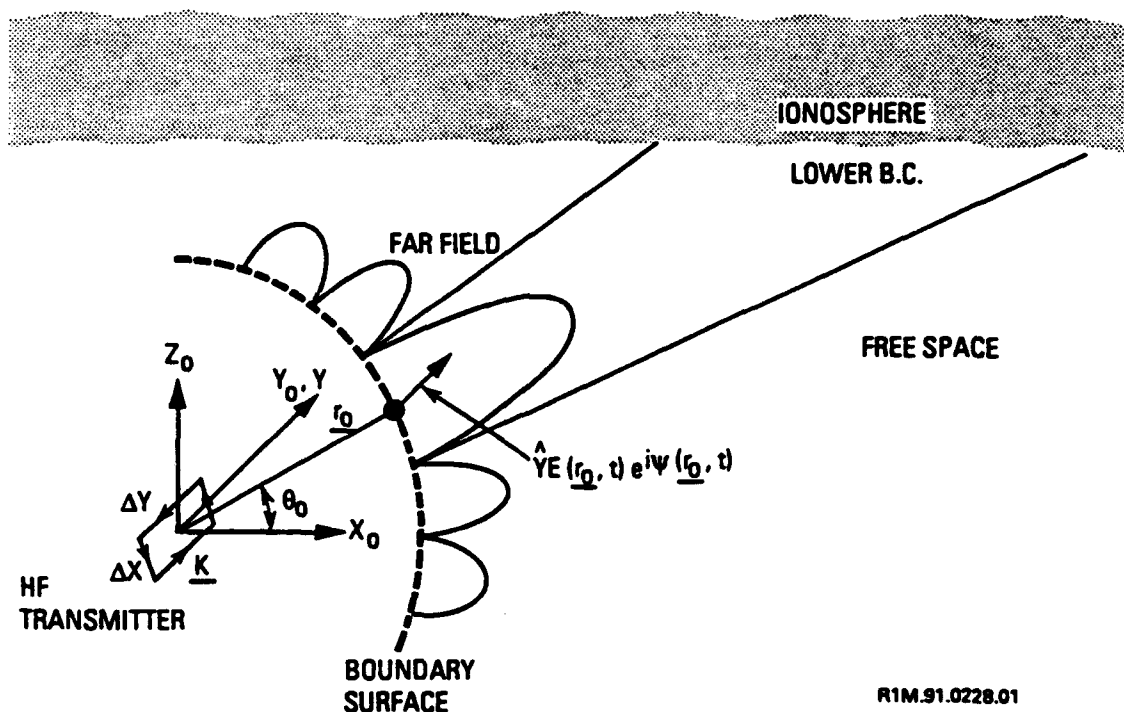
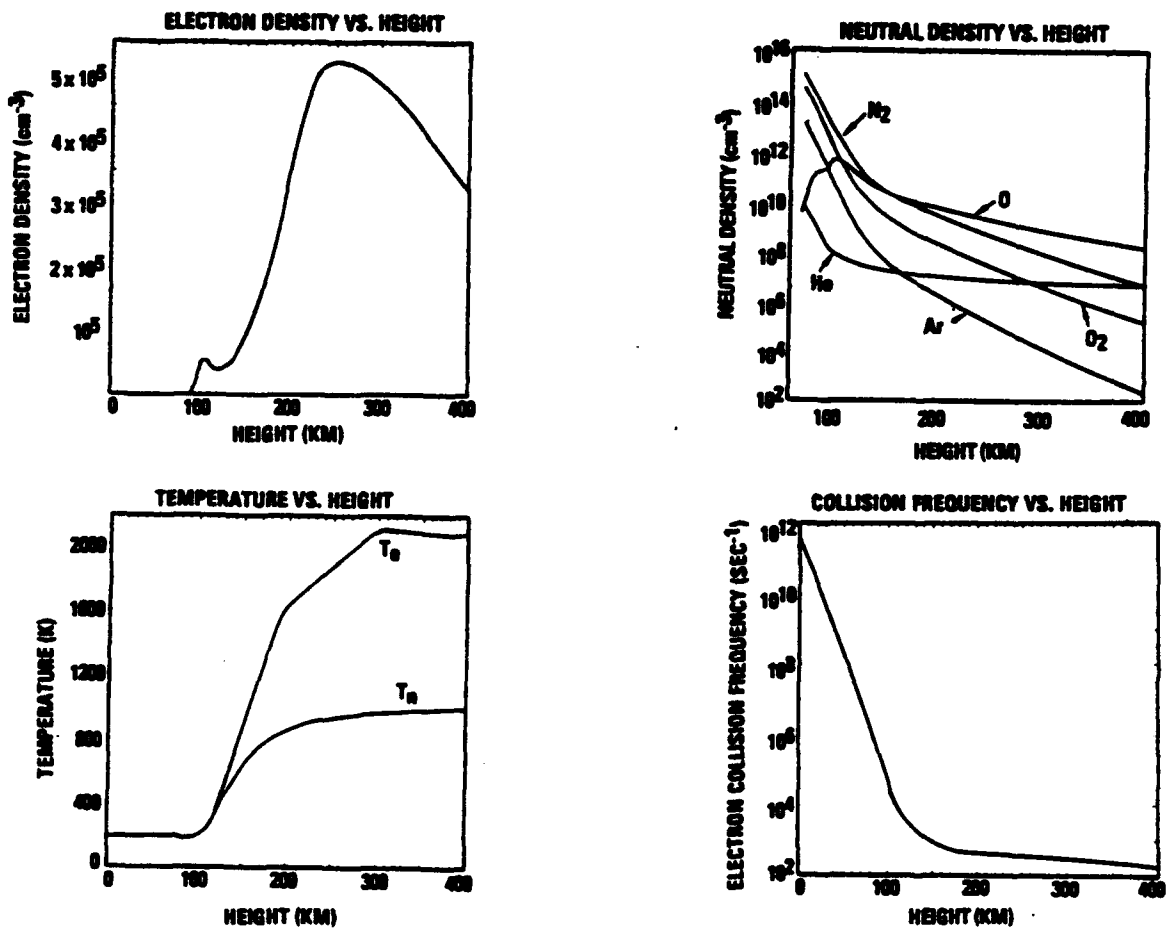


Figure 4-2. Ionospheric Parameters Calculated at 45° North and 70° West for the Month of January at 8:00 AM Local Time and Sunspot No. 100



5. MODELING OF OBLIQUE IONOSPHERIC PROPAGATION

A model has been developed and implemented for the dielectric tensor of the ionosphere at mid-latitude and high-latitude using standard prescriptions for electron density and temperature profiles.

The improved wave propagation code has been exercised to scan frequency, polarization, latitude, and tilt parameters, which affect the propagation of HF beams in the ionosphere.

In this section we show some illustrative calculations simulating an HF radar beam propagating in the ionosphere. All examples use the ionospheric conditions shown in Figure 4-2. Rays are transmitted from a location 45° North and 70° West during the month of January at 8:00 AM local transmitter time. The sunspot number is 100. Figure 5-1 shows an angular scan of ten rays transmitted at 10 MHz with horizontal transmitter polarization. Since the reflection layer altitude is a function of frequency and angle of incidence, some rays reflect from the ionosphere and others pass through it.

All rays bifurcate into distinct ordinary and extraordinary mode rays because of the anisotropy of the magnetized ionospheric plasma. Figure 5-2 shows multiple bounces of a radar-like beam.

Notice that while rays incident at steeper angles are about to complete four hops, grazing incidence rays are barely completing two hops. A full layout of the different projections of a single hop beam of rays is shown in Figure 5-3.

Details of the caustic surface geometry, splitting of the beam into ordinary and extraordinary modes, and shifting of the beam pattern toward the direction of the earth's magnetic field are clearly apparent. Figure 5-4 shows contours of constant ohmic power deposition along the equatorial x-z plane.

Here the contributions from different waves are incoherently superposed since the interference terms are rapidly oscillating in space. Large absorption of the HF energy occurs at low altitude in the D and E regions due to large collision frequencies. Caustic swelling at higher altitudes is also a cause of enhanced absorption of the wave energy. These regions are therefore likely locations for thermal modification of the ionosphere. The code's capability to conserve energy is carried out every time power absorption is calculated, in the manner discussed in Section 4.

A simple way to test how density irregularities affect the radar's HF beam is to include a density blob or bubble at the center of the HF beam. Varying the amplitude and the size of the irregularity gives a parameter regime over which various phenomena are likely to occur. Estimates of the magnitude of effects like beam self-focusing, striations, and beam scattering can be readily obtained in this non self-consistent manner.

For example, in attempting to find out how large a density blob must be before the path of an initial beam of rays is significantly affected, a three dimensional gaussian ball of density was added. Its analytical expression is given in Section 8, equation (15), and the results are shown in Figures 8-9 to 8-11.

Another feature of the linear analysis of oblique propagation is the modeling of ducted waves. With proper launch angle and ionospheric conditions, rays launched from the ground can be trapped or ducted in the ionosphere for very long propagation paths. Figure 5-5 shows a 20 MHz HF beam launched from the east coast of the USA (45°N, 70°W) at an angle of 5.5° above horizontal (other parameters are same as before). The

code runs show that the rays remain ducted for over 6000 km due east of Moscow, Maine and could potentially remain in this mode for longer ranges, i.e., without hitting the ground or escaping from the upper ionosphere. Ducting calculations can be repeated for other operating scenarios and can form the basis of a separate study of such topics as the amount of HF energy ducted, the attenuation suffered by a ducted beam, induced ducting by powerful HF beams, induced duct steering, and the potential for reliable detection of reentry vehicles and other missiles.

Figure 5-1. Angular Scan of Eastward Propagating, Horizontally Polarized Rays at 10 MHz; Rays Reflected from the Ionosphere are Reflected Again from a Curved Earth Surface Assumed to Be a Perfect Conductor

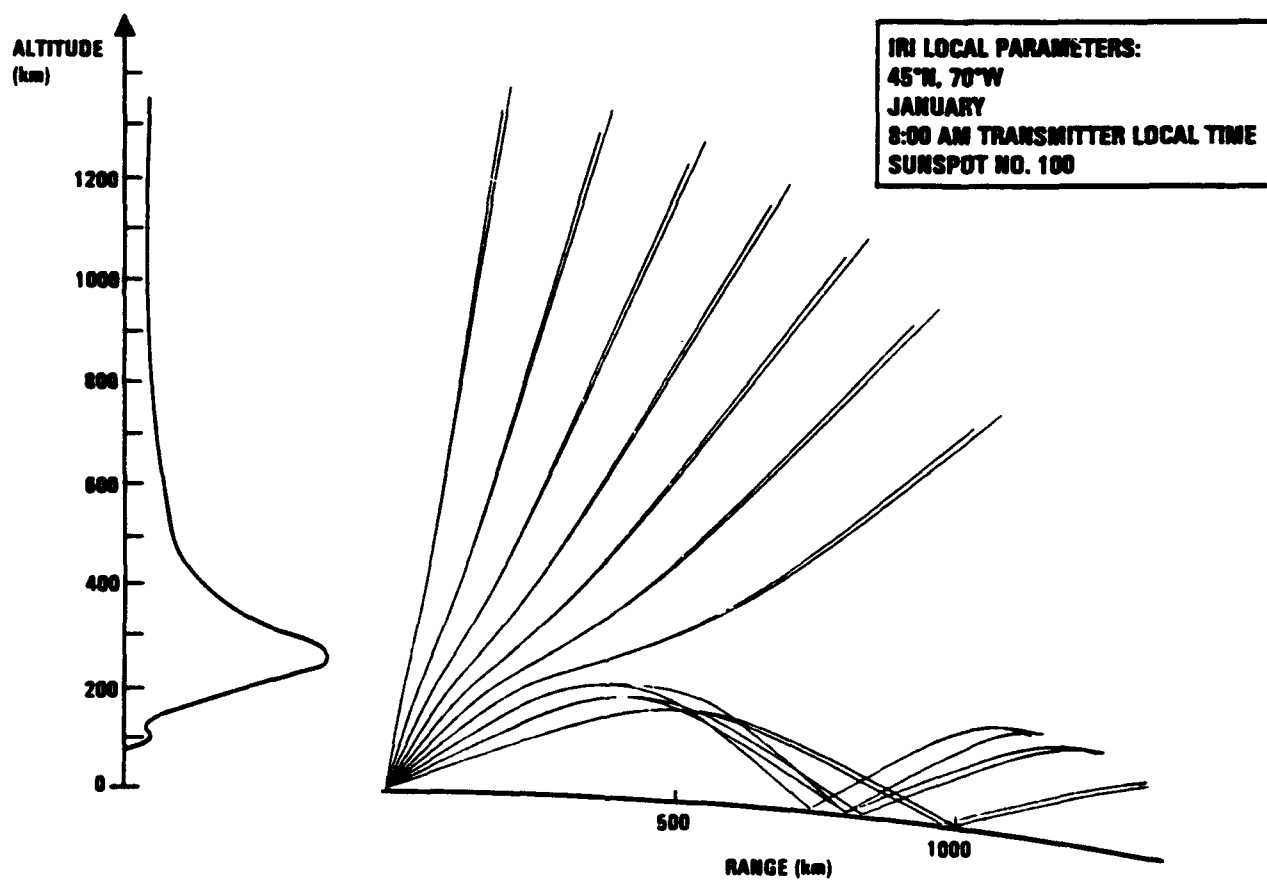


Figure 5-2. Multiple Hops of Radar Rays

IRI LOCAL PARAMETERS:
45°N, 70°W
JANUARY
8:00 AM TRANSMITTER LOCAL TIME
SUNSPOT NO. 100

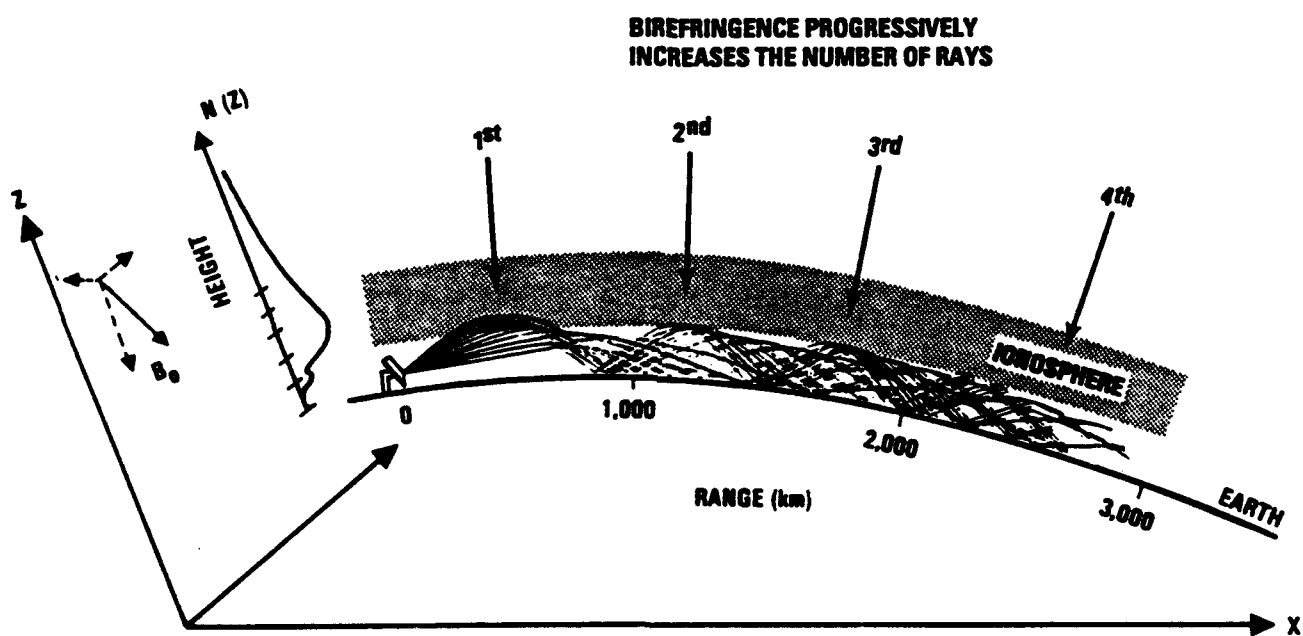


Figure 5-3. Projections of 10 MHz, Horizontally Polarized,
Eastward Propagating Beam of Rays

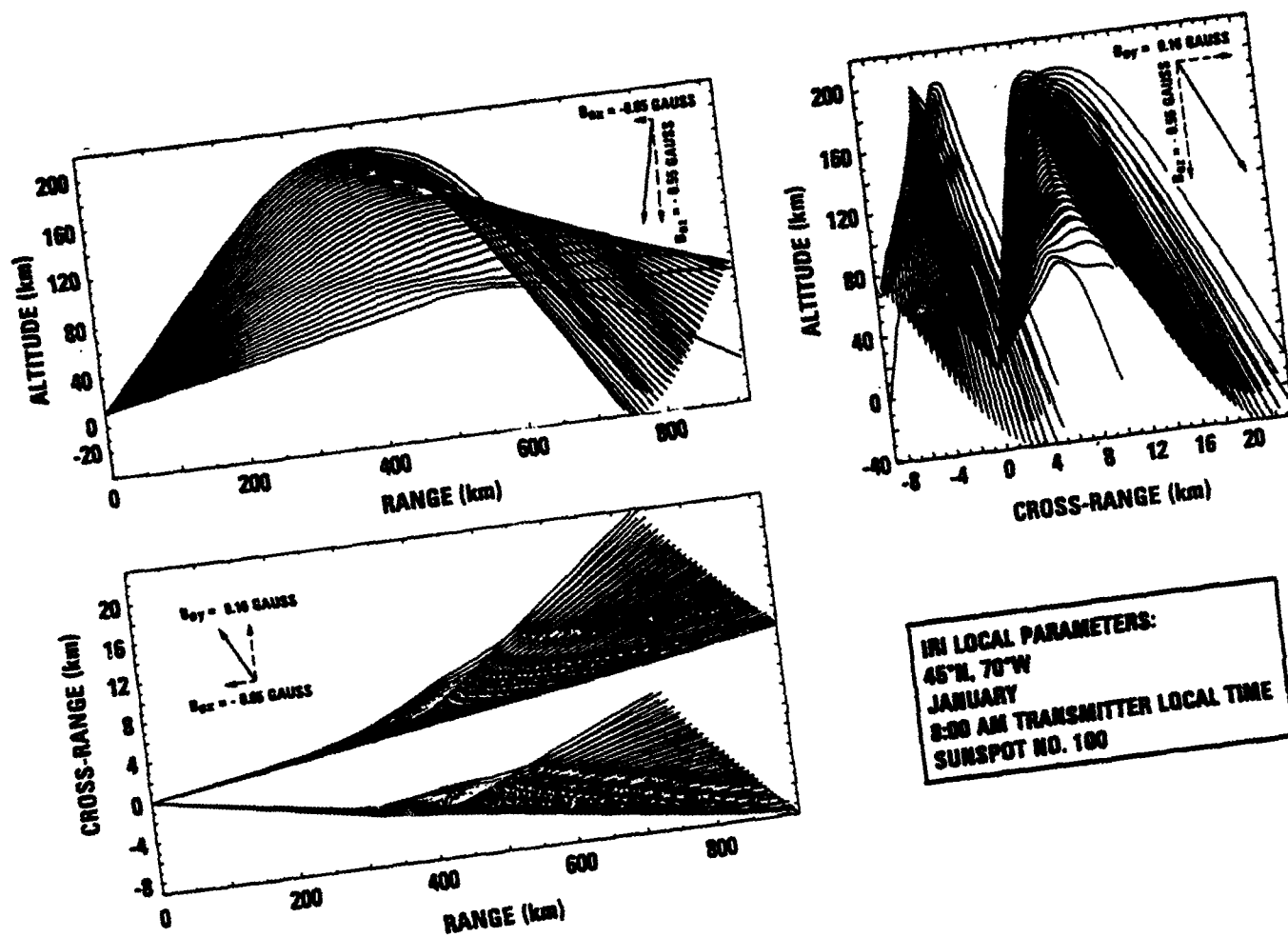


Figure 5-4. Power Deposition

$$P = \langle \bar{J} \cdot \bar{E} \rangle - \frac{1}{2} \bar{J}^* \cdot \bar{E}, \text{ with } \bar{E} = \sum_j \bar{E}_j \text{ and } \bar{J} = \sum_j \bar{\sigma}_j \cdot \bar{E}_j$$

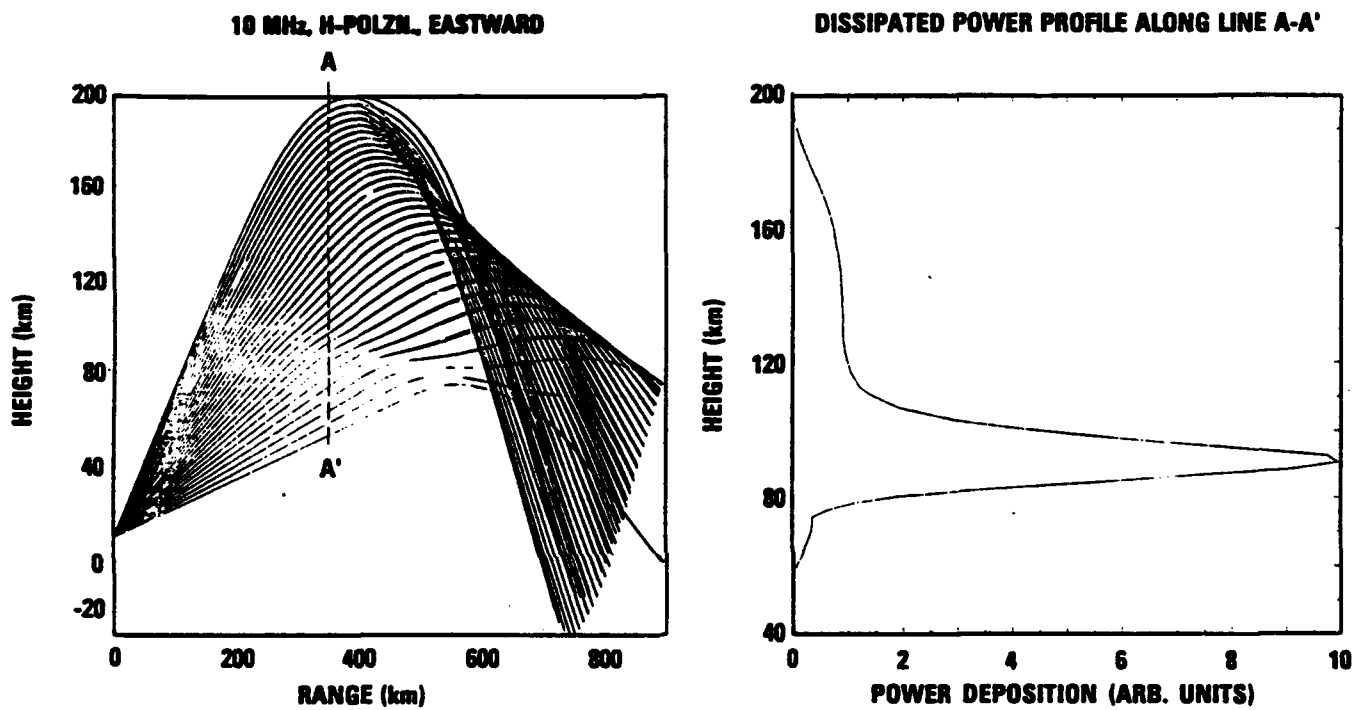
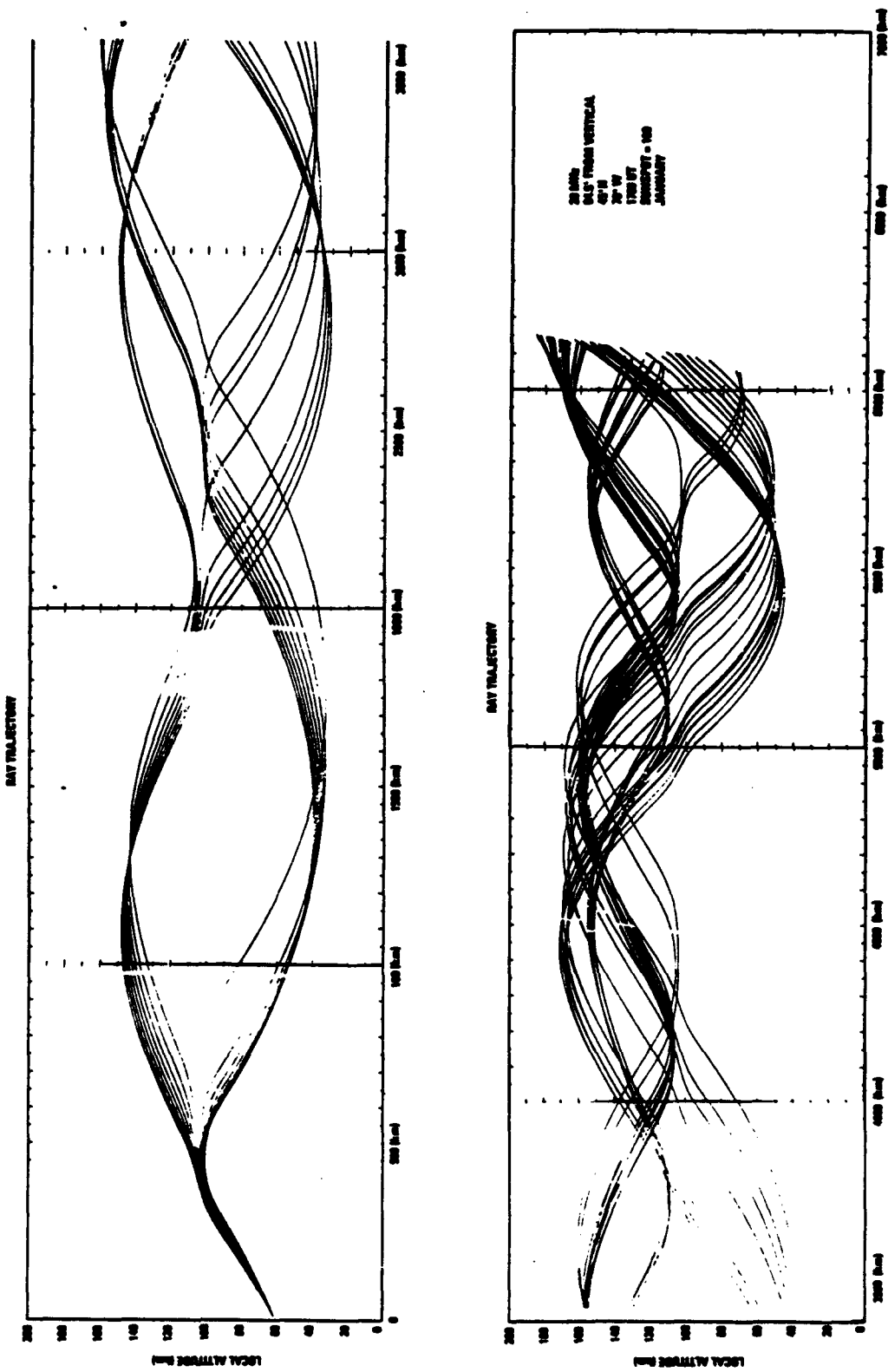


Figure 5-5. Propagation of 20 MHz Ducted Beam Launched Toward Magnetic East from an Antenna Located at 45°N and 70°W, at an Elevation Angle of 5.5° above Horizon. Ducted Beam is Shown Up to a Range of 6000 km and Is Displayed Projected onto a Flat Earth. The Local Altitude Spread of the Beam Ranges between 30 km and 180 km.



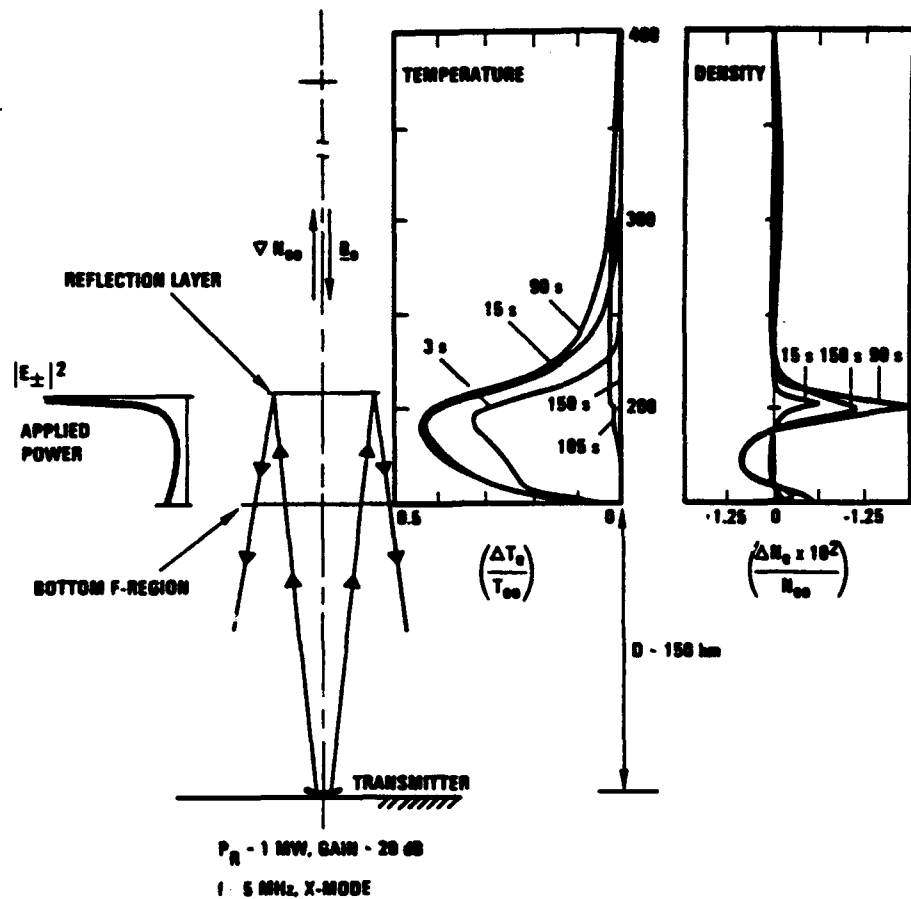
6. OVERVIEW OF THE IONOSPHERIC TRANSPORT DESCRIPTION

In spite of increasing interest in ionospheric modification physics as well as improved analytical and experimental diagnostic tools, there has been a limited number of attempts to understand and simulate bulk processes affecting the background plasma during HF heating. Plasma transport in the ionosphere caused by enhanced absorption of powerful HF waves is one such important effect. Through the years, it has been modeled analytically and numerically for various special cases. For example, mid-latitude transport models have been developed for the heating experiments conducted at Arecibo^[12,13,14] and Platteville^[15,16]. Transport in the polar ionosphere has also been modeled^[6], as has the case of a colinear field-aligned geometry, for which the effects of microwave beam heating from power station satellites^[17] have been simulated numerically. Numerical models of the transport equations have been derived with assumptions which either limit their usage to a specific application or which are simply incomplete.

In the current work, we construct a transport code which can operate equally in different regions and conditions of the ionosphere. The current transport code is designed to predict temperature and density variations of the plasma caused by HF heating in the D, E, and F regions of the ionosphere, i.e., from 65 km altitude to the upper ionosphere. It operates at low, middle, and high latitudes. It includes all the necessary basic atomic, molecular and chemical ingredients that permit a valid analysis of how the background reacts to ohmic absorption of powerful HF waves. The transport code used in this work was developed initially to model high latitude polar plasma heating in the F region^[6]. The original code modeled a single ionic species plasma and assumed an unperturbed equilibrium background. Figure 6-1 shows an example of results from the polar heating code where both electron temperature and density are changed by 90 seconds of vertical heating at 5 MHz.

The polar transport code was later modified to include the effect of recombination on F region heating^[12]. It is this later version of the code that has been upgraded to include the lower ionosphere with its molecular ions, and the ability to operate at arbitrary geomagnetic longitudes and latitudes. Temperature dependent recombination rates is another feature added to the current code. Section 7 discusses the details of the current transport model as well as its numerical implementation.

Figure 6-1. Deformation of the Plasma Temperature and Density Under 90 Seconds of HF Heating Followed by 60 Seconds of Cooling. HF Signal is 5 MHz, ERP =100 MW (from Reference 6).



7. UPGRADE OF THE IONOSPHERIC TRANSPORT COMPUTER CODE

This section presents the transport analysis and code developments which have been performed. Previous limitations on the transport calculation boundaries have been removed so that transport processes in the lower ionosphere, below 150 km, may be modeled. Phenomenology of the E region has been incorporated. The molecular ions NO^+ and O_2^+ , dominant in the E region, have been included in the model along with O^+ , which dominates the F region. The modeled ionospheric plasma is thus composed of three ionic species, NO^+ , O_2^+ , and O^+ , hereafter denoted as species 1, 2, and 3 respectively. Also included in the upgrade are the effects of ionization, recombination, and elastic and inelastic atomic collision processes. Although densities and cross sections are highly uncertain in this collisional region of the ionosphere, there exists sufficient data in the literature to permit qualitative modeling of the major processes occurring in the E region. The transport code has been generalized to account for inclinations of the geomagnetic field lines at arbitrary latitudinal locations.

Finally, software improvements have been made which permit more flexible interaction with the wave propagation code as well as with other routines which model background ionospheric parameters.

7-1. Momentum Equations

The momentum equations for the four species (3 ionic + 1 electronic) are derived from fluid theory, by making the following assumptions:

$$\text{ions are singly ionized } (Z = 1); \quad (1)$$

$$n_1 + n_2 + n_3 = n_e, \quad (\text{quasi - neutrality}); \quad (2)$$

$$n_1 \underline{u}_1 + n_2 \underline{u}_2 + n_3 \underline{u}_3 = n_e \underline{u}_e, \quad (\text{ambipolar diffusion}); \quad (3)$$

where \underline{u}_α is the fluid velocity of species α . When inertia is neglected, the momentum equations take the form

$$\nabla p_\alpha = n_\alpha q_\alpha \underline{E} + \frac{1}{c} n_\alpha q_\alpha \underline{u}_\alpha \times \underline{B} - m_\alpha n_\alpha \underline{u}_\alpha \nu_{\alpha n} - m_\alpha n_\alpha \sum_{\beta \neq \alpha} (\underline{u}_\alpha - \underline{u}_\beta) \nu_{\alpha\beta} - m_\alpha n_\alpha \underline{g}, \quad (4)$$

where $\alpha = 1, 2, 3, 4$ refers to the ionic species 1, 2, 3, and the electrons, respectively. The collisional rate $\nu_{\alpha n}$ represents collisions of species α with the neutral constituents, which are atomic hydrogen (H), atomic helium (He), atomic oxygen (O), molecular nitrogen (N_2), and molecular oxygen (O_2). The collisional rate $\nu_{\alpha\beta}$ represents electron-ion and ion-ion collisions. The quantity q_α is the charge of species α ; m_α is the mass of species α ; c is the speed of light, and the pressure of species α is

$$p_\alpha = n_\alpha T_\alpha. \quad (5)$$

Acceleration due to gravity is denoted by \underline{g} .

When equation (4) is summed over the species index α , then

$$\nabla [p_e + p_1 + p_2 + p_3] = -m_e n_e \nu_{en} \underline{u}_e - m_1 n_1 \nu_{1n} \underline{u}_1 - m_2 n_2 \nu_{2n} \underline{u}_2 - m_3 n_3 \nu_{3n} \underline{u}_3 - \left(\sum_{\alpha=1}^4 m_\alpha n_\alpha \right) \underline{g}. \quad (6)$$

The terms proportional to the electric field \mathbf{E} vanish by invoking quasi-neutrality, and those proportional to $\mathbf{u}_\alpha \times \mathbf{B}$ vanish by invoking ambipolar diffusion. The terms proportional to the electron-ion and ion-ion collisional rates cancel exactly.

Since this model supports ambipolar diffusion, it is necessary to determine the fractional flux for each ionic species given a unit flux of electrons. Such a quantity depends upon the mass, density, and collisional rate of each species. Thus, it is assumed that

$$n_\alpha \mathbf{u}_\alpha = \delta_\alpha \frac{M_I \nu_{IN}}{m_\alpha \nu_{an}} n_e \mathbf{u}_e , \quad (7)$$

where $\alpha = 1, 2, 3$ (ionic species index),

$$\delta_\alpha \equiv \frac{n_\alpha}{n_e} , \quad (8)$$

and $M_I \nu_{IN}$ is a mass-weighted ionic collisional term, which is determined by summing (7) over α and using (3),

$$M_I \nu_{IN} = \frac{(m_1 \nu_{1n})(m_2 \nu_{2n})(m_3 \nu_{3n})}{\delta_1(m_2 \nu_{2n})(m_3 \nu_{3n}) + \delta_2(m_1 \nu_{1n})(m_3 \nu_{3n}) + \delta_3(m_1 \nu_{1n})(m_2 \nu_{2n})} . \quad (9)$$

Substitution of (7) into (6) yields

$$n_e \mathbf{u}_e = \frac{-1}{m_e \nu_{en} + M_I \nu_{IN}} \{ \nabla [p_e + p_1 + p_2 + p_3] + (\sum_\alpha m_\alpha n_\alpha) \mathbf{g} \} . \quad (10)$$

When the projection of the electron flux onto a magnetic field line is taken, it is found that

$$n_e w_e = -D \left[\frac{\partial}{\partial s} [n_e (T_e + T_i)] + \sum_\alpha m_\alpha n_\alpha \mathbf{g} \cdot \mathbf{B} / B \right] , \quad (11)$$

where $w_\alpha \equiv \mathbf{u}_\alpha \cdot \mathbf{B} / B$, $s \equiv \mathbf{r} \cdot \mathbf{B} / B$, $\mathbf{B} \equiv B_x \mathbf{e}_x + B_y \mathbf{e}_y + B_z \mathbf{e}_z$, $B \equiv [B_x^2 + B_y^2 + B_z^2]^{1/2}$ is the earth's magnetic field, and the diffusion coefficient D is

$$D \equiv \frac{1}{m_e \nu_{en} + M_I \nu_{IN}} , \quad (12)$$

and where it has been assumed that the ionic species are at the same temperature, namely,

$$T_i \equiv T_1 = T_2 = T_3 . \quad (13)$$

The ion (T_i) and neutral (T_n) temperatures are treated as constant in time, but are allowed to vary in space, a feature which was not included in past versions of the transport code^[6,12]. Equations (10), (11), and (12) assume the ambipolar plasma form with a single ion species having an effective mass of M_I and an effective ion-neutral collision frequency of ν_{IN} . A summary of the collisional rates included in this model is given in Appendix A.

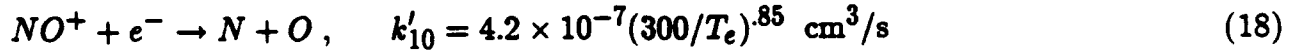
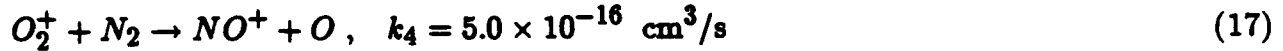
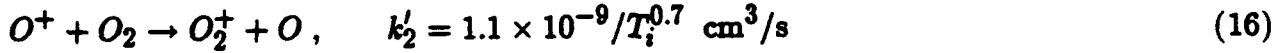
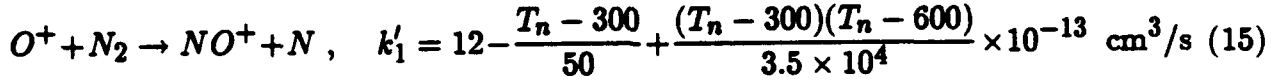
7-2. Continuity Equations

The continuity equation along a magnetic field line for each species is of the form

$$\frac{\partial n_\alpha}{\partial t} + \frac{\partial}{\partial s} n_\alpha w_\alpha = \beta_\alpha(s, t) + P_\alpha(s, t) + S_{\alpha\alpha}(s) , \quad (14)$$

where $S_{o\alpha}$ is the steady state source term which brings about the equilibrium density profile, P_α is the production rate, and β_α is the recombination rate for species α .

According to Schunk and Walker^[18], the important chemical reactions from 100 – 600 km in altitude which involve O^+ , O_2^+ , and NO^+ are



The dissociative reaction rates k'_{10} and k'_{11} are those cited by Schunk and Nagy^[19]. The reaction rates k'_1 and k'_2 are those cited by Park and Banks^[20]. All other reaction rates are from Schunk and Walker^[18].

The continuity equations then take the form

$$\frac{\partial}{\partial t} n_1 + \frac{\partial}{\partial s}(n_1 w_1) = S_{o1} + n(N_2)[k'_1 n_3 + k_4 n_2] - k'_{10} n_e n_1 \quad (20)$$

$$\frac{\partial}{\partial t} n_2 + \frac{\partial}{\partial s}(n_2 w_2) = S_{o2} + k'_2 n(O_2) n_3 - [k'_{11} n_e + k_4 n(N_2)] n_2 \quad (21)$$

$$\frac{\partial}{\partial t} n_3 + \frac{\partial}{\partial s}(n_3 w_3) = S_{o3} - [k'_1 n(N_2) + k'_2 n(O_2)] n_3 \quad (22)$$

$$\frac{\partial}{\partial t} n_e + \frac{\partial}{\partial s}(n_e w_e) = S_{oe} - [k'_{10} n_1 + k'_{11} n_2] n_e. \quad (23)$$

The molecular ions, n_1 and n_2 are assumed to be in chemical equilibrium, in accord with the findings of Schunk and Walker^[18]. Hence, the lefthand sides of equations (20) and (21) are set to zero, and these equations then reduce to

$$n_1 = \frac{S_{o1} + [k'_1 n_3 + k_4 n_2] n(N_2)}{k'_{10} n_e} \quad (24)$$

$$n_2 = \frac{S_{o2} + k'_2 n(O_2) n_3}{k'_{11} n_e + k_4 n(N_2)}. \quad (25)$$

The quasi-neutrality equation (2) implies that the sum of (24) and (25) yields

$$n_3 = n_e - n_1 - n_2 = \frac{k'_{10} n_e^2 - S_{o1} - \frac{k'_{10} n_e + k_4 n(N_2)}{k'_{11} n_e + k_4 n(N_2)} S_{o2}}{k'_{10} n_e + k'_1 n(N_2) + k'_2 n(O_2) \frac{k'_{10} n_e + k_4 n(N_2)}{k'_{11} n_e + k_4 n(N_2)}}. \quad (26)$$

Originally, Shoucri et al.^[6] did not include recombination in the continuity equation, as it was their desire to model short time ($t < 90$ s) effects in the F region. They found

that the density changes caused by the pressure imbalance induced by HF heating never saturated over these short time periods. Later, Hansen^[12] added a recombination rate to the continuity equation of the form

$$\beta(T_i, T_n) = k'_2 n(O_2) + k'_1 n(N_2) \text{ s}^{-1} . \quad (27)$$

This recombination rate models dissociative recombination of NO^+ and O_2^+ by a loss of O^+ , an effect which is currently present in the continuity equation (22) for O^+ as well as in the equations (20) and (21) for NO^+ and O_2^+ as production rates.

The reaction rates for NO^+ and O_2^+ are functions of the electron temperature T_e , and as indicated in equation (23), there is a loss of electrons at a rate which depends upon the electron temperature in a nonlinear fashion, namely, $\beta_e(T_e)$. Physically, what occurs is that the ionosphere is heated, and the electron temperature increases; the electrons then do not recombine as easily as they did before heating. This is modeled in (18) and (19) by the reaction rates being inversely proportional to the electron temperature raised to a power which has been determined empirically^[19].

7-3. Electron Energy Equation

The electron energy equation along a magnetic field line^[6] is of the form

$$\frac{3}{2} k \{ n_e \frac{\partial T_e}{\partial t} + n_e w_e \frac{\partial T_e}{\partial s} \} + k n_e T_e \frac{\partial w_e}{\partial s} = \frac{\partial}{\partial s} [K_e \frac{\partial T_e}{\partial s}] + Q_{hf} + Q_o - L_e , \quad (28)$$

where k is Boltzmann's constant, and where the first term represents the time rate of change of the electron temperature T_e due to heating; the second term represents convection, and the third pressure flux. The first term on the righthand side of (28) represents thermal conductivity along a magnetic field line, where K_e is the parallel coefficient of thermal conductivity^[6],

$$K_e = \frac{7.75 \times 10^5 T_e^{5/2}}{1 + 3.22 \times 10^4 (T_e^2/n_e) \sum_k n_k < Q_k >} \text{ eV cm}^{-1} \text{ s}^{-1} \text{ K}^{-1} , \quad (29)$$

and where the summation in the denominator is over all the products of neutral gas species concentrations n_k with average electron-neutral momentum transfer cross sections $< Q_k >$.

The second term on the righthand side of (28), Q_{hf} , is the HF heating source, $Q_{hf} = \text{Re}[\mathbf{E}_{hf}^* \cdot \mathbf{J}] = \text{Re}[\mathbf{E}_{hf}^* \cdot \underline{\underline{\sigma}} \cdot \mathbf{E}_{hf}]$, where \mathbf{E}_{hf} is the complex amplitude of the HF electric field whose full space-time dependence is given by $[\mathbf{E}_{hf}(r)e^{-i\omega_{hf}t} + \text{c.c.}]/2$. The third term on the righthand side of (28), Q_o , accounts for the steady state source which brings about the equilibrium temperature profile in the absence of the HF pump. The last term on the righthand side of (28), L_e , represents the rate of electron cooling caused by translational, rotational, and vibrational excitation of neutrals as well as cooling by collisions with ions. A summary of the terms included in L_e can be found in Appendix B.

7-4. Recovery of Limiting Cases

In the limit of $n_1 = n_2 = 0$ the transport equations used by Hansen^[12] are recovered,

$$\frac{\partial}{\partial t} n_3 + \frac{\partial}{\partial s} (n_3 w_3) = S_{o3} - [k'_1 n(N_2) + k'_2 n(O_2)] n_3 \quad (30)$$

and

$$n_e w_e = -D \left[\frac{\partial}{\partial s} [n_e (T_e + T_i)] + \sum_{\alpha} m_{\alpha} n_{\alpha} g \cdot B / B \right] , \quad (31)$$

where $n_3 = n_e$ (quasi-neutrality), and $D = \frac{1}{m_e \nu_{en} + m_3 \nu_{3n}}$. The electron energy equation used by Hansen^[12] is the same as (28), except that some updates have been made to the L_e term for the current model.

If the gravitational term and the recombination term, which are terms linear in the electron density or its first derivative, are incorporated into the equilibrium source term in (30), an assumption valid when heating on short time scales, then the transport model of Shoucri et al.^[6] is recovered,

$$\frac{\partial}{\partial t} n_e + \frac{\partial}{\partial s} (n_e w_e) = S_{oe} \quad (32)$$

$$n_e w_e = -D \left[\frac{\partial}{\partial s} [n_e (T_e + T_i)] \right] . \quad (33)$$

The electron energy equation used by Shoucri et al.^[6] is identical to that of Hansen^[12].

The current transport model has the ability to recover these limits. It can be run with the recombination rate updated in time (because T_e is changing), it can be run with the recombination rate constant in time (in analogy to Hansen^[12]), or it can be run without the effect of recombination (Shoucri et al.^[6])

7-5. Numerical Solution for Transport

Using a predictor-corrector form of the time-averaged Crank-Nicholson^[21] tri-diagonal method, equations (11), (12), (23), (24), (25), (26) and (28) are solved when the HF energy is turned on. The temporal and spatial modifications of density and temperature are solved in the following manner:

1. Solve for T_e using (28) with Q_{hf} turned on.
2. Update all coefficients: L_e , K_e , ν_{en} , ν_{ei} , β_e .
3. Solve for the electron density, n_e , using (23).
4. Update all coefficients: L_e , K_e , ν_{en} , ν_{ei} , β_e .
5. Update the O^+ density (n_3), the O_2^+ density (n_2), and the NO^+ density, using (24), (25), and (26).
6. Update all coefficients: L_e , K_e , ν_{en} , ν_{ei} , β_e .
7. Repeat at each time step.

The boundary conditions utilized are those established by Hansen^[12]. Any linear combination of T_e and $\partial T_e / \partial s$, or n_e and $\partial n_e / \partial s$, may be used as boundary conditions at the lower and upper endpoints for equations (23) and (28). For the current runs, at the lower boundary,

$$T_e(z = z_{lower}, t) = T_e(z = z_{lower}, t = 0) \quad (34)$$

$$n_e(z = z_{lower}, t) = n_e(z = z_{lower}, t = 0) ; \quad (35)$$

whereas, at the upper boundary,

$$\partial T_e / \partial s(z = z_{upper}, t) = \partial T_e / \partial s(z = z_{upper}, t = 0) \quad (36)$$

$$\partial n_e / \partial s(z = z_{upper}, t) = \partial n_e / \partial s(z = z_{upper}, t = 0) . \quad (37)$$

In the D-E layer, it has been determined that the temperature and density modifications are essentially local in nature because the thermal conductivity, compression, convection, and diffusion coefficients nearly vanish. Thus, in this region of space, the conductivity, compression, and convection terms are set equal to zero in (refte eqn), and the local balance between heating and cooling determines the temperature modification, which is isotropic in nature, because $\omega_{ce} \sim \nu_e$. In the F layer, however, where these terms are not negligible, the complete equation (28) is solved, and the temperature modifications are field-aligned because $\omega_{ce} \gg \nu_e$.

7-6. Establishment of the Equilibrium

Before any heating can be done, it is necessary to first set up the equilibrium profiles. For T_e , T_i , T_n , n_e , and the ionic densities, this is carried out by invoking IRI (International Reference Ionosphere) at the launch point to obtain a data set, and by then making a cubic spline fit to the data as a function of altitude only. This guarantees continuous first and second derivatives, necessary for both the ray tracing and transport codes. While variations of temperature and density with respect to latitude and longitude have not been implemented, the capacity for including such variations has been developed.

The neutral densities are set up using CIRA data, and there is not a spline fit incorporated into this package for these profiles. Since there is scarce CIRA data for atomic hydrogen density, it was modeled using a Boltzmann law for the pressure as a function of altitude.

Two typical cases have been run using the transport code. The first is due east HF propagation from Moscow, Maine, with sunspot number 150 (a value typical for 1991 and 1992), in January at 1200 hours local time, denoted as case 0112. Depicted in Figures 7-1, 7-2, and 7-3 are the neutral density profiles; the equilibrium profiles of T_e , T_i , and T_n ; and the equilibrium profiles of n_e , n_1 , n_2 , and n_3 for case 0112.

The second case is due east propagation from Moscow, Maine, with sunspot number 150 in July at 0400 hours local time, denoted as case 0704. Figures 7-4 and 7-5 exhibit the equilibrium temperature and density profiles for this case. (The neutral density profiles are the same as in case 0112.)

The original transport code^[6] was developed for the polar region and hence $\nabla n \parallel B \parallel e_z$ for such geometry. Later, Hansen^[12] extrapolated the code to describe mid-latitude effects such as those observed at Arecibo Observatory, and thus the magnetic field was chosen to have a dip angle with a typical value of 50°. In the current version of the code, the transport calculation is run on a magnetic field line whose orientation is specified as an input. Given the beginning point of a field line and the grid spacing, the field line along which modifications are to be calculated is established. Associated with each grid point on the field line are two reference frames: the launch point reference frame (l.p.), where $(x, y, z) = (0, 0, 0)$ is at the launch point; and the center-of-earth reference frame (c.o.e.), which provides the latitude, longitude, and altitude of each grid point.

Once an altitude is associated with each grid point on a field line, the equilibrium densities and temperatures of that grid point can be specified. Latitudinal and longitudinal variations in the density and temperature profiles can be included by calling IRI data for each grid point.

It is necessary that the first and second derivatives of density and temperature be continuous for the transport calculations, because the modifications of temperature and density depend upon their derivatives, which are incorporated into the diffusion term, the thermal conductivity term, the convective term, and the pressure flux term. The cubic spline fit to the IRI data addresses this requirement.

When the equilibrium profiles are established, the sources which sustain the profiles are determined. Equations (23) through (26) are solved in steady state to ascertain the density sources, $S_{o\alpha}$. The temperature source Q_o is found from (28) with $\partial/\partial t = 0$ and $Q_{hf} = 0$.

7-7. Versions of the Transport Code

Three different versions of the transport code currently exist. The first is "eos_oth", which runs the transport on many field lines in many different magnetic meridian planes. The second is "eos_oth_1plane", which runs the transport on many field lines in just one magnetic meridian plane. To append all of the output files together from running "eos_oth_1plane" on many different planes, there exists a short program "output". Finally, there is a version of the code called "eos_diag", which allows the operator to choose a specific field line in a specific magnetic meridian plane upon which he/she desires to see diagnostic output of all equilibrium quantities, as well as the quantities which vary in time because of heating. The program "eosplot_oth" plots the diagnostic output from "eos_diag".

Figure 7-1. Neutral Density Profiles

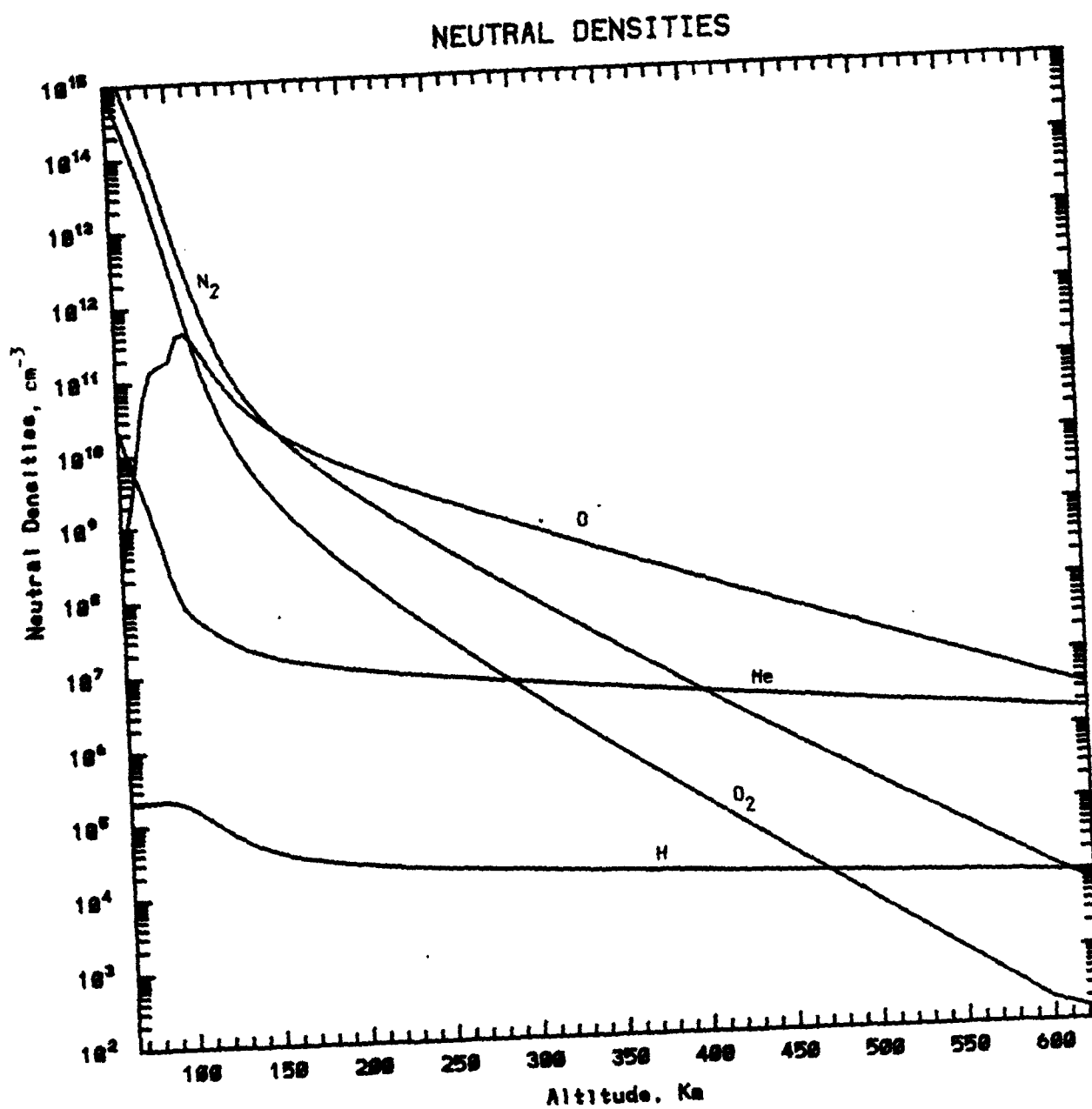


Figure 7-2. Equilibrium Temperature Profiles for Case 0112

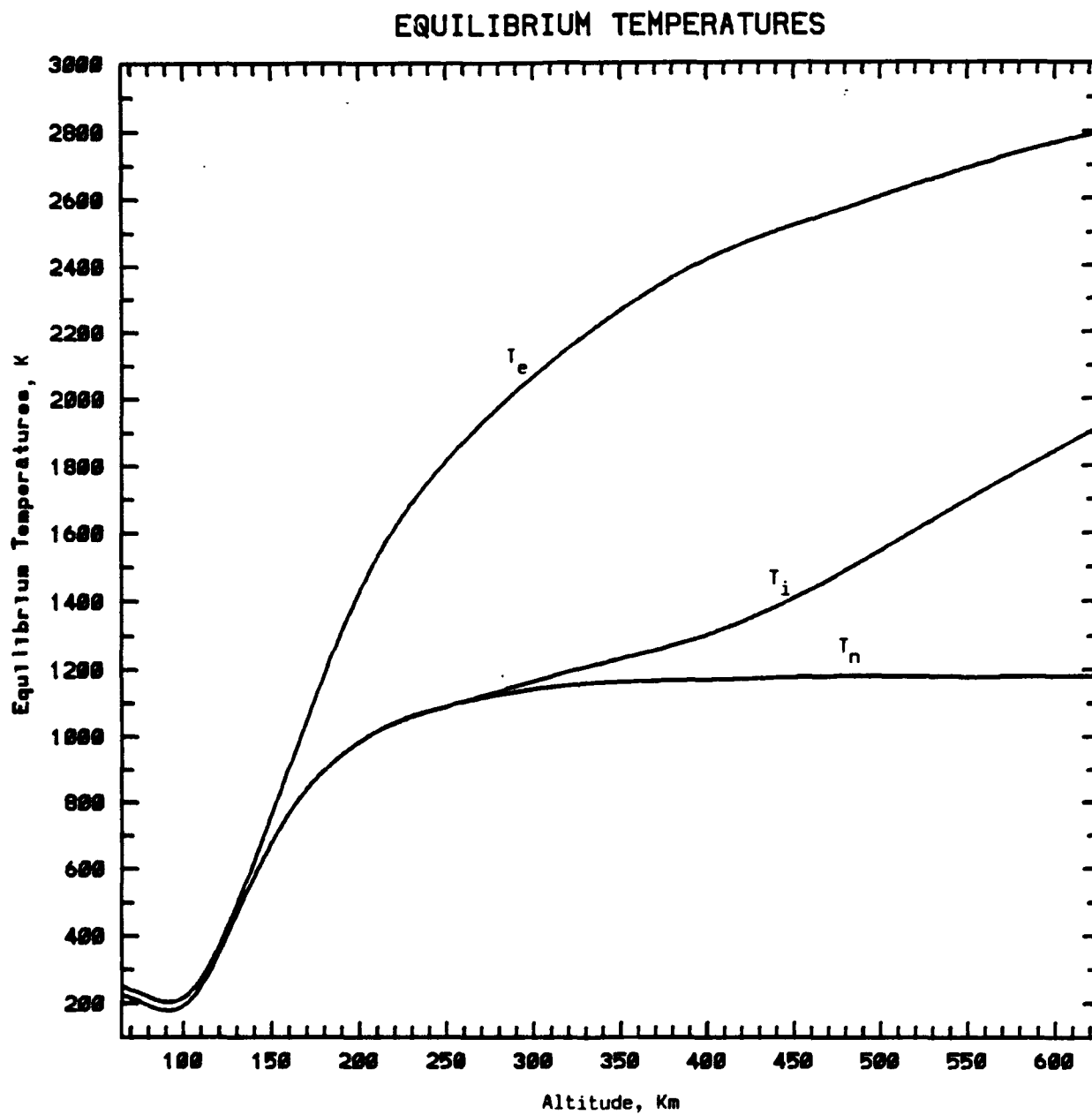


Figure 7-3. Equilibrium Charged Particle Density Profiles for Case 0112

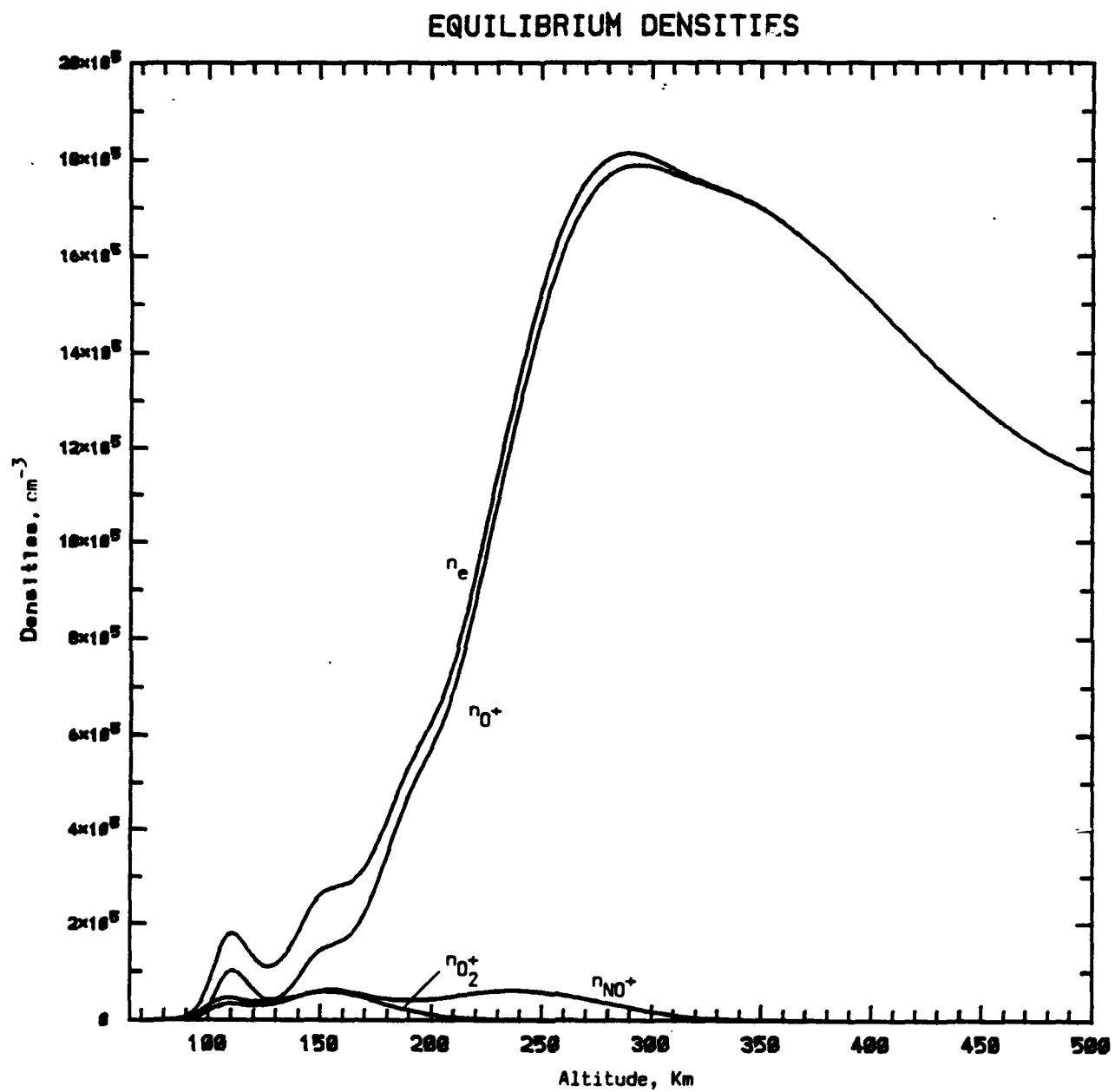


Figure 7-4. Equilibrium Temperature Profiles for Case 0704

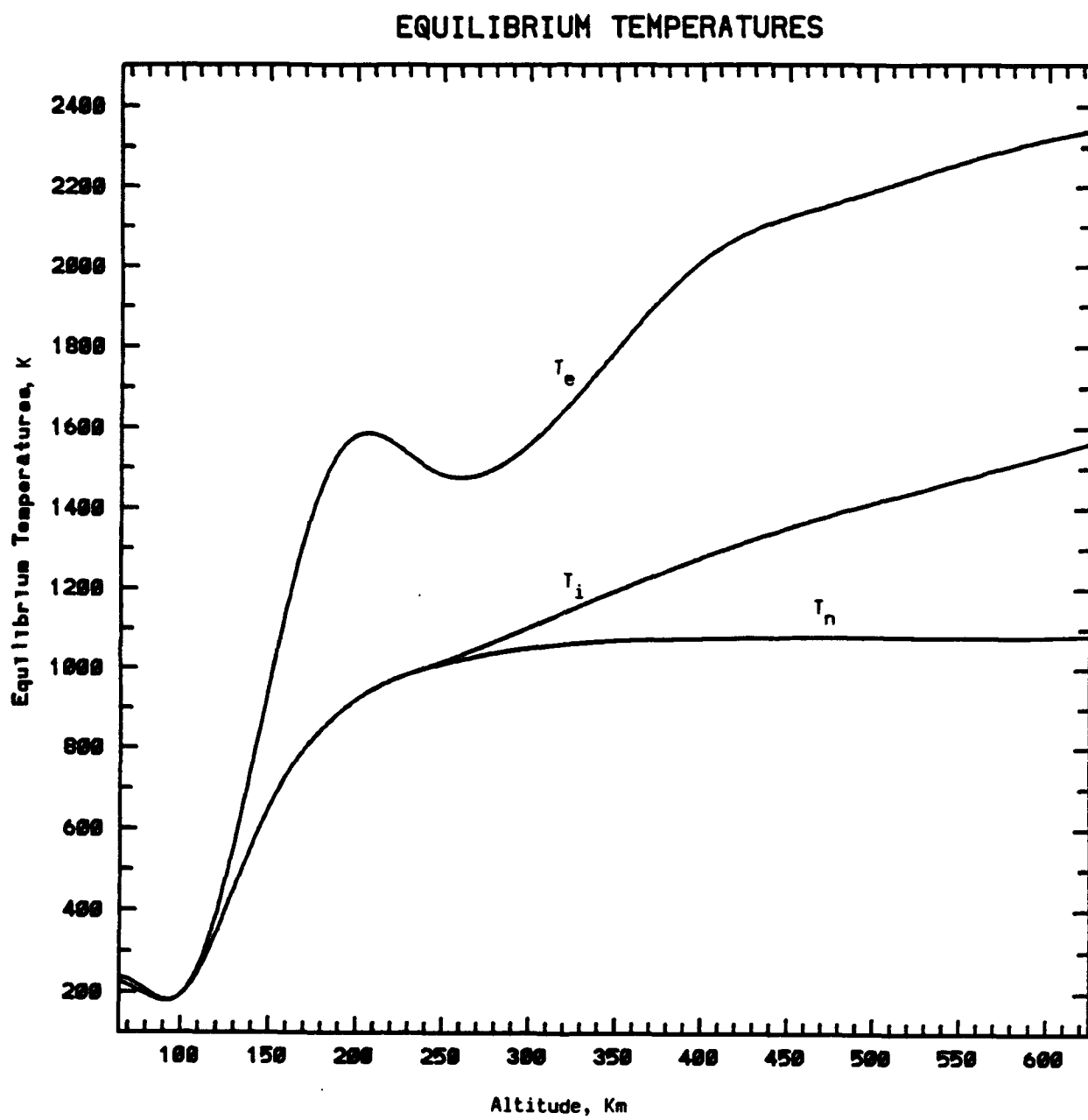
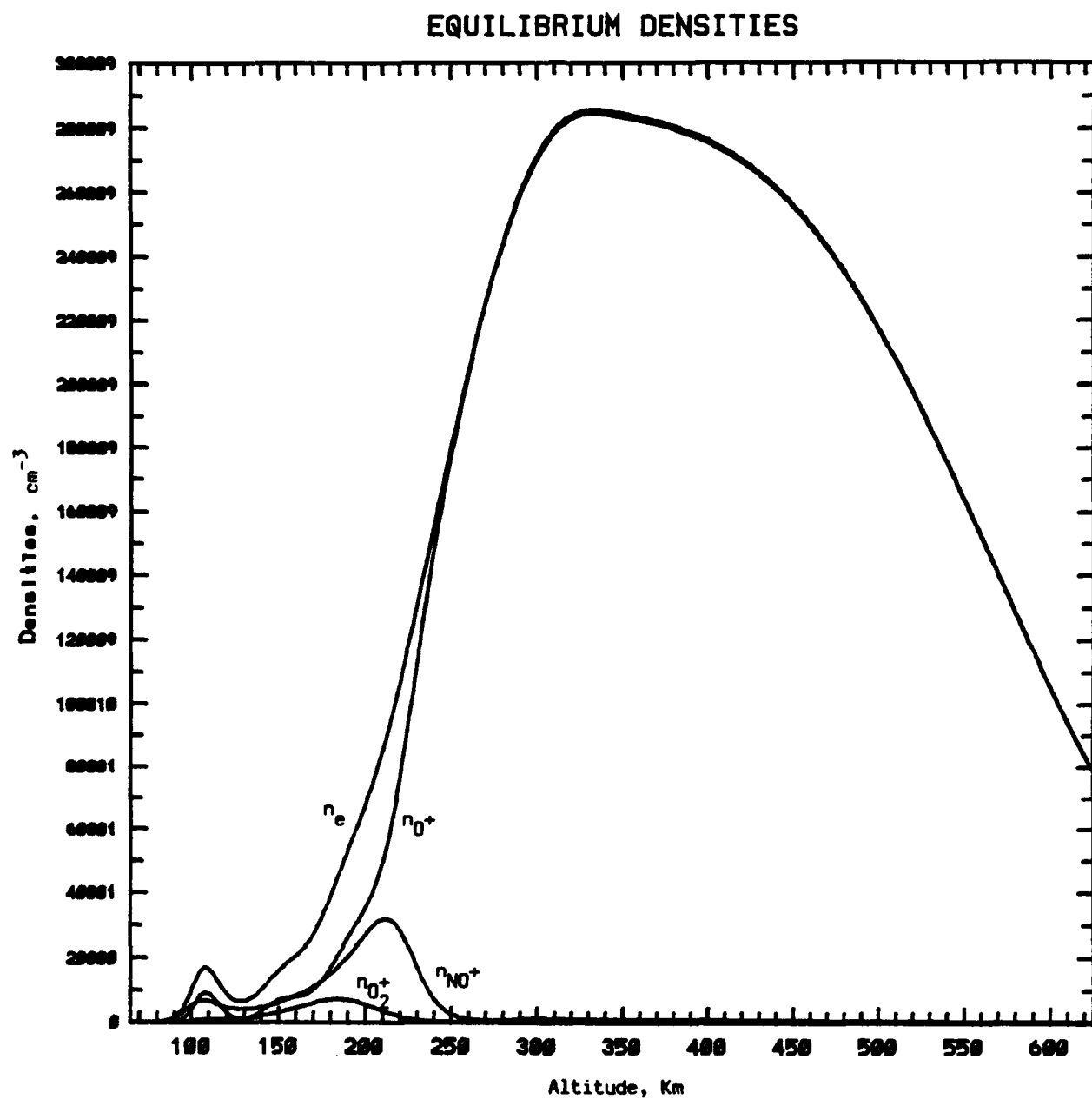


Figure 7-5. Equilibrium Charged Particle Density Profiles for Case 0704



8. COUPLING OF THE WAVE PROPAGATION AND TRANSPORT CODES

The block diagram in Figure 3-3 shows the coupling of the transport code to the wave propagation code. Here the use of the output of the wave propagation code is used as input to the transport code.

An algorithm for projecting the propagating geometric optics rays associated with an HF beam onto the field-aligned transport calculation numerical grid has been devised and implemented. Initially, the rays are traced through the ionosphere to determine the unperturbed trajectories. Then the region of the ionosphere in which the modification is to be calculated is earmarked, and is contained within a volume spanned by the points \underline{r}_1 , \underline{r}_2 , \underline{r}_3 , and \underline{r}_4 . The point \underline{r}_1 is typically chosen so that it is below the bottom-most ray in altitude, near the entry point to the ionosphere, and outside of the beam in the y - z plane. The point \underline{r}_2 is then chosen so that the vector $\underline{r}_2 - \underline{r}_1$ lies along a magnetic field line, with \underline{r}_2 high enough in altitude that all of the HF beam is contained on the field line.

The points \underline{r}_3 and \underline{r}_4 cannot be chosen until the magnetic field coordinate system is established. A magnetic field line is constrained to lie along the direction of the unit vector \underline{e}_3 , where

$$\underline{e}_3 \equiv \frac{B_x}{B} \underline{e}_x + \frac{B_y}{B} \underline{e}_y + \frac{B_z}{B} \underline{e}_z , \quad (1)$$

in the launch point reference frame, and

$$\underline{e}_3 \equiv (0, 0, 1) , \quad (2)$$

in the magnetic field coordinate frame, with

$$B \equiv [B_x^2 + B_y^2 + B_z^2]^{1/2} . \quad (3)$$

The unit vector \underline{e}_2 , which denotes the direction to adjacent magnetic field lines in the same magnetic meridian plane, is

$$\underline{e}_2 \equiv \frac{B_x B_z}{B B_\perp} \underline{e}_x + \frac{B_y B_z}{B B_\perp} \underline{e}_y - \frac{B_\perp}{B} \underline{e}_z , \quad (4)$$

in the launch point frame, and

$$\underline{e}_2 \equiv (0, 1, 0) , \quad (5)$$

in the magnetic field coordinate frame, with

$$B_\perp \equiv [B_x^2 + B_y^2]^{1/2} . \quad (6)$$

Finally, the unit vector \underline{e}_1 defines the direction to an adjacent magnetic meridian plane, and is given by the expressions

$$\underline{e}_1 \equiv \frac{B_y}{B_\perp} \underline{e}_x - \frac{B_x}{B_\perp} \underline{e}_y , \quad (7)$$

in the launch point reference frame, and

$$\underline{e}_1 \equiv (1, 0, 0) . \quad (8)$$

in the magnetic field coordinate frame. There is a well-defined, unitary transformation which links the two reference frames, namely,

$$\begin{pmatrix} \mathbf{e}_1 \\ \mathbf{e}_2 \\ \mathbf{e}_3 \end{pmatrix}_{\text{l.p. frame}} = \underline{R} \cdot \begin{pmatrix} \mathbf{e}_1 \\ \mathbf{e}_2 \\ \mathbf{e}_3 \end{pmatrix}_{\vec{B} \text{ frame}} \quad (9)$$

$$\begin{pmatrix} \mathbf{e}_1 \\ \mathbf{e}_2 \\ \mathbf{e}_3 \end{pmatrix}_{\vec{B} \text{ frame}} = \underline{R}^{-1} \cdot \begin{pmatrix} \mathbf{e}_1 \\ \mathbf{e}_2 \\ \mathbf{e}_3 \end{pmatrix}_{\text{l.p. frame}} \quad (10)$$

where

$$\underline{R} = \begin{pmatrix} B_y/B_{\perp} & B_z B_z/BB_{\perp} & B_z/B \\ -B_x/B_{\perp} & B_y B_z/BB_{\perp} & B_y/B \\ 0 & -B_{\perp}/B & B_z/B \end{pmatrix}, \quad (11)$$

and $\underline{R}^{-1} = \underline{R}^T$, so that $\underline{R} \cdot \underline{R}^T = 1$.

The point \mathbf{r}_3 is constrained to lie in the plane determined by the points \mathbf{r}_1 , $\mathbf{r}_1 + \Delta s_3 \mathbf{e}_3$, and $\mathbf{r}_1 + \Delta s_2 \mathbf{e}_2$; i.e., the $\mathbf{e}_2 - \mathbf{e}_3$ plane, which is that of the magnetic meridian. Typically, \mathbf{r}_3 is at the same altitude as \mathbf{r}_1 (on the bottomside of the beam in the x-y plane), but on the side of the beam opposite to \mathbf{r}_1 in the y-z plane.

Finally, the point \mathbf{r}_4 must lie in the $\mathbf{e}_2 - \mathbf{e}_3$ plane, so that

$$(\mathbf{r}_4 - \mathbf{r}_1) \cdot \mathbf{e}_2 = 0, \quad (12)$$

i.e., $(\mathbf{r}_4 - \mathbf{r}_1)$ has a component across meridian planes as well as along magnetic field lines, but not a component in the direction between adjacent field lines in the same meridian plane. Figures 8-1, 8-2, and 8-3 show the unperturbed rays in the x-z, y-z, and x-y planes, respectively, as well as the locations of \mathbf{r}_1 , \mathbf{r}_2 , \mathbf{r}_3 , and \mathbf{r}_4 for case 0112. Figures 8-4, 8-5, and 8-6 depict the unperturbed rays in the x-z, y-z, and x-y planes, respectively, with the locations of \mathbf{r}_1 , \mathbf{r}_2 , \mathbf{r}_3 , and \mathbf{r}_4 denoted, for case 0704.

Once the points \mathbf{r}_1 , \mathbf{r}_2 , \mathbf{r}_3 , and \mathbf{r}_4 are determined, a numerical grid is established. A numerical interpolation of the electric field \underline{E} is performed at specific points along a magnetic field line, whose bottommost grid point is

$$\mathbf{s}_0 = \mathbf{r}_1 + \frac{\mathbf{r}_4 - \mathbf{r}_1}{\# \text{ planes} - 1} \times i + \frac{\mathbf{r}_3 - \mathbf{r}_1}{\# \text{ lines} - 1} \times j, \quad (13)$$

where $i < \# \text{ planes}$, and $j < \# \text{ lines}$. The spline fit call is made to retrieve the electron density and temperature at the point of interpolation so that the quantity

$$Q_{\text{hf}} = \text{Re} \langle \underline{E}^* \cdot \underline{J} \rangle. \quad (14)$$

at each grid point along each field line in each meridian plane is determined. Samples of Q_{hf} profiles for cases 0112 and 0704 are exhibited in Figures 8-7 and 8-8.

An effort has been made to assess just how large the density modifications must be in order for the rays to be affected. Thus, a Gaussian ball of density was non-self-consistently introduced into the ray tracing code, so that

$$n(\mathbf{r}) = n_0(\mathbf{r}) + \delta n \exp[-(x^2/a^2 + y^2/b^2 + z^2/c^2)]. \quad (15)$$

The parameter δn can be either positive or negative. It was found that for case 0112, when $\delta n \sim .2n_0$ and is situated at an altitude of 100 km along the center of the beam, the rays are nominally disturbed. The ray paths are displayed in Figures 8-9 through 8-11 when this density modification is included.

This is tantamount to allowing the density and temperature modifications to saturate in the lower ionosphere, which occurs within two minutes of heating. Based upon this analysis, it was decided to allow the density and temperature modifications to evolve for two minutes before performing the feedback calculation.

8-1. Daytime Heating - Case 0112

For the daytime scenario described in Section 7-6, Figures 8-12 through 8-18 display the modification which occurs. The data shown is from field line #6 on plane 10, where the pump is centered at an altitude of roughly 100 km. Since the daytime density is so high ($\sim 2 \times 10^6 \text{ cm}^{-3}$ at the peak of the profile), the rays never get higher than 180 km in altitude. The frequency of the HF beam is 15 MHz for this case.

Figure 8-12 depicts the coefficient of thermal conductivity, K_e , normalized to $\alpha L_n^2 k n_{e00}$, where

$$L_n \equiv \text{ionospheric scale length} = 5 \times 10^6 \text{ cm} \quad (16)$$

$$k \equiv \text{Boltzmann's constant} \quad (17)$$

$$n_{e00} \equiv n_0(s = s_{upper}) \quad (18)$$

$$\alpha \equiv \frac{2kT_{e00}/m_e}{\nu L_n^2} \quad (19)$$

$$T_{e00} \equiv T_0(s = s_{upper}) \quad (20)$$

$$\nu \equiv \text{a characteristic ionospheric collision frequency} = 4.444 \times 10^2 \text{ s}^{-1} \quad (21)$$

Essentially, K_e is zero in the vicinity of the beam. Corrections introduced by the convective and pressure flux terms are even smaller than that of the thermal conductivity term^[6]. Thus, for this case, the heating is local in nature, as is evidenced in Figures 8-13a and 8-13b. Figure 8-13a depicts T_e vs. altitude, plotted at 6 second intervals for the duration of heating (2 minutes). Figure 8-13b is a plot of $\delta T_e(s) = [T_e(s, t)/T_e(s, t = 0) - 1]$ vs. altitude at 6 second intervals. The peak modification normalized to the background is on the order of 75%, and is self-similar to the pump shape. A typical run was also done which included the thermal conductivity, convective term, and pressure flux term. There is no significant change in the output when these terms are excluded below 140 km in altitude. They are, however, necessary and important above 140 km in altitude, and are retained when the pump center falls above this point.

Figure 8-13c exhibits $\delta T_e(s)$ near the peak of the profile vs. time. The changes in the electron temperature saturate quickly on a short time scale; there is also a slight decrease in δT_e on a longer time scale (\sim minutes), which is in response to the density modifications. The density increases on the long time scale in the vicinity of the pump, and thus there are more particles to heat than in the early heating stage. As a consequence, the electron temperature slightly decreases on the longer time scale.

Figures 8-14 and 8-15 are plots of the electron cooling, $L_e(s)$ vs. altitude, and the electron collision frequency, $\nu_e(s) = \nu_{en} + \nu_{ei}$ vs. altitude, respectively, at 6 second

intervals. The electron cooling shows an increase centered around the pump which saturates on the temperature time scale. The collision frequency also shows an increase centered about the pump. However, as the input energy moves higher in altitude on a field line and enters the region where the collisions are electron-ion in nature rather than electron-neutral, the change in the collision frequency becomes a decrement rather than an increment, because ν_{ei} is inversely proportional to $T_e^{3/2}$, whereas ν_{en} scales as $T_e^{1/2}$.

Figure 8-16a depicts $n_e(s)$ vs. altitude plotted at 6 second intervals over the course of 2 minutes of heating. The density modification normalized to the background density, $\delta n_e(s) = [n_e(s, t)/n_e(s, t = 0) - 1]$ vs. altitude at 6 second intervals is displayed in Figure 8-16b. Figure 8-16c shows $\delta n_e(s)$ near the center of the pump as a function of heating time. The density modification is self-similar to the pump, is an increase rather than a decrease, and saturates on a time scale of minutes rather than seconds. The density increase may be explained by examining Figures 8-17 and 8-18. Figure 8-17 is a plot of the recombination rate, $\beta_e(s)$, vs. altitude at 6 second intervals. It is readily observable that β_e decreases around the pump as heating occurs, because T_e increases [c.f. equations (17), (18), and (22) of Section 7]. Figure 8-18 exhibits the diffusion coefficient, $D(s)$, normalized to $\frac{1}{m_e \nu}$. In the vicinity of the pump, D is essentially zero, and the recombination rate β_e decreases from what it was in equilibrium. However, the source, S_e , is emitting enough photoelectrons to sustain the equilibrium profile. Therefore, the decrease in the recombination rate, β_e , caused by heating, causes an increase in the electron density.

The features of the modification summarized in Figures 8-12 through 8-18 hold on each field line in each meridian plane wherever modification occurs for case 0112. Only the amplitudes of the modifications are altered from field line to field line, and from meridian plane to meridian plane.

8-2. Nighttime Heating - Case 0704

Figures 8-19 through 8-25 describe the density and temperature modifications for a nighttime scenario. The data shown is from field line #9 on plane 20, where the pump is roughly centered at an altitude of 170 km. The quantities n_{e00} and T_{e00} are now normalized to the lowest grid point on the field line rather than the highest grid point,

$$n_{e00} = n_e(s = s_{\text{lower}}) \quad (22)$$

$$T_{e00} = T_e(s = s_{\text{lower}}) . \quad (23)$$

The electron density peaks at a value of about $3 \times 10^5 \text{ cm}^{-3}$. The frequency of the HF beam is set to 10 MHz. Figure 8-19 depicts the coefficient of thermal conductivity, K_e , normalized to $\alpha L_n^2 n_{e00}$. In the vicinity of an altitude of 170 km, K_e is non-zero, and thus it is anticipated that conduction of heat away from where the pump is located will occur. For these nighttime runs, all of the terms in equation (28) of Section 7 were retained when the pump center was higher than 140 km in altitude.

Figures 8-20 exhibit the temperature modifications which take place for case 0704. Figure 8-20a is a plot of T_e along a field line vs. altitude, plotted at 6 second intervals over the course of 2 minutes of heating. There is clearly a change in T_e at locations other than where the pump heats. Figure 8-20b, which displays $\delta T_e(s)$ vs. altitude, shows this phenomenon more clearly. There is a definite conduction of heat to higher altitudes. The

change in δT_e at lower altitude is not as great because K_e is vanishingly small there. Figure 8-20c is a plot of δT_e near the peak of modification vs. time. The electron temperature response time to the heating is on the order of a few seconds.

Figure 8-21 depicts the electron cooling term, $L_e(s)$, vs. altitude at 6 second intervals. There is an increase in L_e of roughly 25% around the pump center, and it essentially occurs within the first 6 seconds. Figure 8-22 displays the electron collision frequency $\nu_e(s) = \nu_{en} + \nu_{ei}$ vs. altitude at 6 second intervals throughout the course of heating. Below an altitude of roughly 220 km, the electron collision frequency increases by 6%, and is self-similar to the pump shape. Above 220 km, the electron collision frequency changes due to temperature modifications by a decrement of 1.5%.

Figure 8-23a displays $n_e(s)$ vs. altitude at 6 second intervals. The density modification normalized to the equilibrium density, $\delta n_e(s)$, is plotted vs. altitude at 6 second intervals, and is shown in Figure 8-23b. Figure 8-23c exhibits $\delta n_e(s)$ near the pump center as a function of heating time. Above an altitude of 220 km, δn_e is negative. The density changes never saturate, in agreement with Hansen^[12], who heated on the order of 10 minutes, and still did not see a steady state achieved while heating a nighttime ionosphere.

The behavior of δn_e is better understood upon examination of Figures 8-24 and 8-25. Figure 8-24 is a plot of the recombination rate along the field line, $\beta_e(s)$, vs. altitude. Below an altitude of 220 km, there is a 5 - 10% decrease in β_e . Above an altitude of 220 km, there is roughly a 10% increase in β_e . Figure 8-25 displays the diffusion coefficient, $D(s)$, normalized to $\frac{1}{m_e \nu}$. Above an altitude of 160 km, the diffusion coefficient is greater than zero.

For this nighttime scenario, at an altitude of 220 km, there is a topological change in the density modification. For different electron density and temperature equilibria, this region of topological change will move to a different altitude. For case 0704, below an altitude of 220 km, there is a density increase primarily caused by the decrease in the recombination, as discussed for case 0112. Since in the nighttime scenario, the pump reaches an altitude where there is some thermal conductivity, there is now an increase in T_e at altitudes higher than the pump. This causes a build-up of pressure above the pump center, and thus the digging of a thermal density cavity as discussed by Shoucri et al.^[6] to achieve pressure equilibrium.

An increase in n_e below 220 km in altitude, and a decrease in n_e above 220 km in altitude means that at 220 km in altitude, δn_e is zero. This suggests that perhaps the best manner in which the radar can operate is to align the null point in δn_e near the caustic surface by tuning the antenna to the appropriate frequency. This should minimize the density modifications which occur in the ionosphere.

This null point in δn_e remains at an altitude of 220 km for all field lines on all meridian planes. When the pump is centered at an altitude significantly lower than that of 220 km, only a density increase is observed because the thermal conductivity is vanishingly small. As the HF beam moves higher in altitude, the topological alteration in the density modification is observed.

8-3. Effect of Different Recombination Models

The transport code currently has the capability to handle three different recombination models. The first is that which has already been discussed, namely, that the recombination

rate, β_e , is inversely proportional to T_e raised to some empirically determined power. This model causes a density increase when the pump is centered on a field line at a low altitude.

The second model is that of Hansen^[12]. The recombination rate remains constant in time, but is a function of position. This is handled in the transport code by establishing the recombination rate in equilibrium, but never updating it in time. When this recombinative model is utilized, the only density modifications observed at all altitudes are thermal cavities caused by pressure imbalances. In the lower ionosphere, such density cavities are on the order of 1%. Figure 8-26 is a plot of $\delta T_e(s)$ vs. altitude with $\beta_e(s, t) = \beta_e(s, t = 0)$ for case 0112. Figure 8-27 displays $\delta n_e(s)$ vs. altitude with $\beta_e(s, t) = \beta_e(s, t = 0)$ for case 0112.

The third model is that of Shoucri et al.^[6]; i.e., there is not a recombinative process explicitly included in the model. The recombination term βn_e is lumped in with the source term and is never updated. (In the model of Hansen^[12], n_e is updated in the term $\beta_e n_e$, but β_e is not.) This limit is achieved by setting to zero within the code the molecular ion densities, as then β_e is also zero. When the transport for this limit is examined, it is found that, once again, density modifications at all altitudes are thermal cavities. However, the cavity does not saturate, in accord with Shoucri et al.^[6] Figures 8-28 and 8-29 display $\delta n_e(s)$ vs. heating time when the recombination rate is constant in time, and when the recombination rate is zero, respectively. Clearly, when there is recombination, the modification saturates.

These three limits are realized by setting a switch, "ibeta", to the appropriate value in the input file "ht_oth.da". If "ibeta" = 0, the recombination rate is updated in time; if "ibeta" = 1, the recombination rate is constant in time; if "ibeta" = 2, the recombination rate is zero.

Figure 8-1. Unperturbed Rays in the X-Z Plane for Case 0112

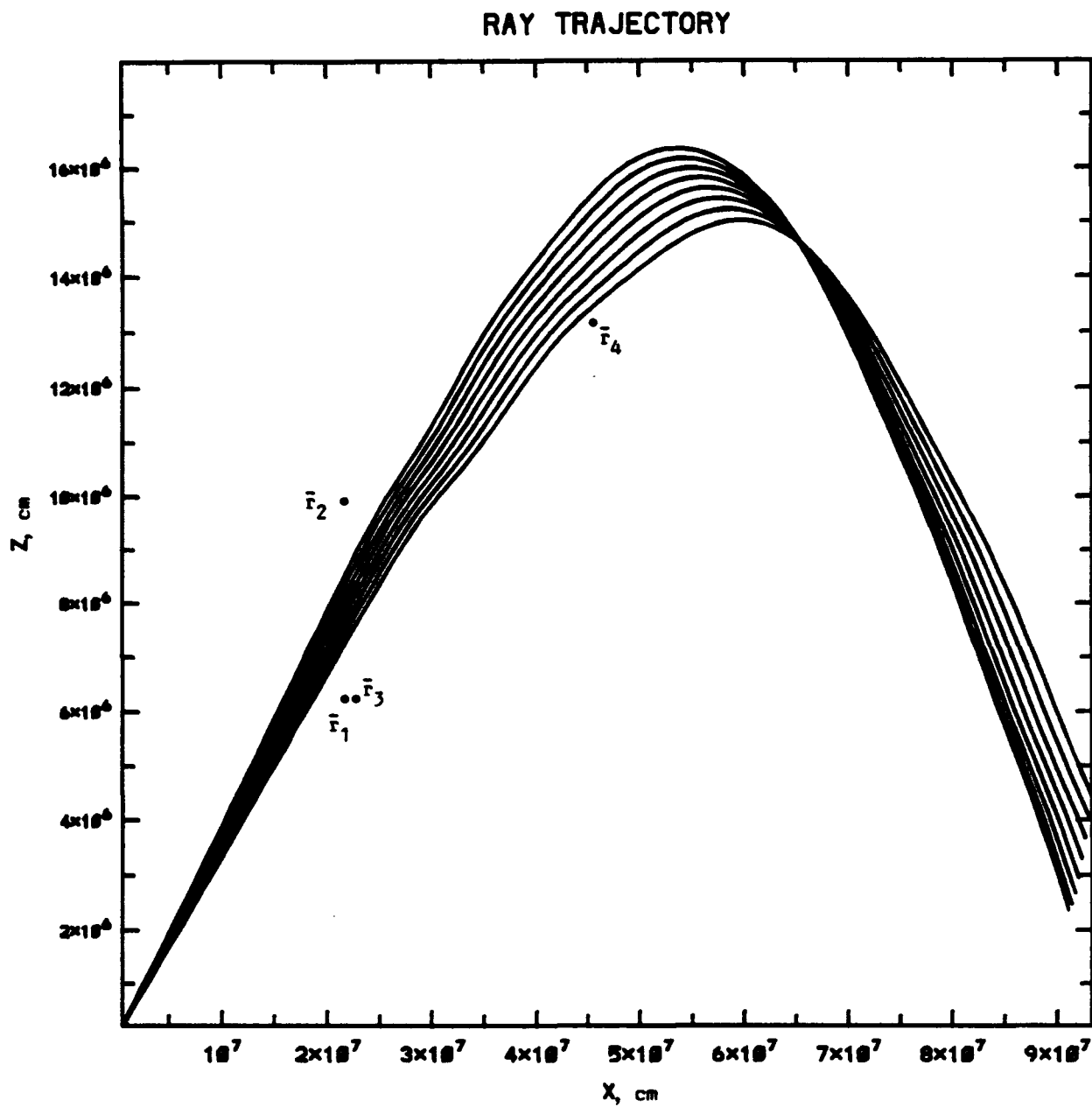


Figure 8-2. Unperturbed Rays in the Y-Z Plane for Case 0112

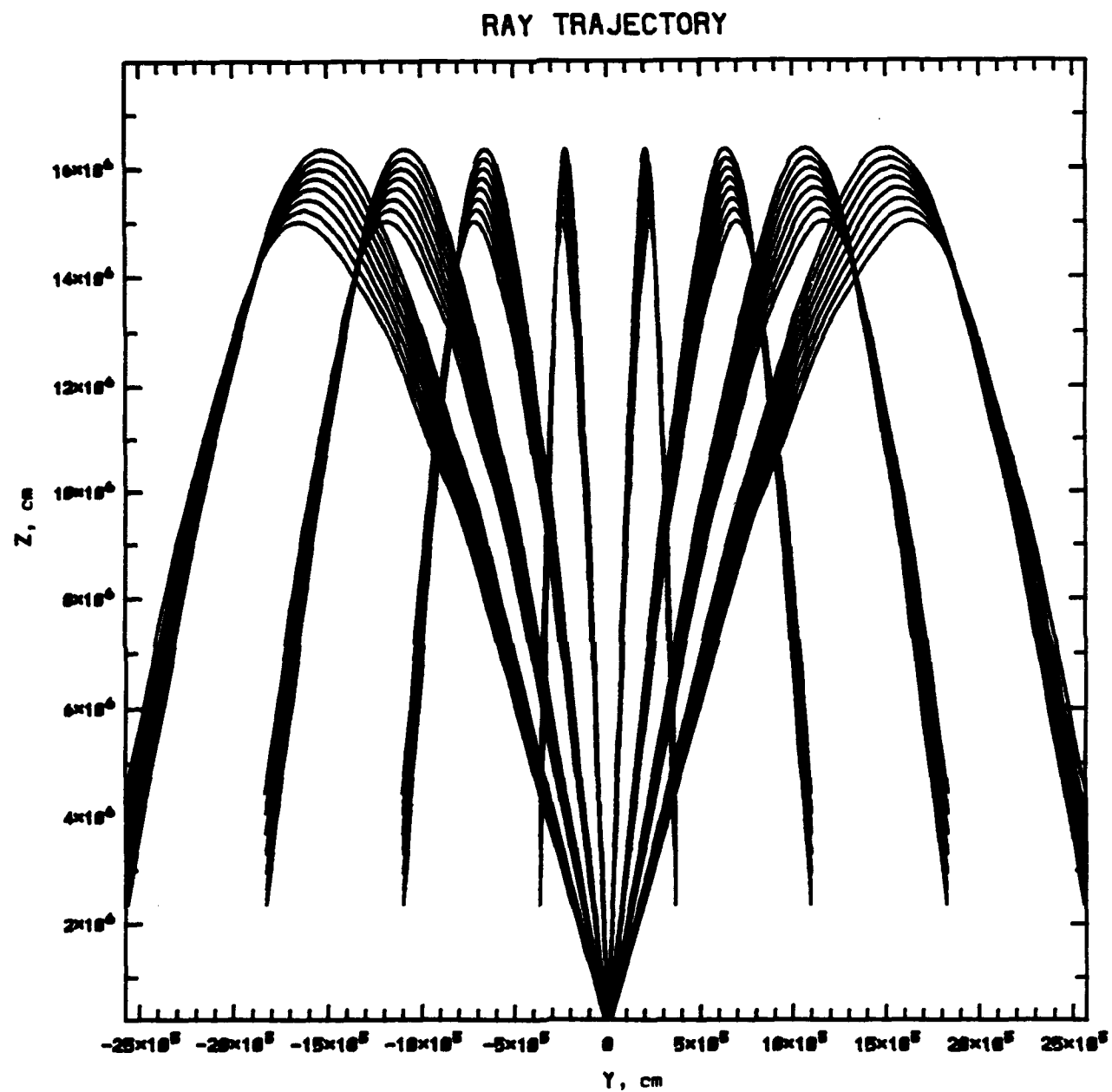


Figure 8-3. Unperturbed Rays in the X-Y Plane for Case 0112

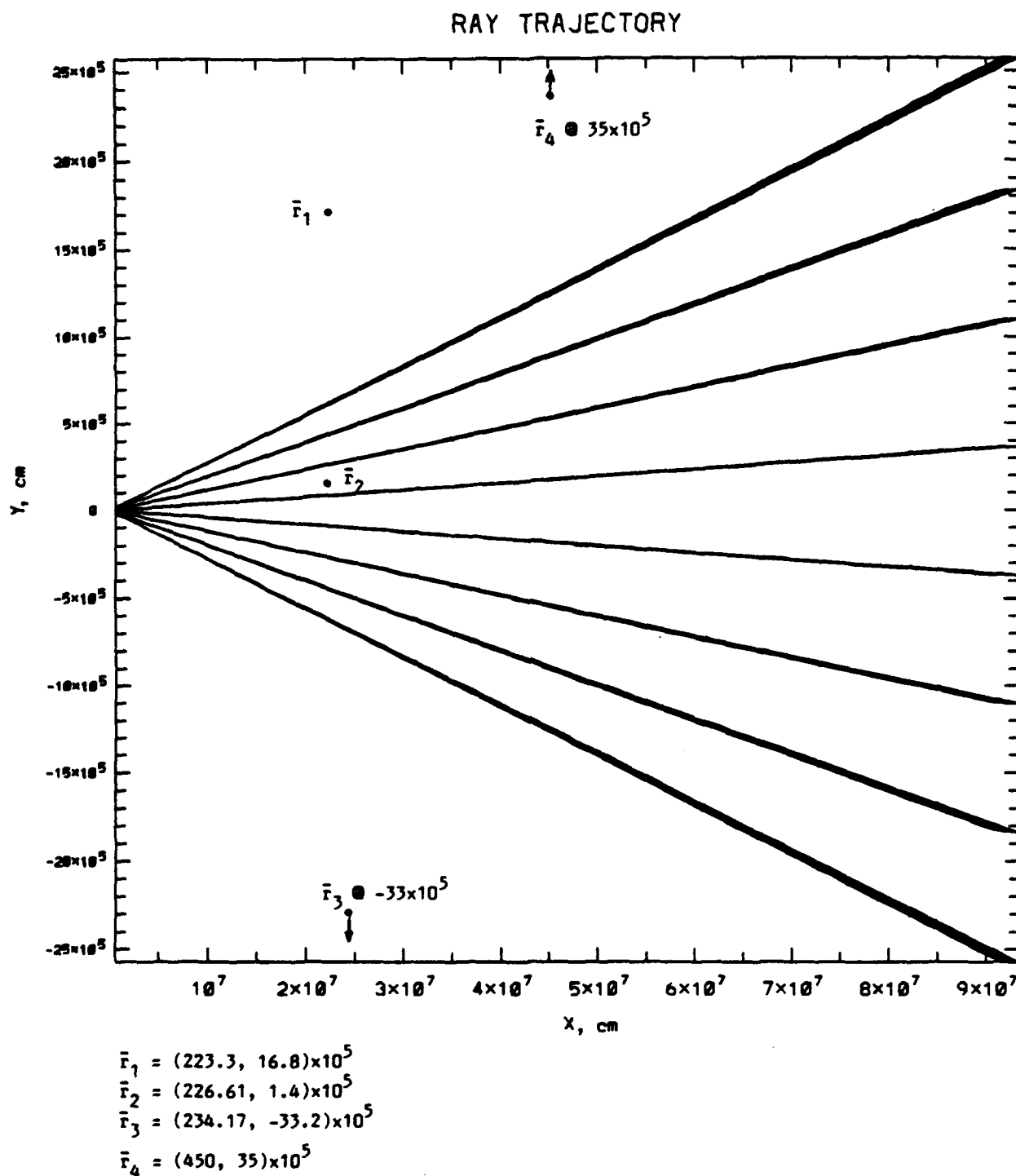


Figure 8-4. Unperturbed Rays in the X-Z Plane for Case 0704

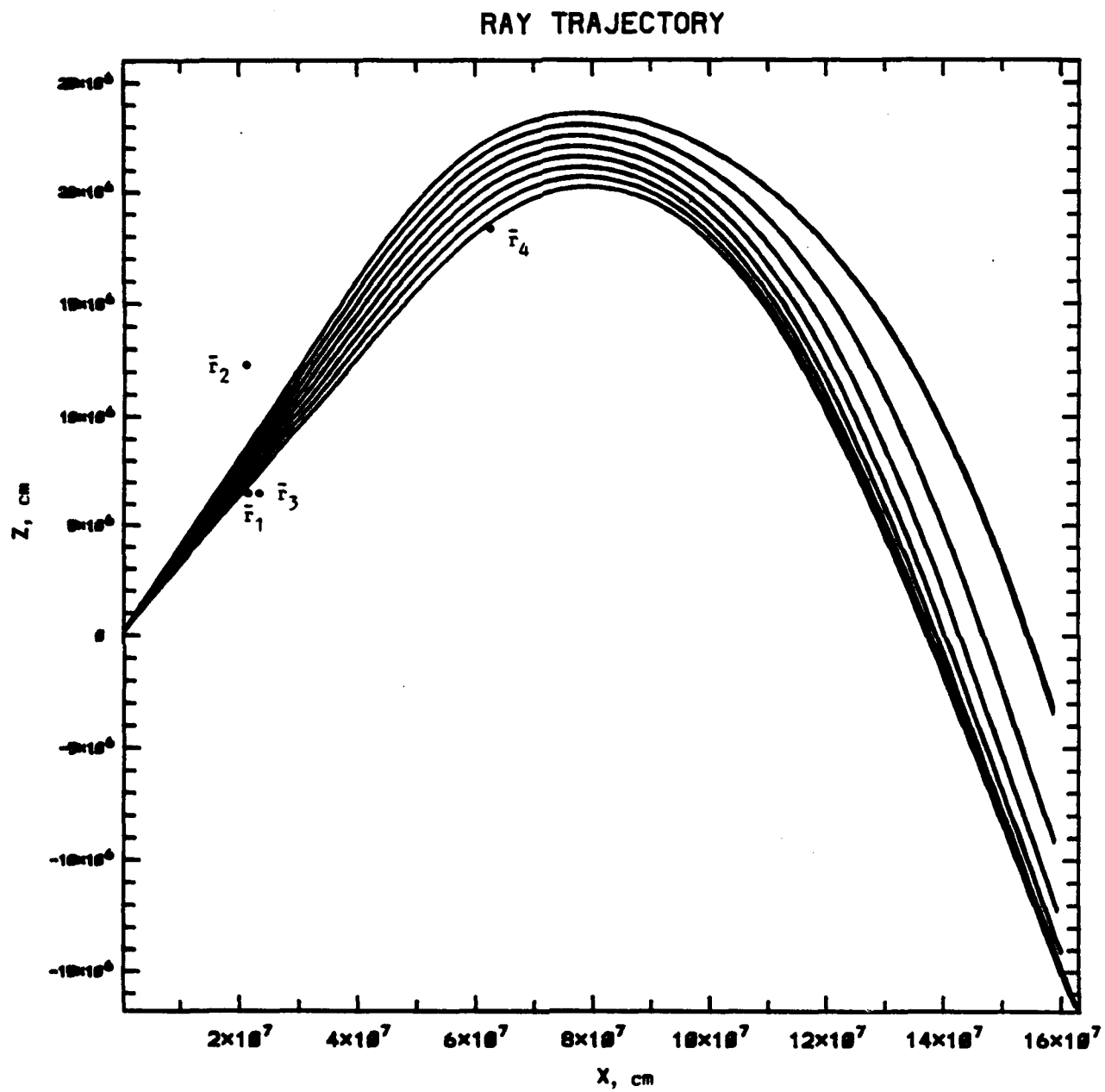


Figure 8-5. Unperturbed Rays in the Y-Z Plane for Case 0704

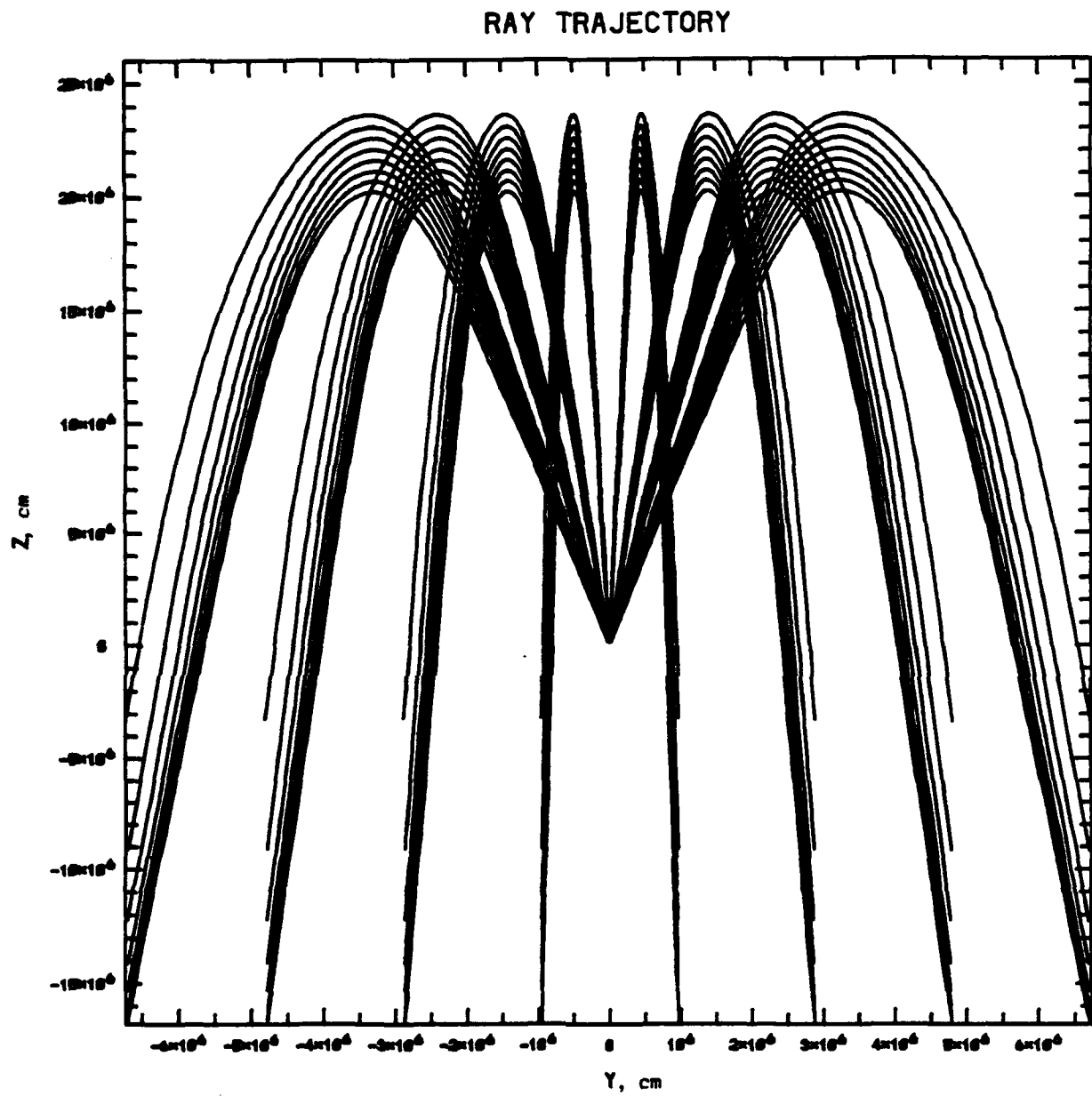


Figure 8-6. Unperturbed Rays in the X-Y Plane for Case 0704

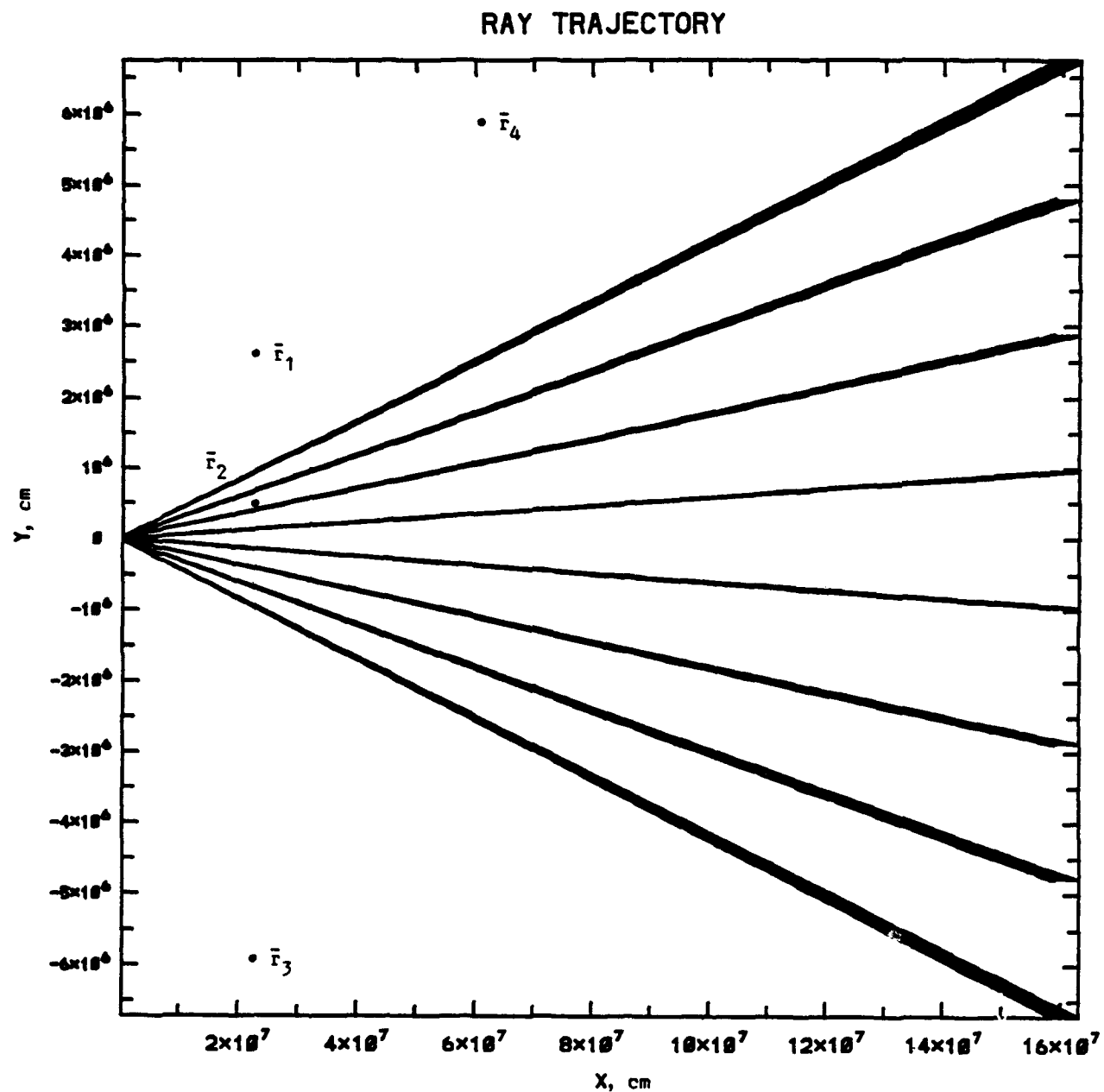


Figure 8-7. Typical Q_{hf} Profile for Case 0112

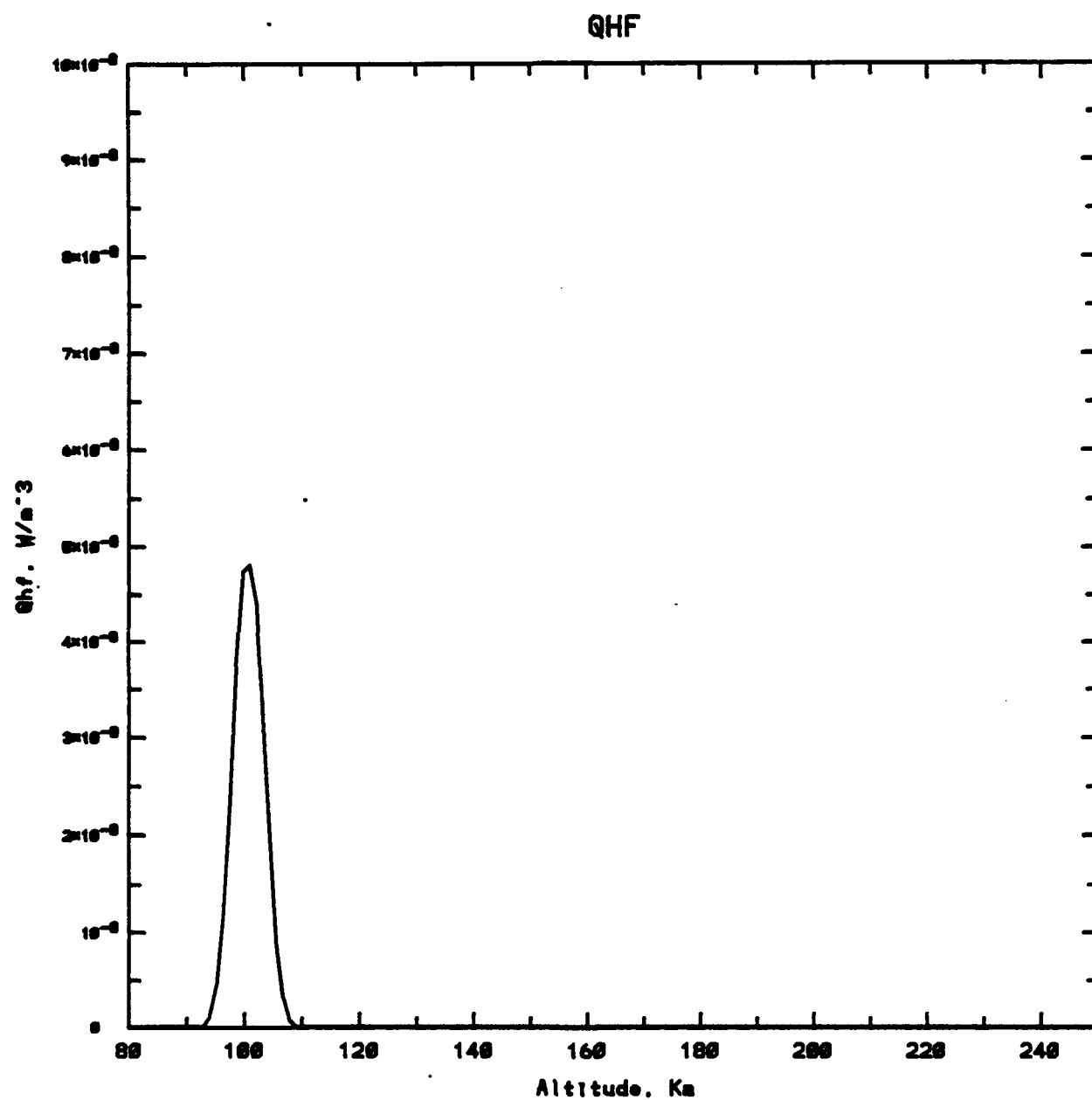


Figure 8-8. Typical Q_{hf} Profile for Case 0704

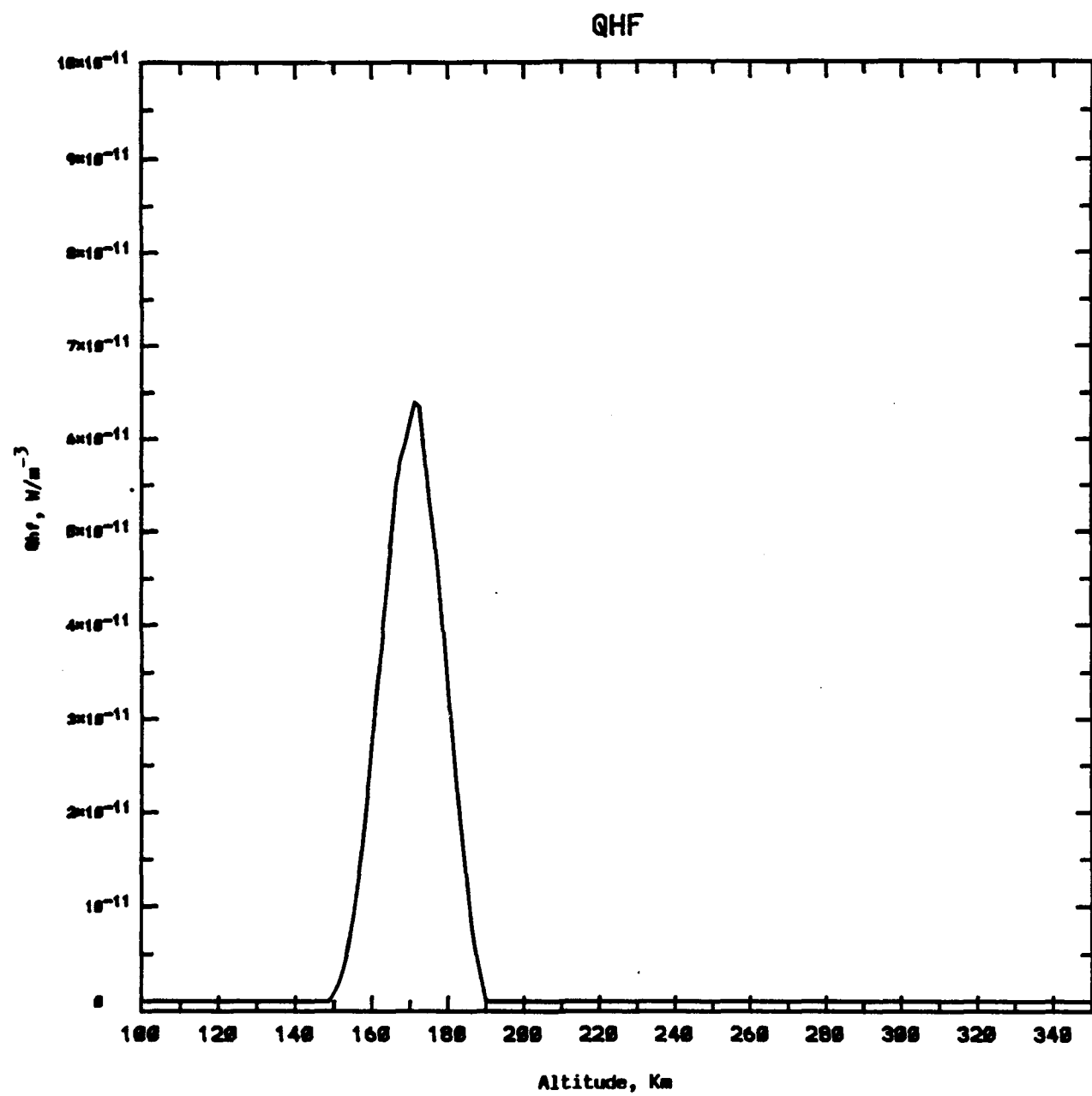


Figure 8-9. Effect of a Non-Self-Consistent Density Perturbation of 20% placed in the E region for Case 0112 (X-Z Plane)

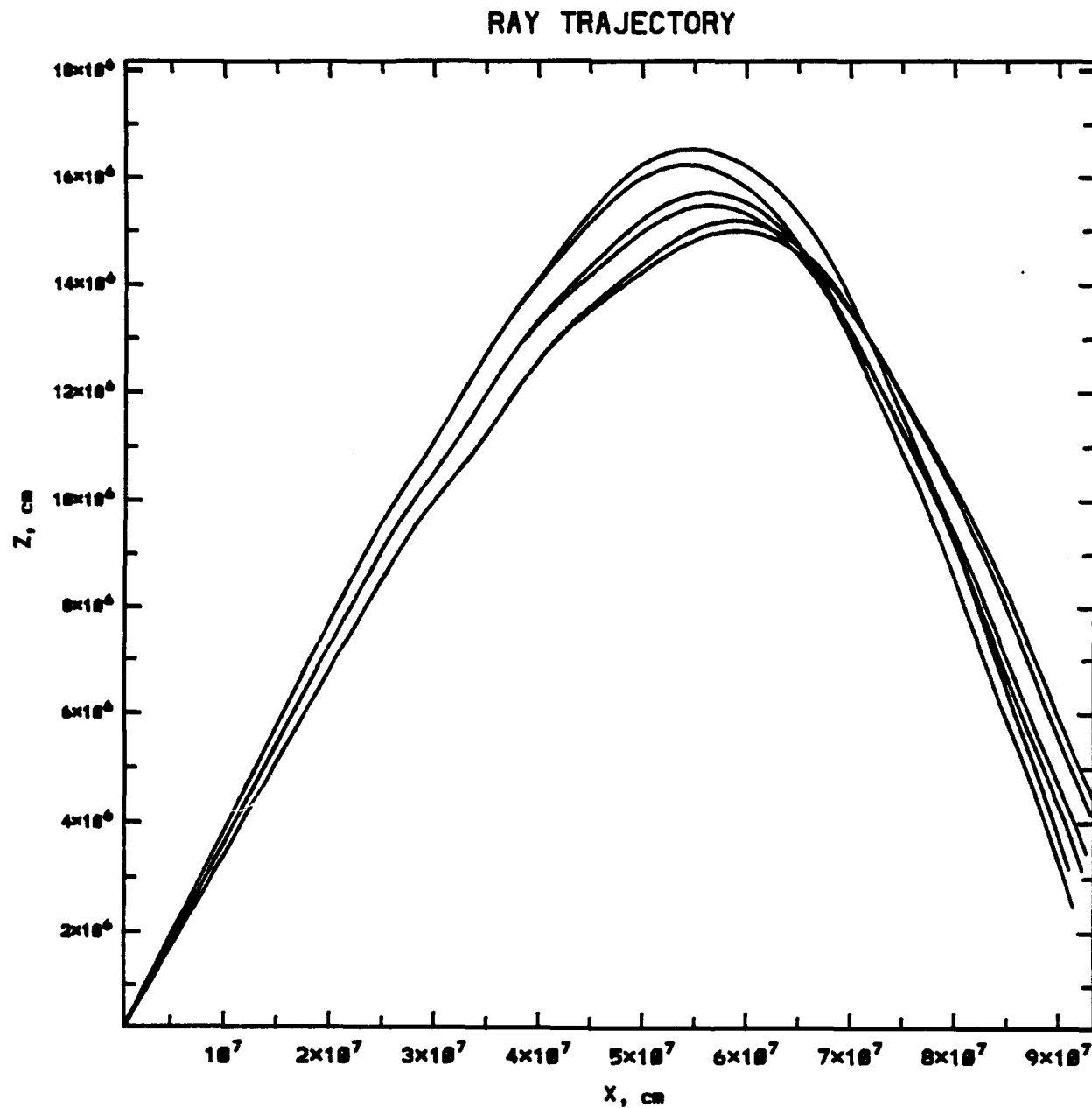


Figure 8-10. Effect of a Non-Self-Consistent Density Perturbation of 20% placed in the E region for Case 0112 (Y-Z Plane)

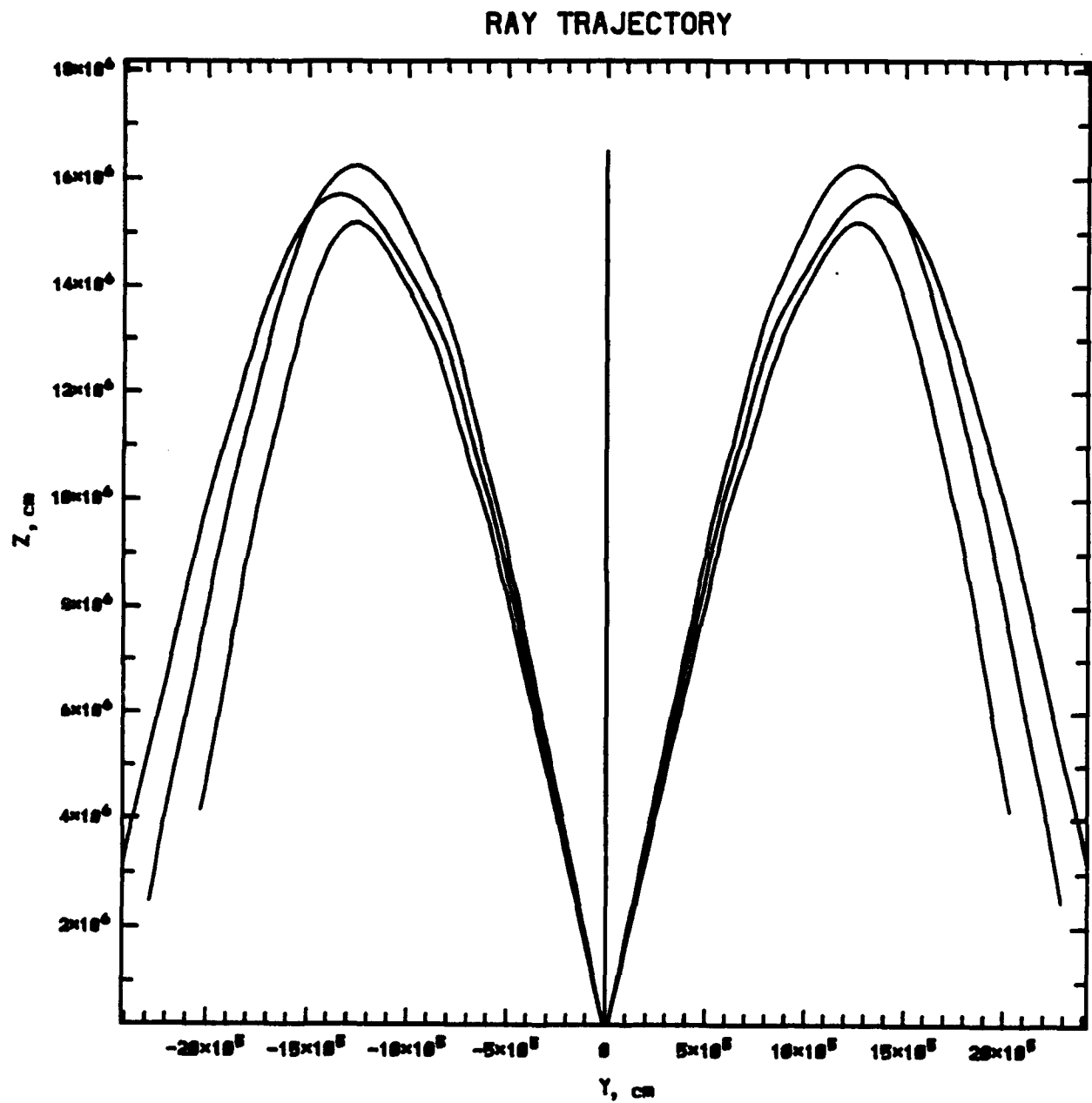


Figure 8-11. Effect of a Non-Self-Consistent Density Perturbation of 20% placed in the E region for Case 0112 (X-Y Plane)

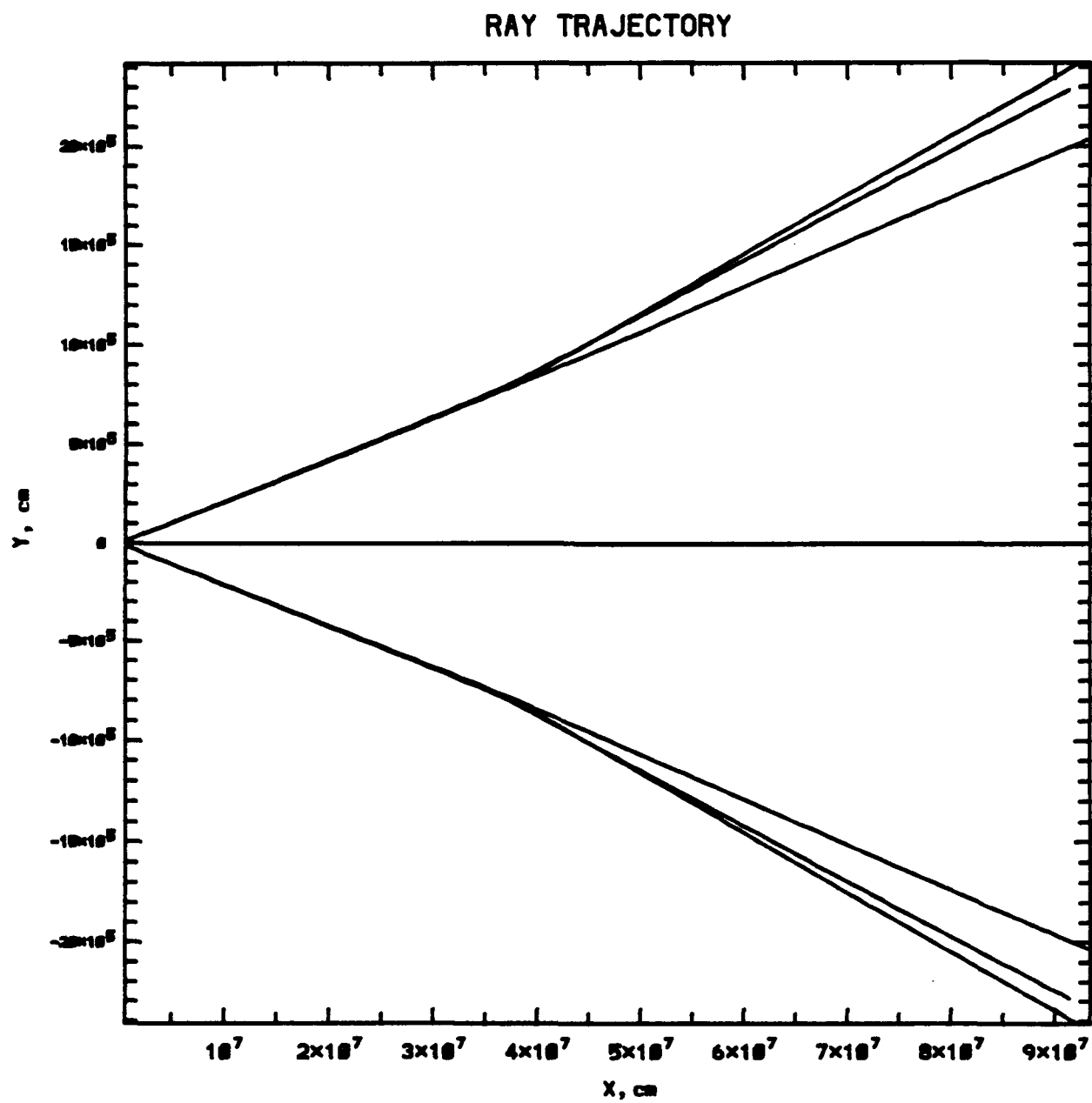


Figure 8-12. Normalized Thermal Conductivity vs. Altitude for Case 0112

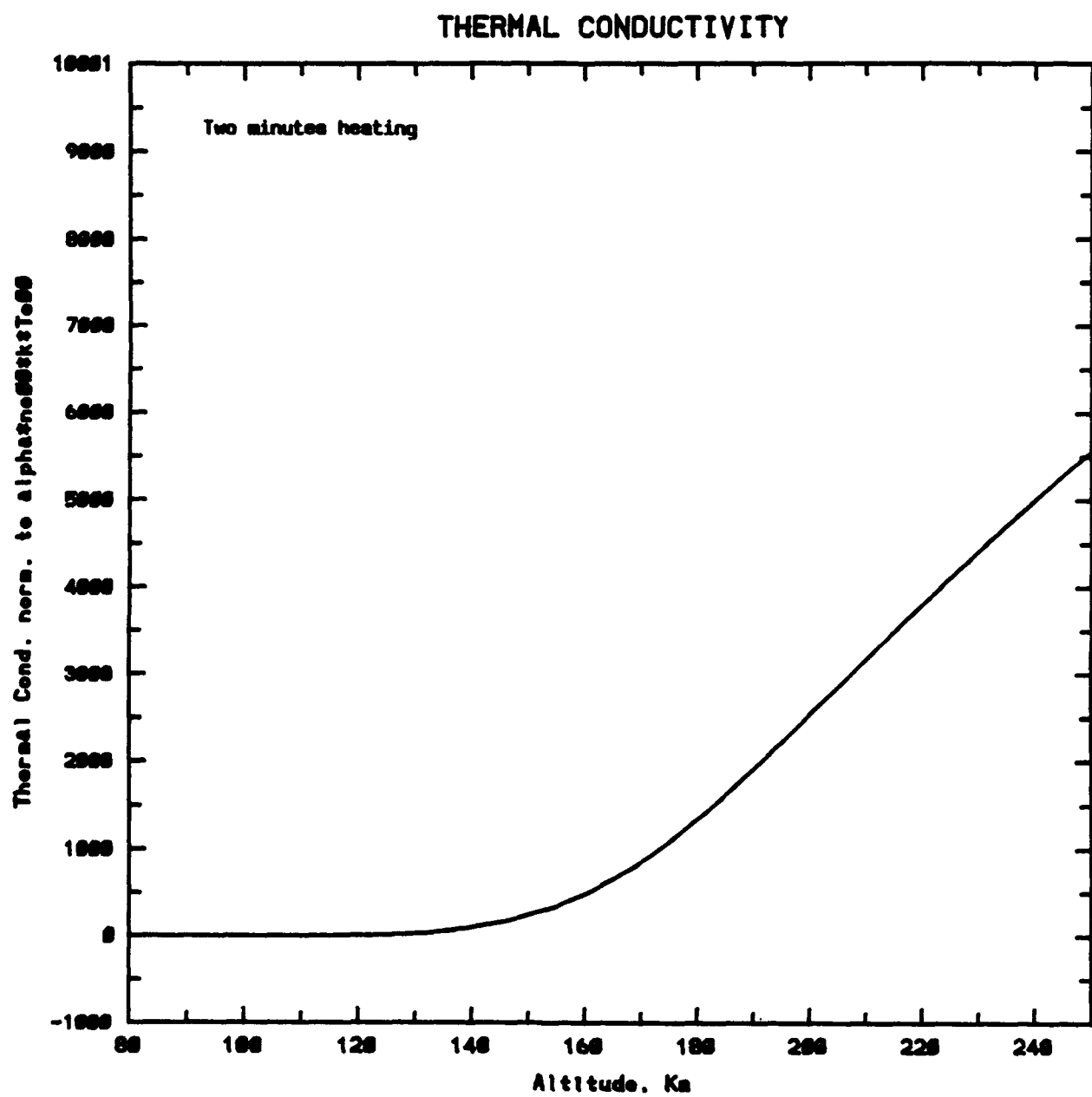
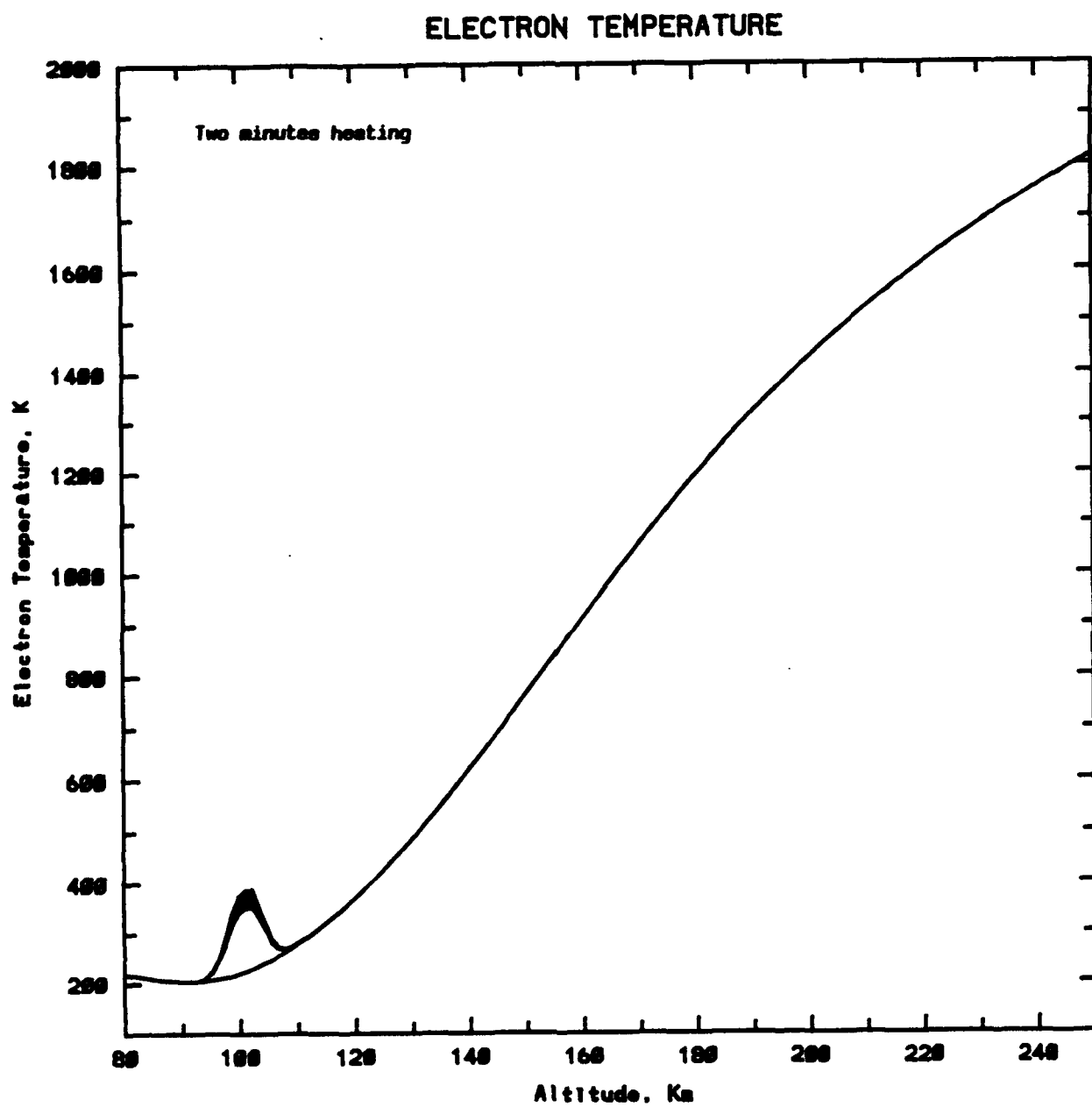
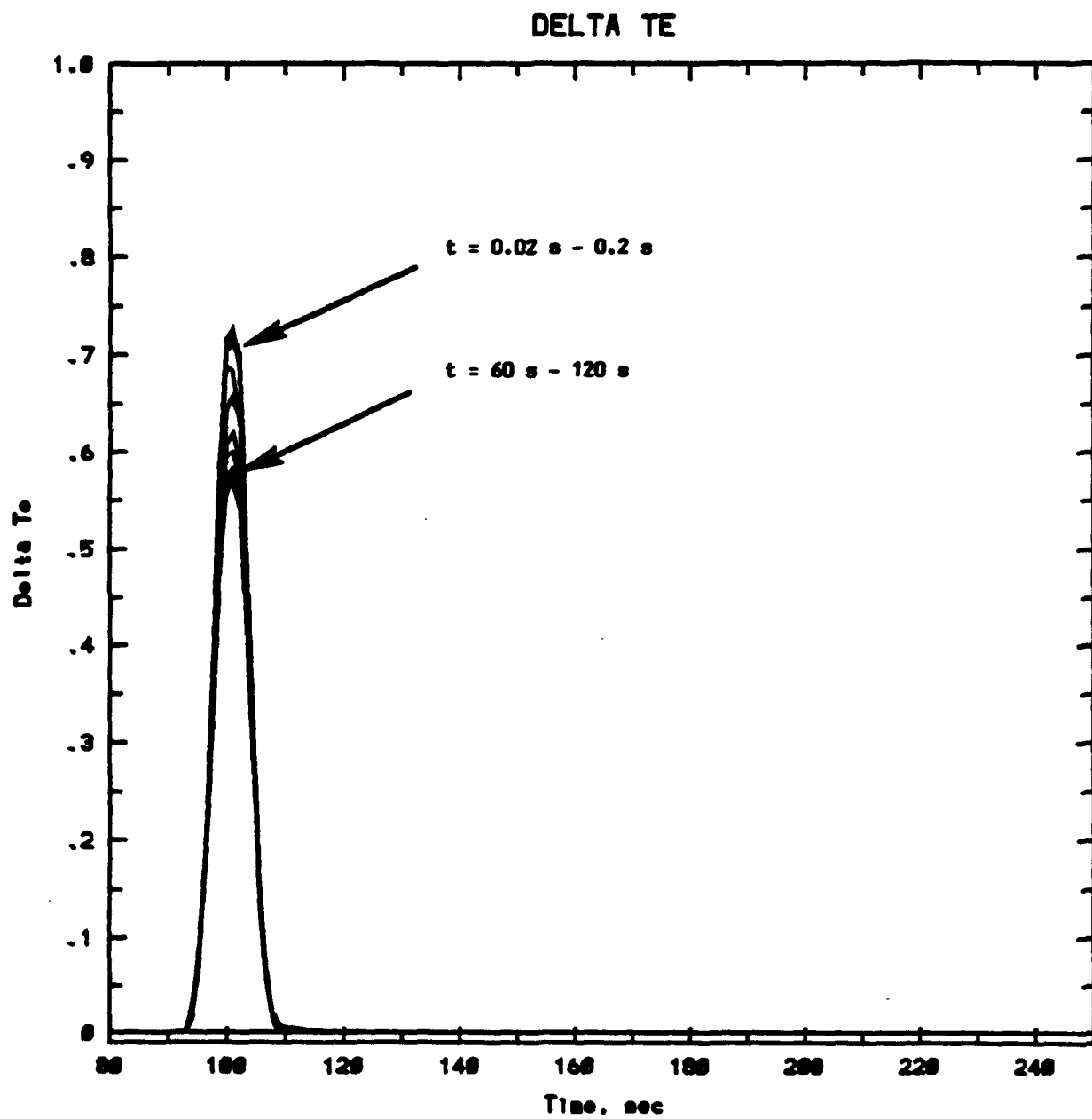


Figure 8-13a. Electron Temperature vs. Altitude for Case 0112



**Figure 8-13b. Normalized Electron Temperature Modification
vs. Altitude for Case 0112**



**Figure 8-13c. Normalized Electron Temperature Modification
vs. Time Near Peak of Q_{lf} Profile for Case 0112**

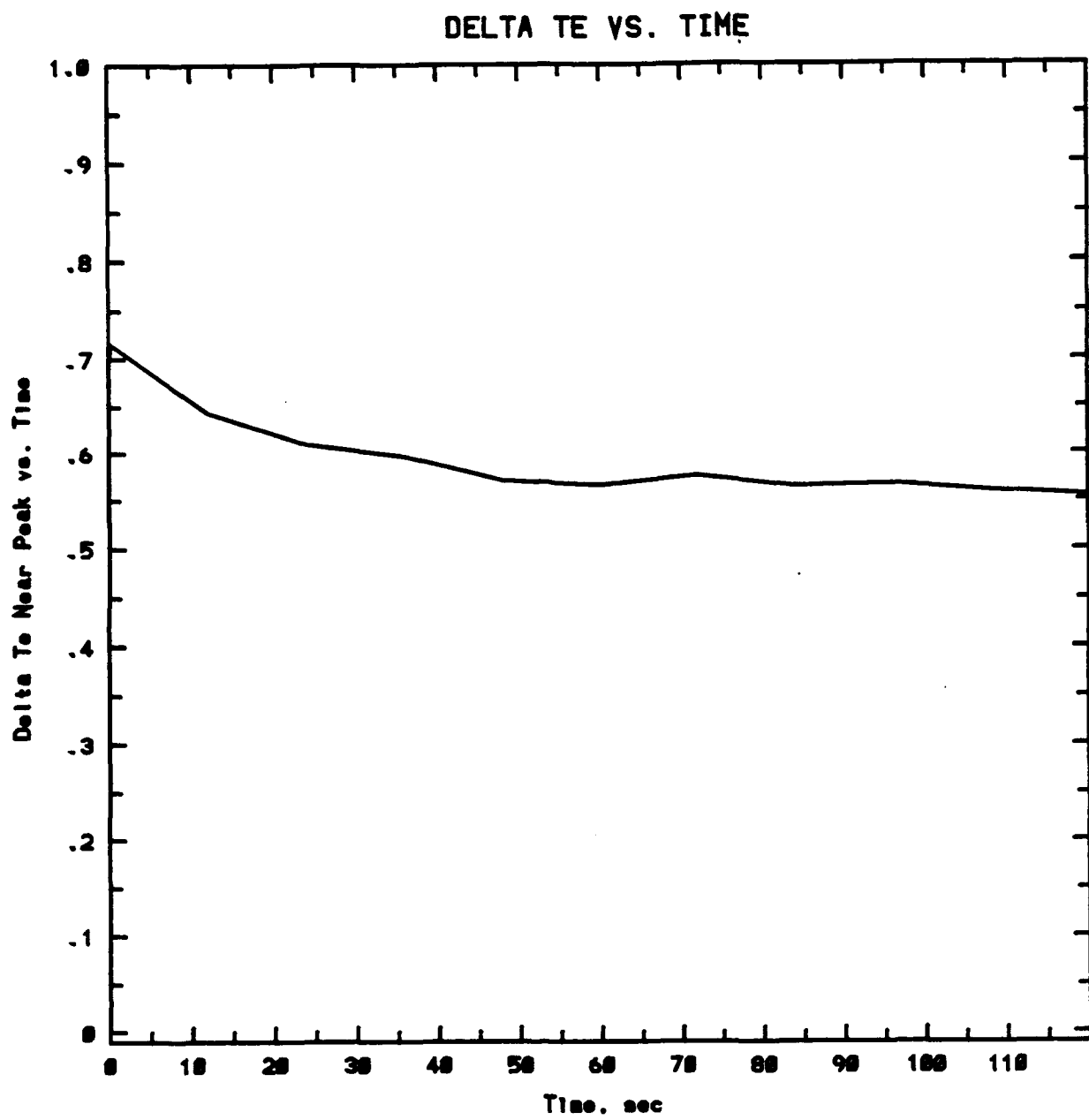
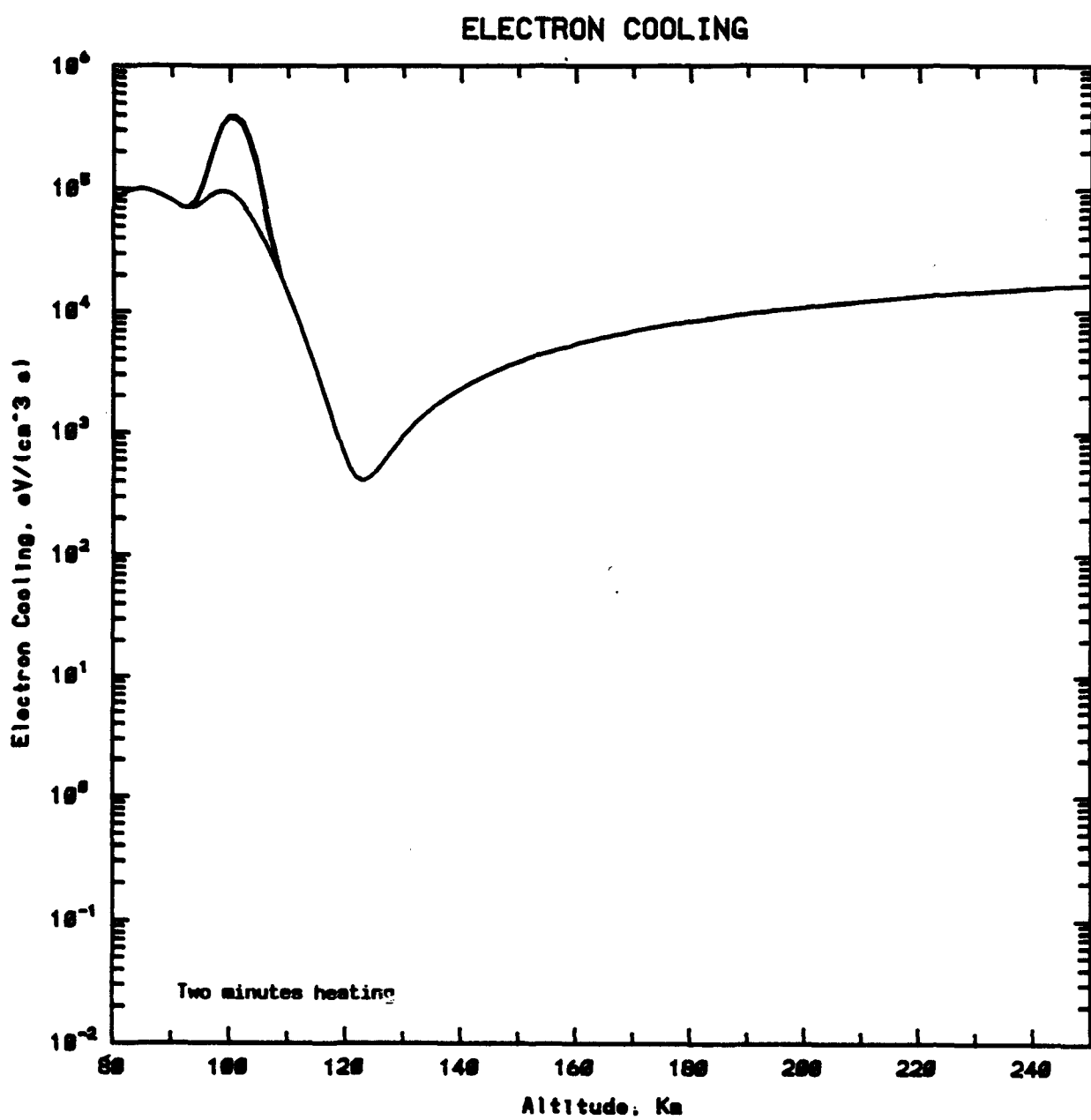


Figure 8-14. Electron Cooling vs. Altitude for Case 0112



**Figure 8-15. Electron Collision Frequency vs. Altitude
for Case 0112**

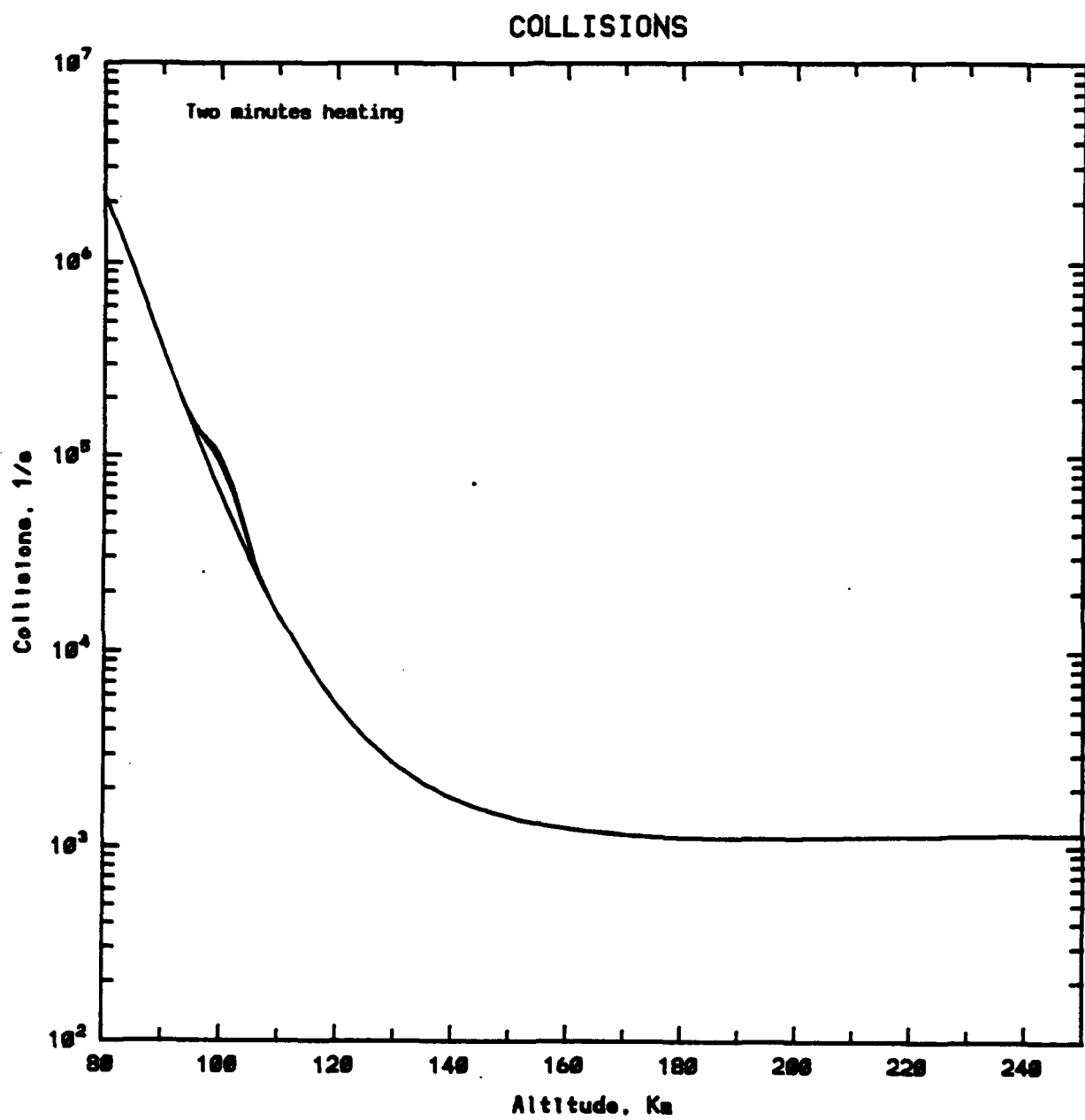


Figure 8-16a. Electron Density vs. Altitude for Case 0112

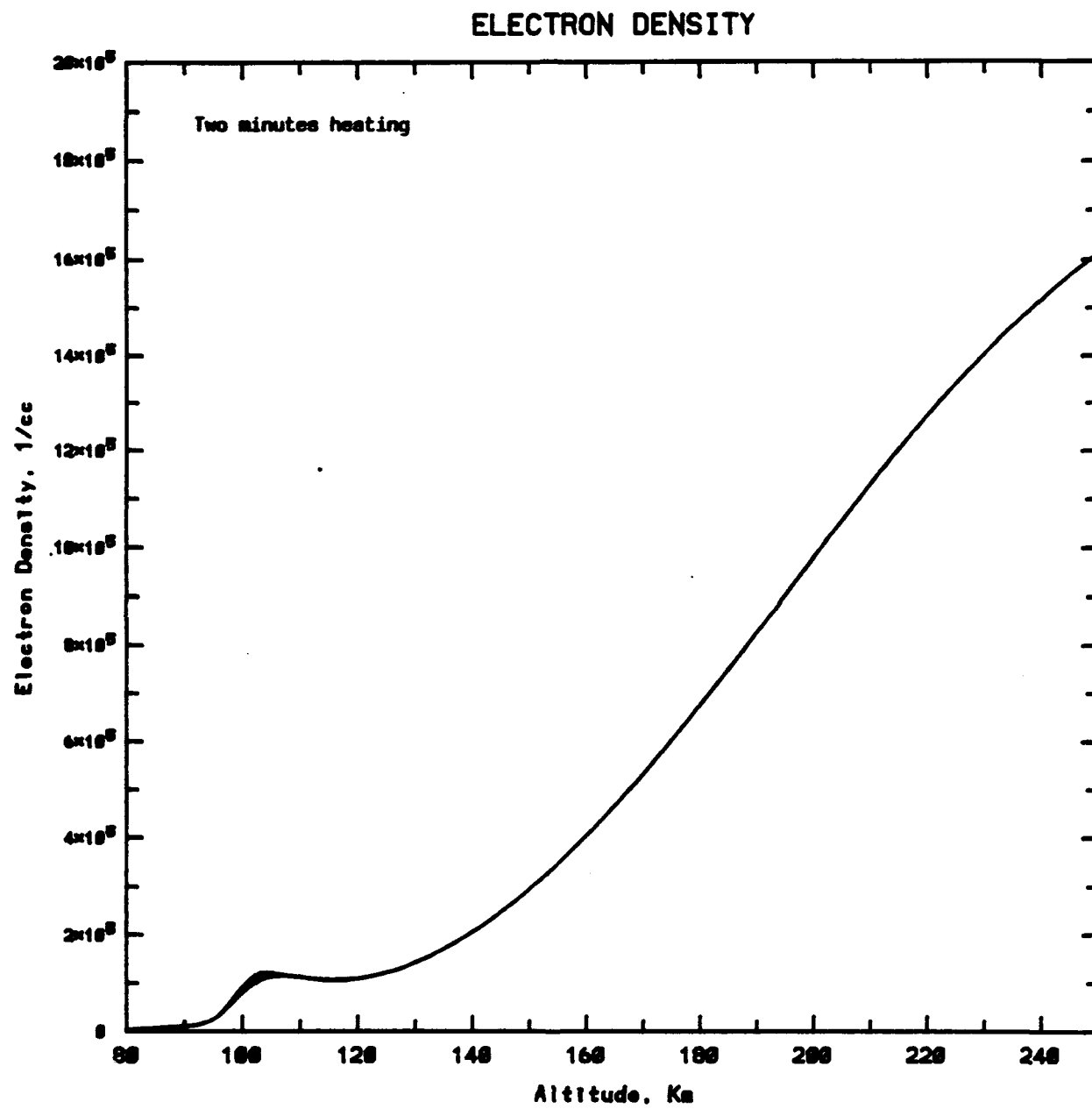
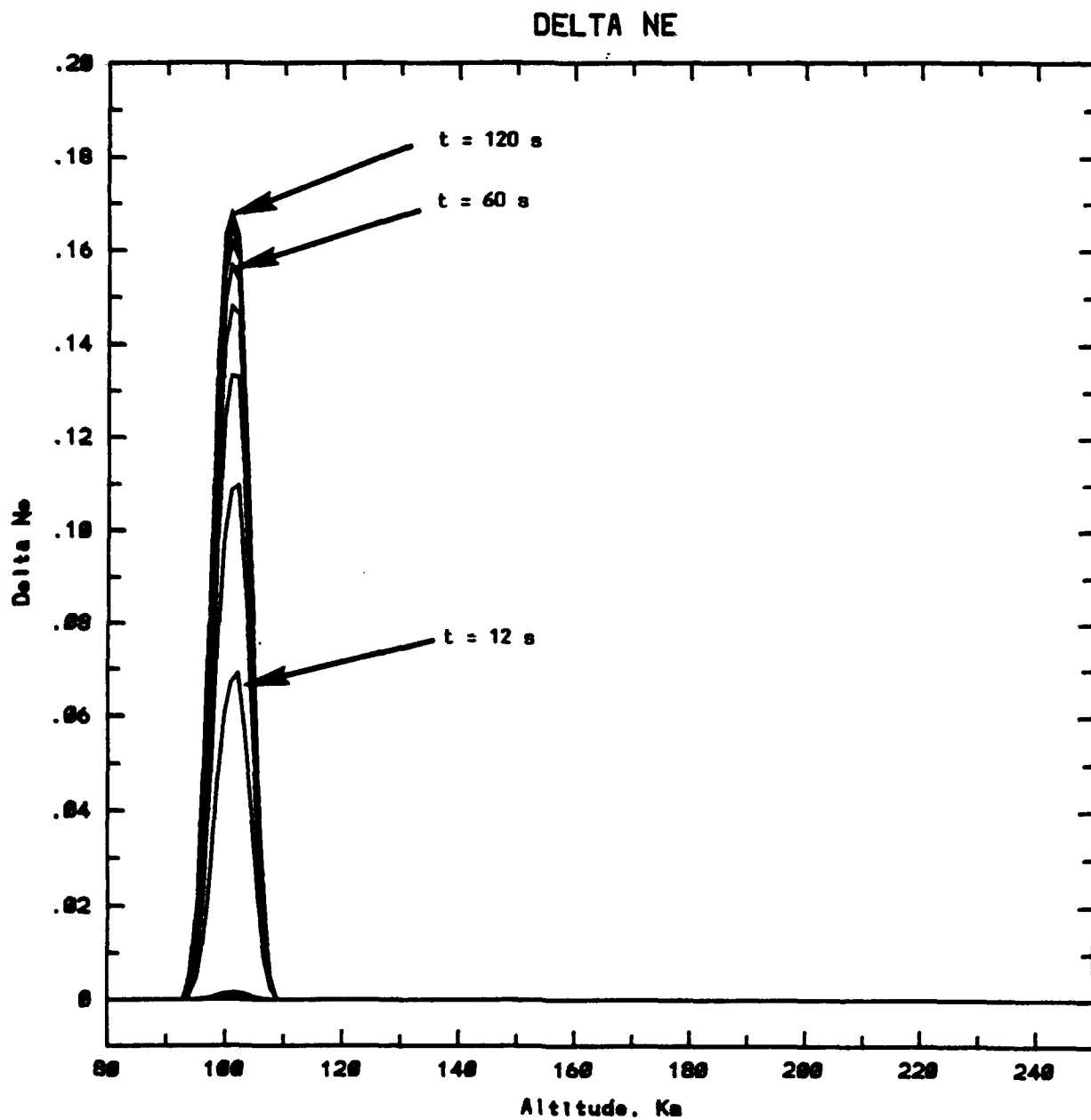


Figure 8-16b. Normalized Electron Density Modification vs. Altitude for Case 0112



**Figure 8-16c. Normalized Electron Density Modification vs.
Time Near Peak of Q_{hr} Profile for Case 0112**

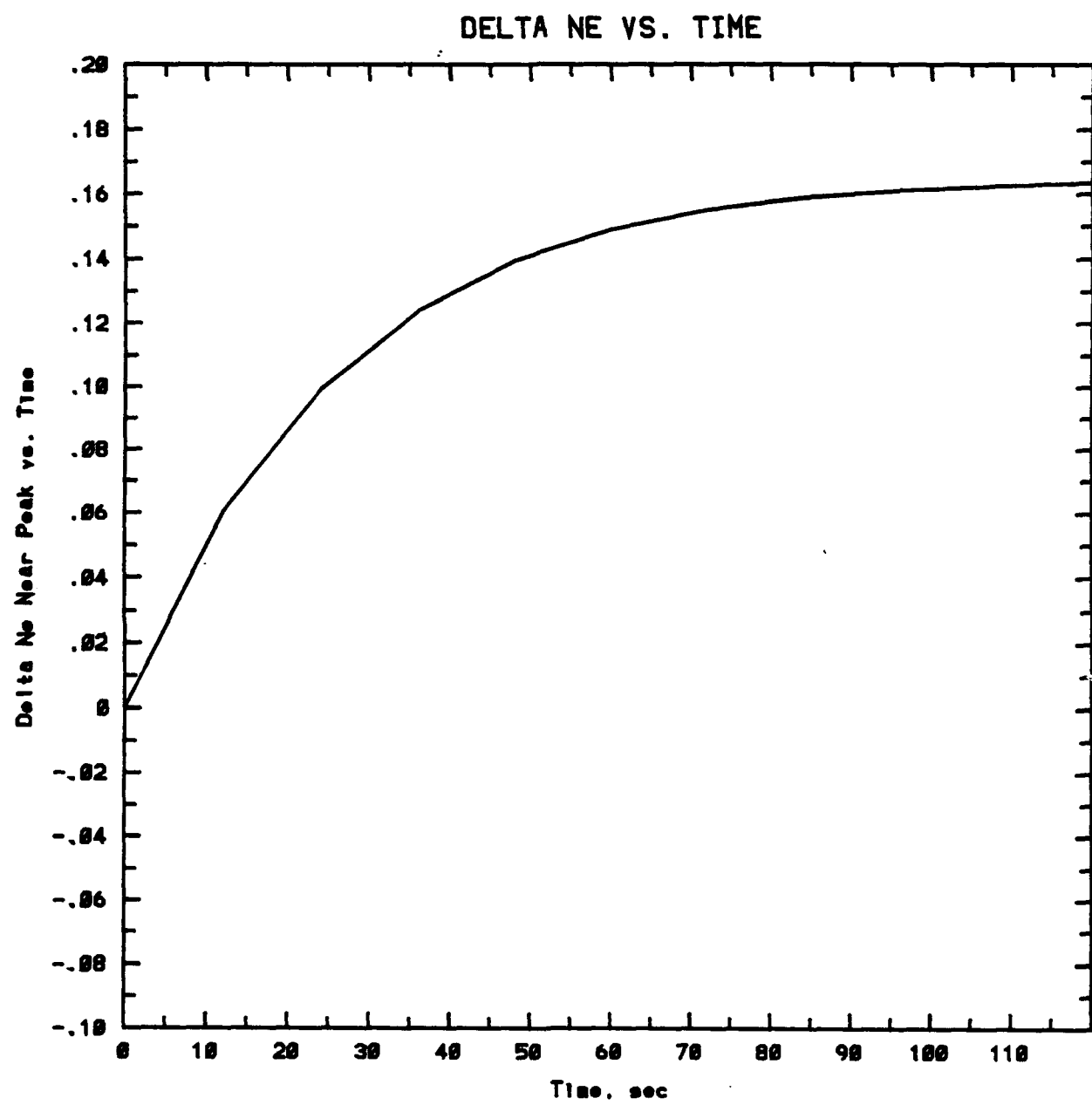
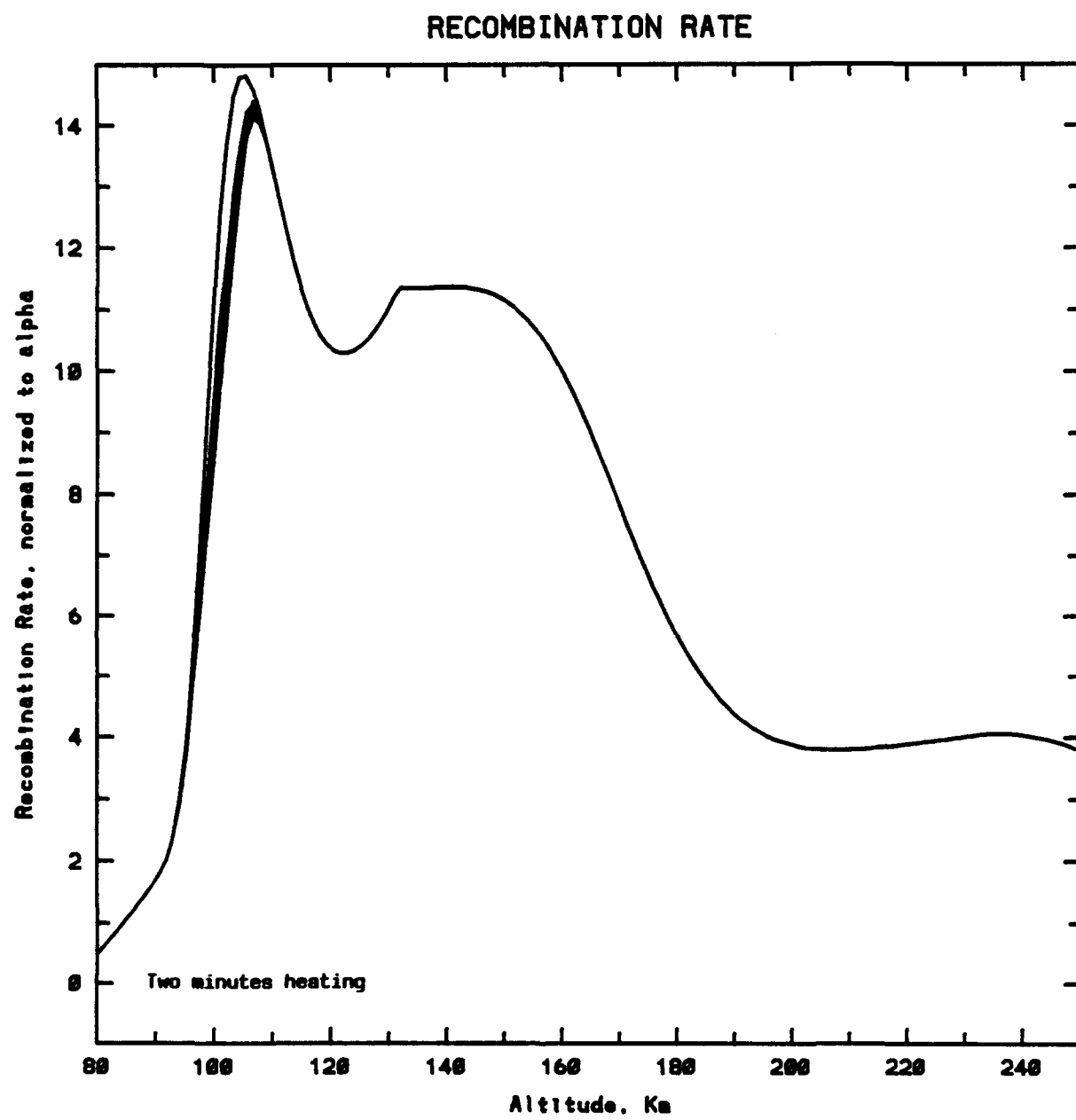
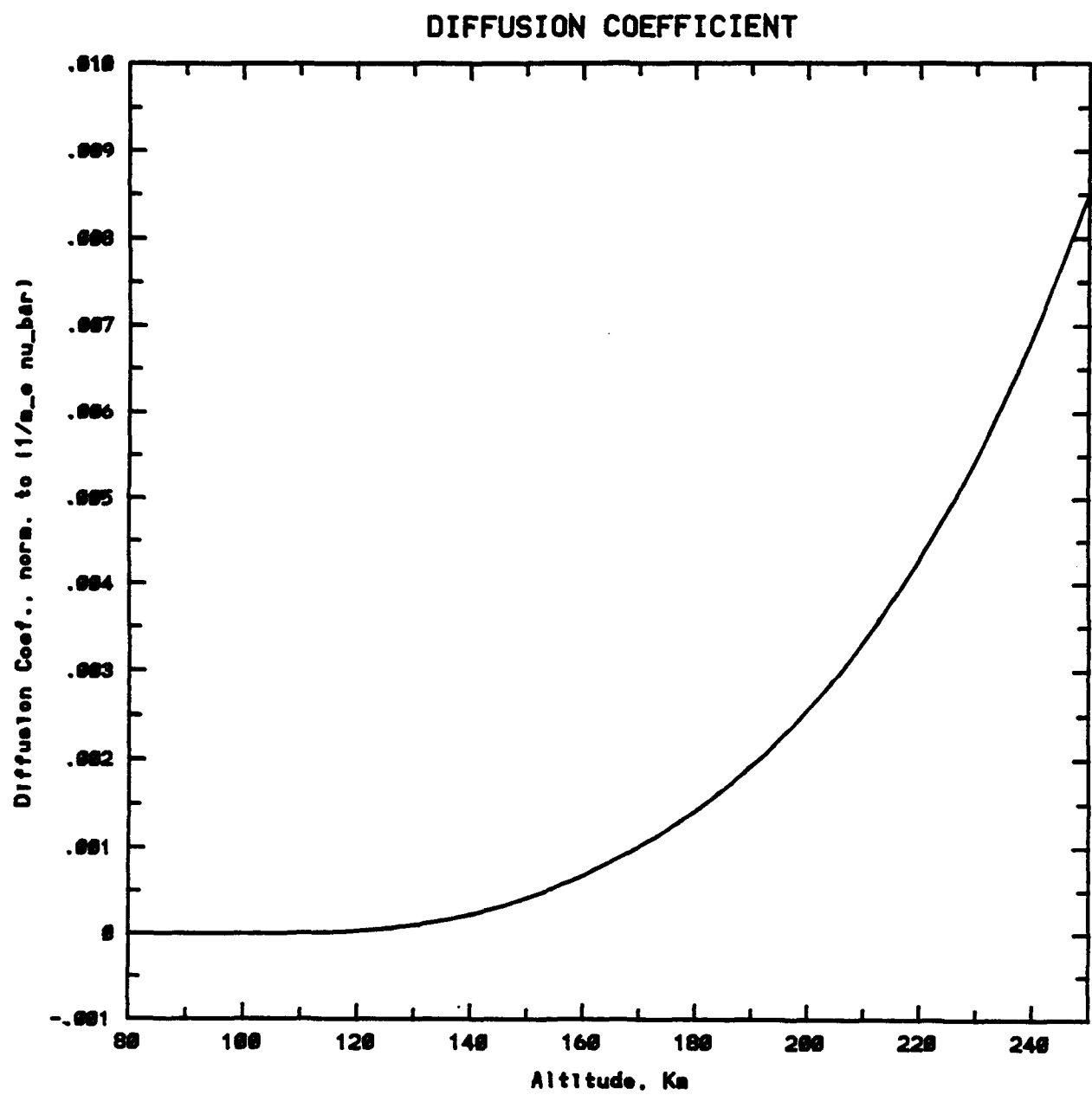


Figure 8-17. Recombination Rate vs. Altitude for Case 0112



**Figure 8-18. Normalized Diffusion Coefficient vs. Altitude
for Case 0112**



**Figure 8-19. Normalized Thermal Conductivity vs. Altitude
for Case 0704 at 6 Second Intervals During Heating**

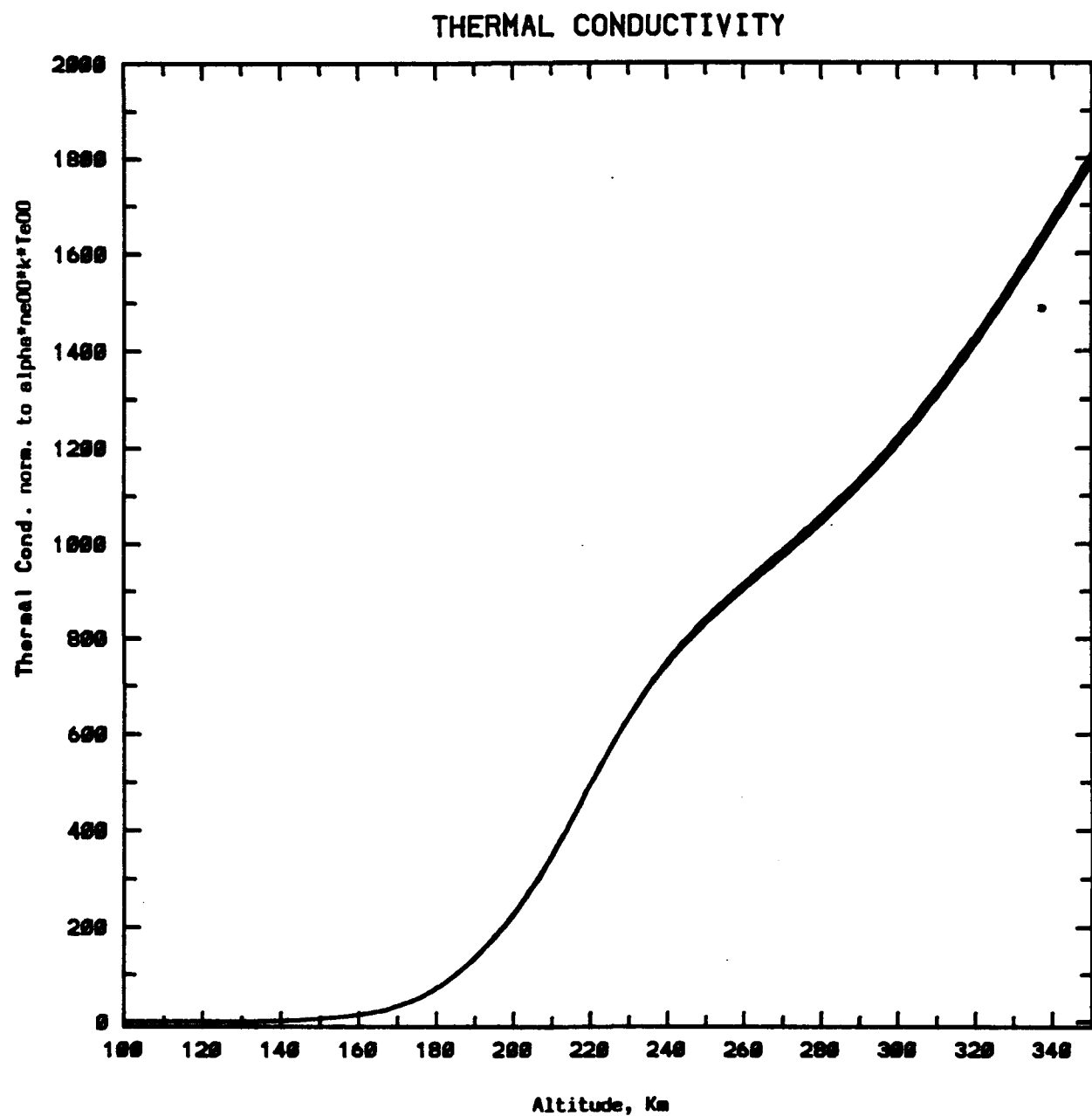


Figure 8-20a. Electron Temperature vs. Altitude for Case 0704 at 6 Second Intervals During Heating

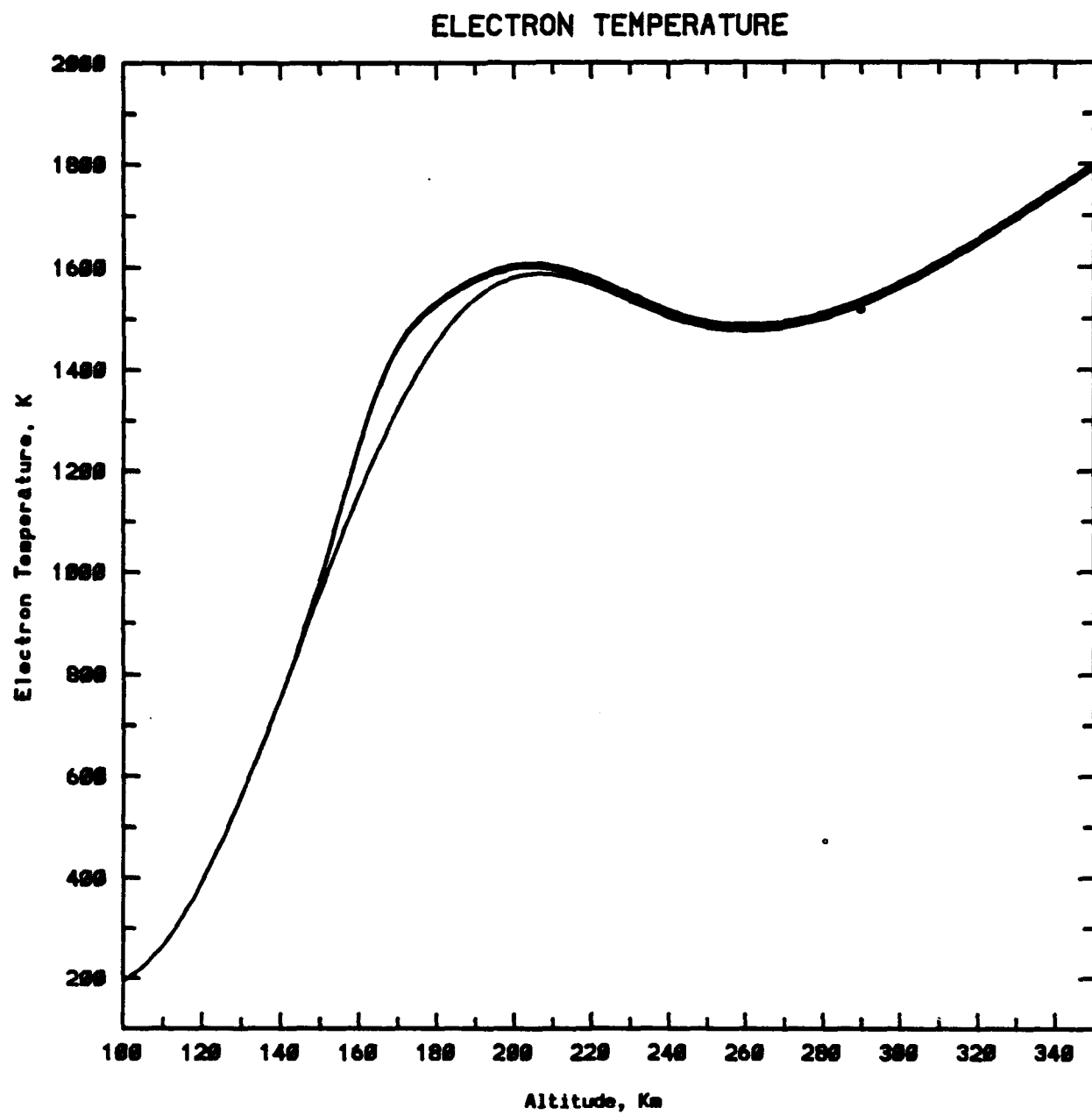
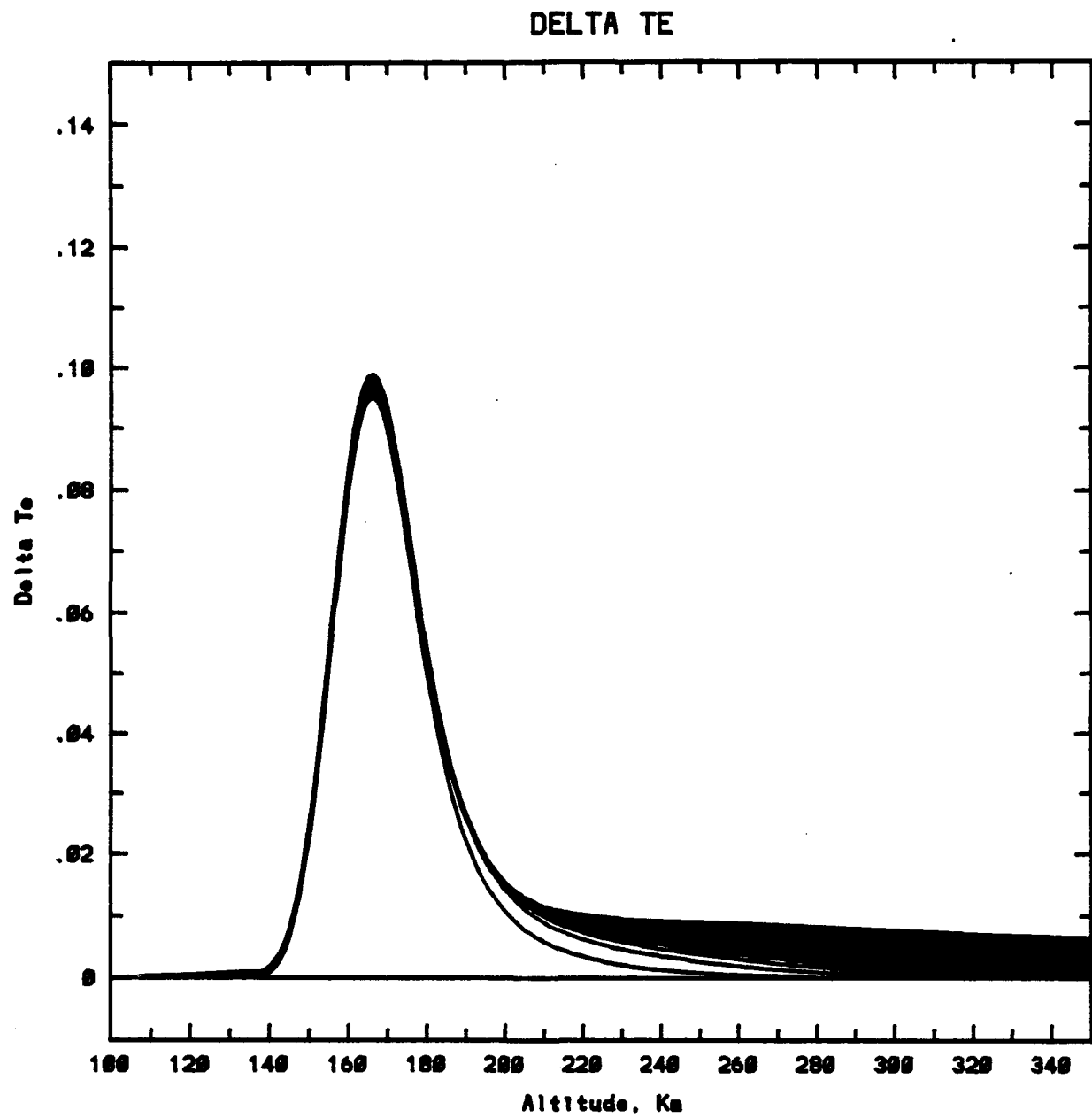
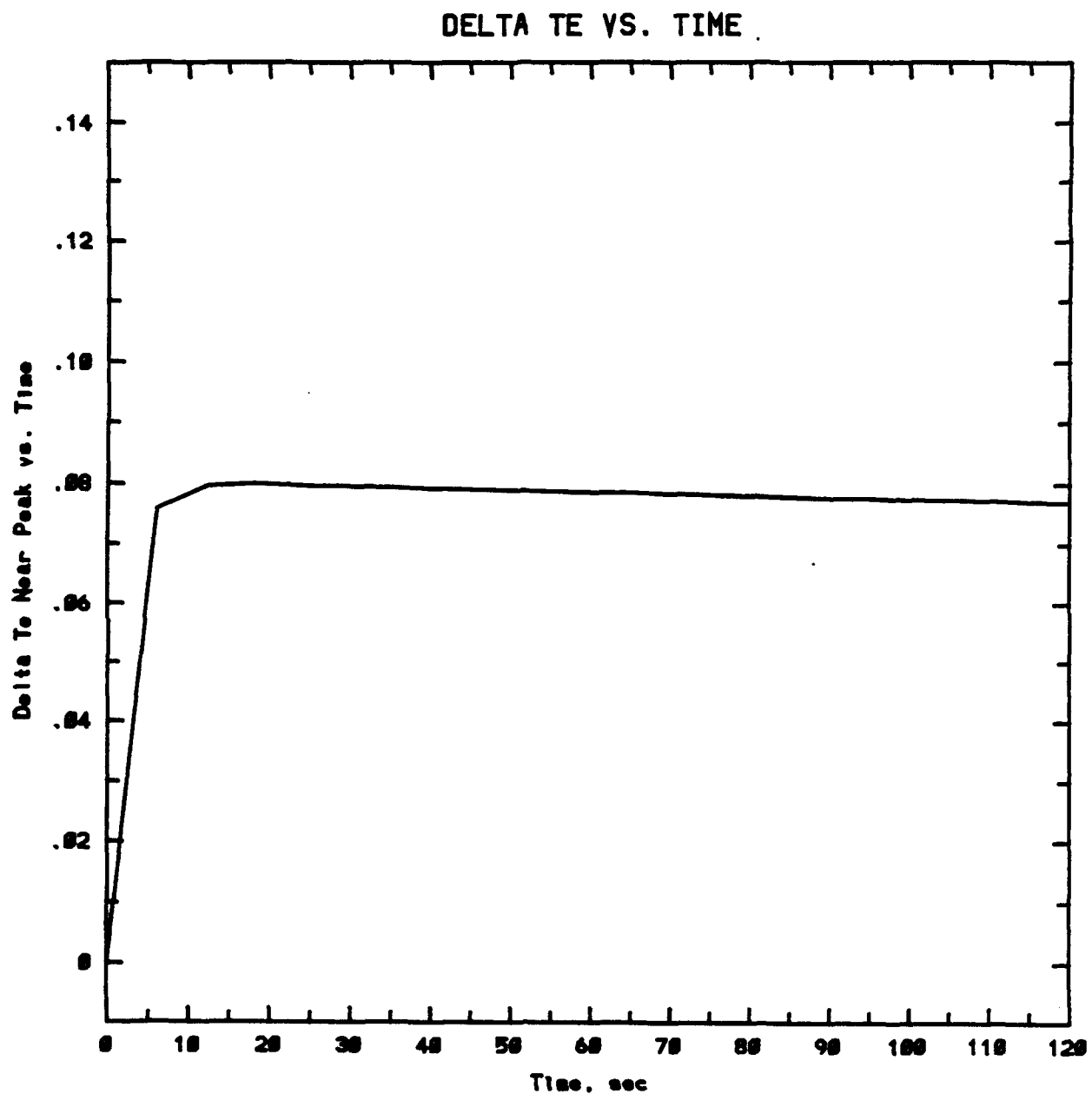


Figure 8-20b. Normalized Electron Temperature Modification vs. Altitude for Case 0704 at 6 Second Intervals During Heating



**Figure 8-20c. Normalized Electron Temperature Modification
vs. Time Near Peak of Q_{in} Profile for Case 07U4**



**Figure 8-21. Electron Cooling vs. Altitude for Case 0704
at 6 Second Intervals During Heating**

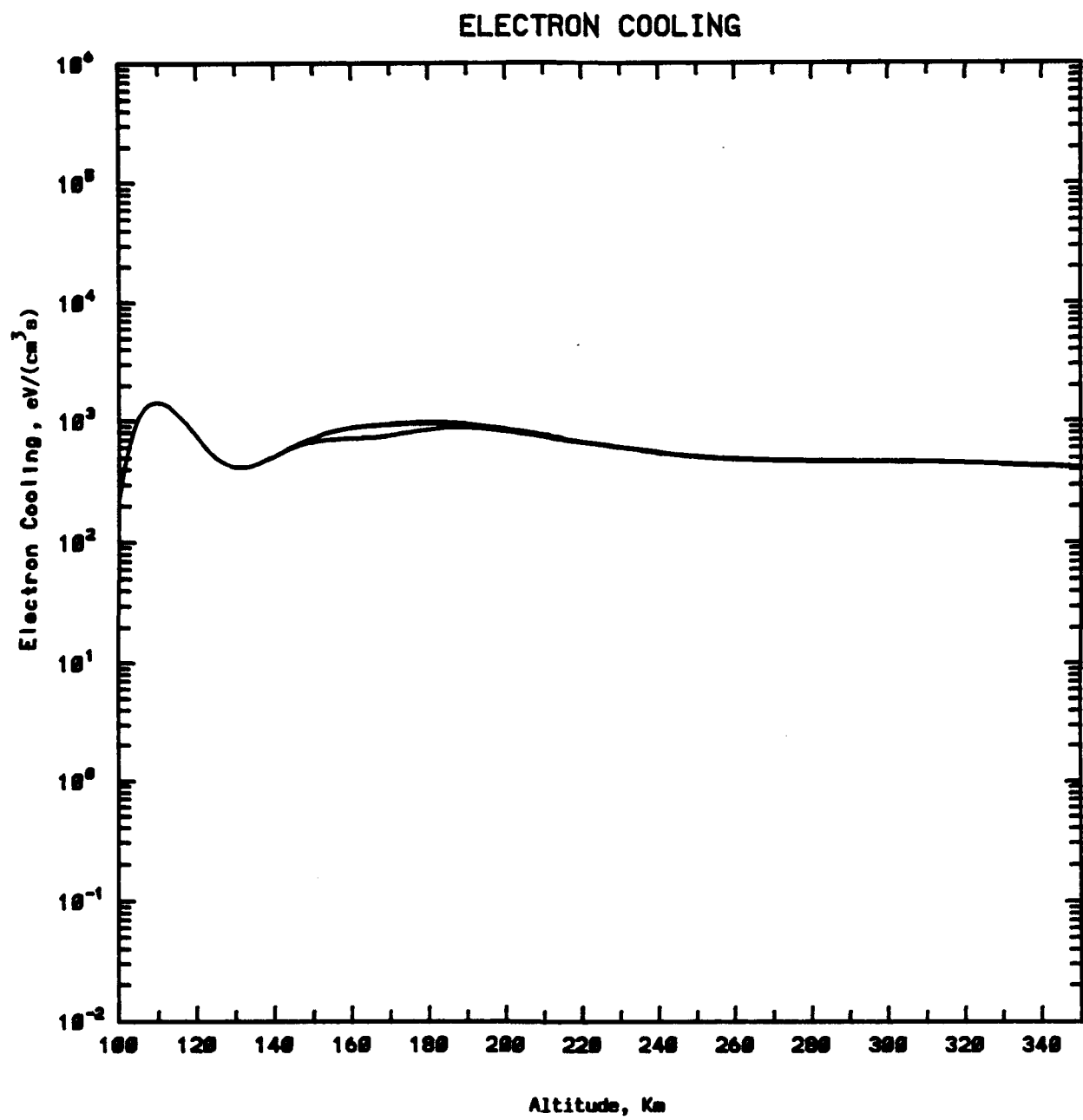


**Figure 8-22. Electron Collision Frequency vs. Altitude
for Case 0704 at 6 Second Intervals During Heating**

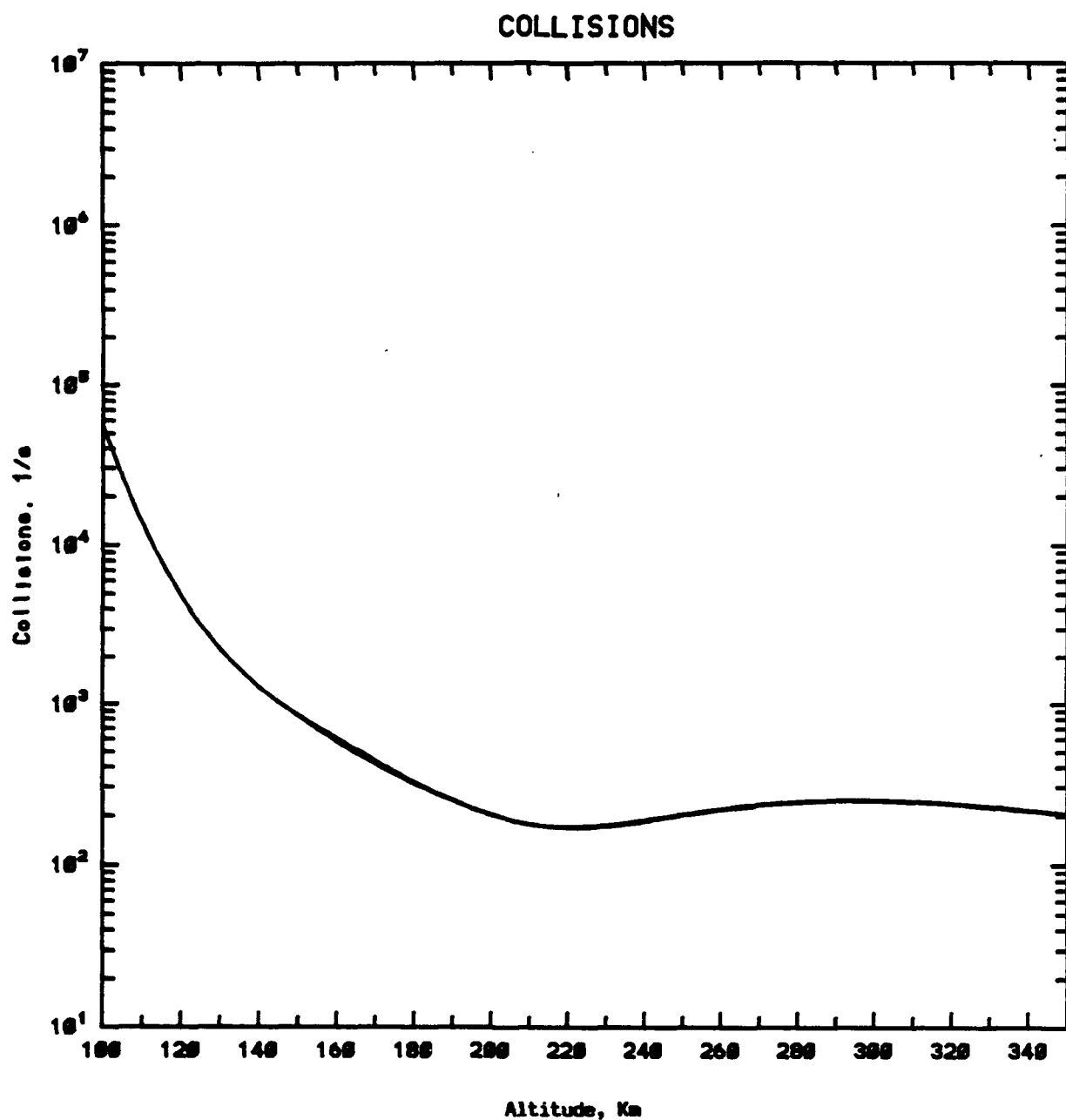


**Figure 8-23a. Electron Density vs. Altitude for Case 0704
at 6 Second Intervals During Heating**

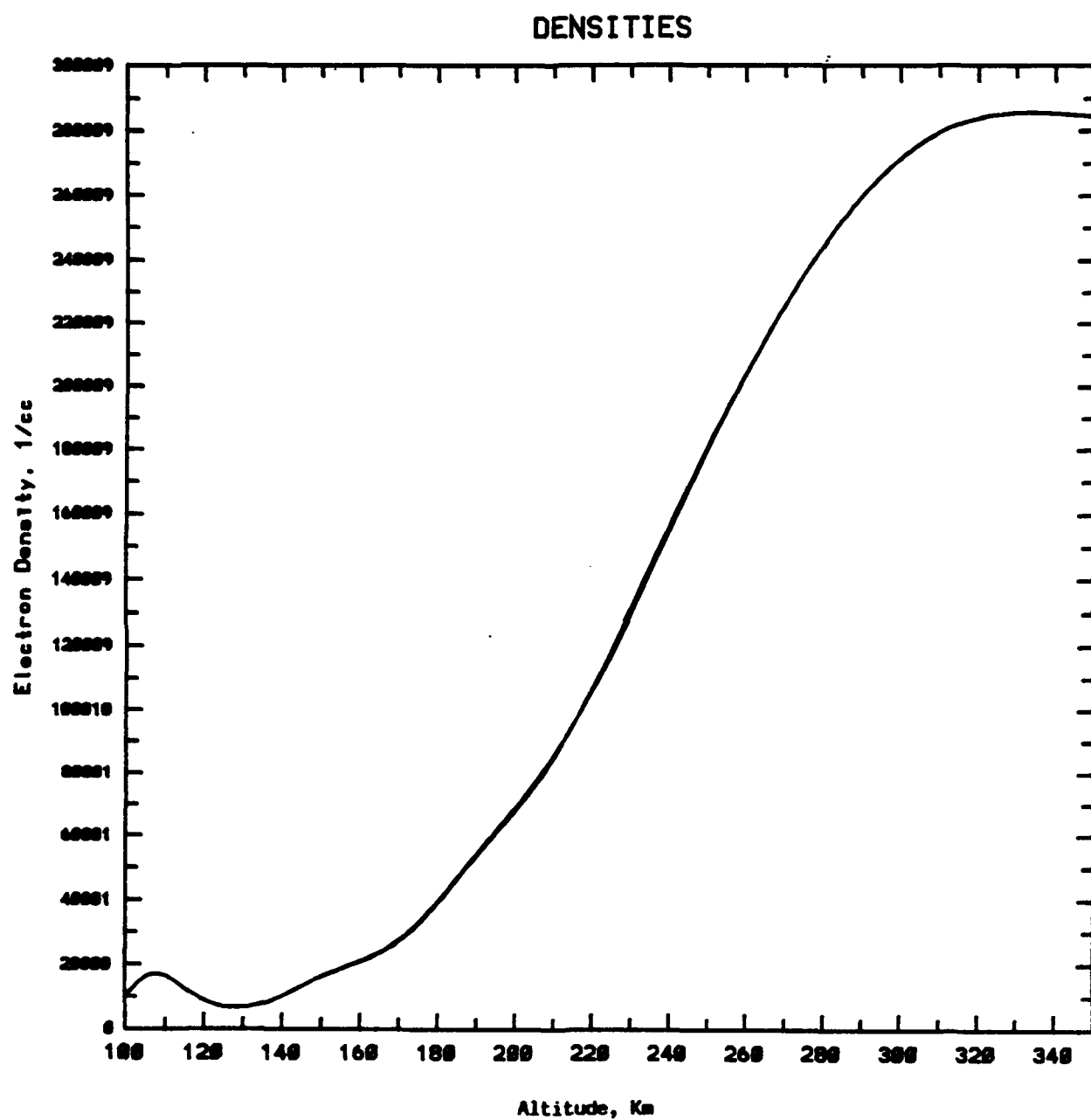


**Figure 8-23b. Normalized Electron Density Modification
vs. Altitude for Case 0704 at 6 Second Intervals
During Heating**

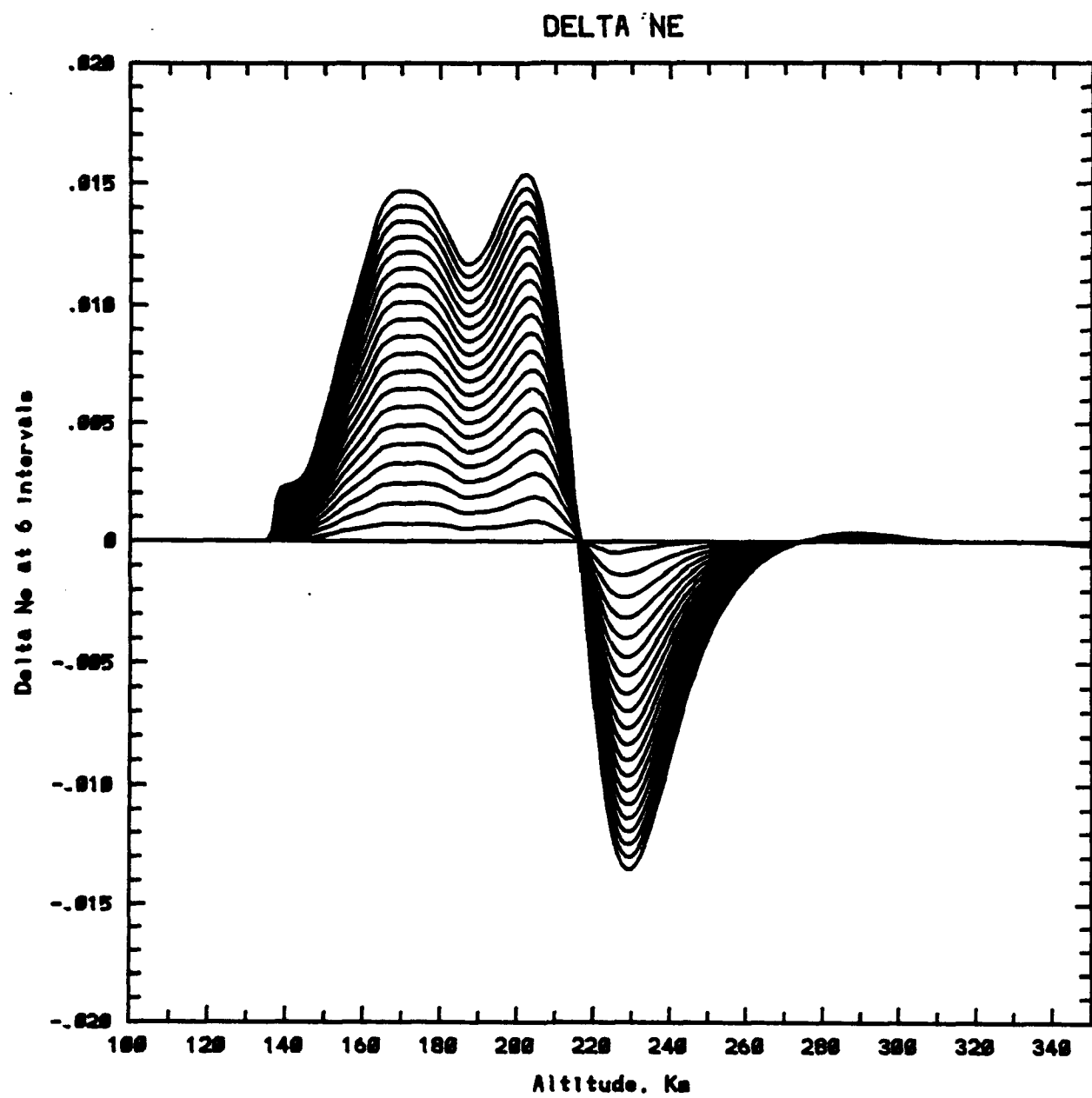


**Figure 8-23c. Normalized Electron Density Modification
vs. Time Near Peak of Q_{hf} Profile for Case 0704**

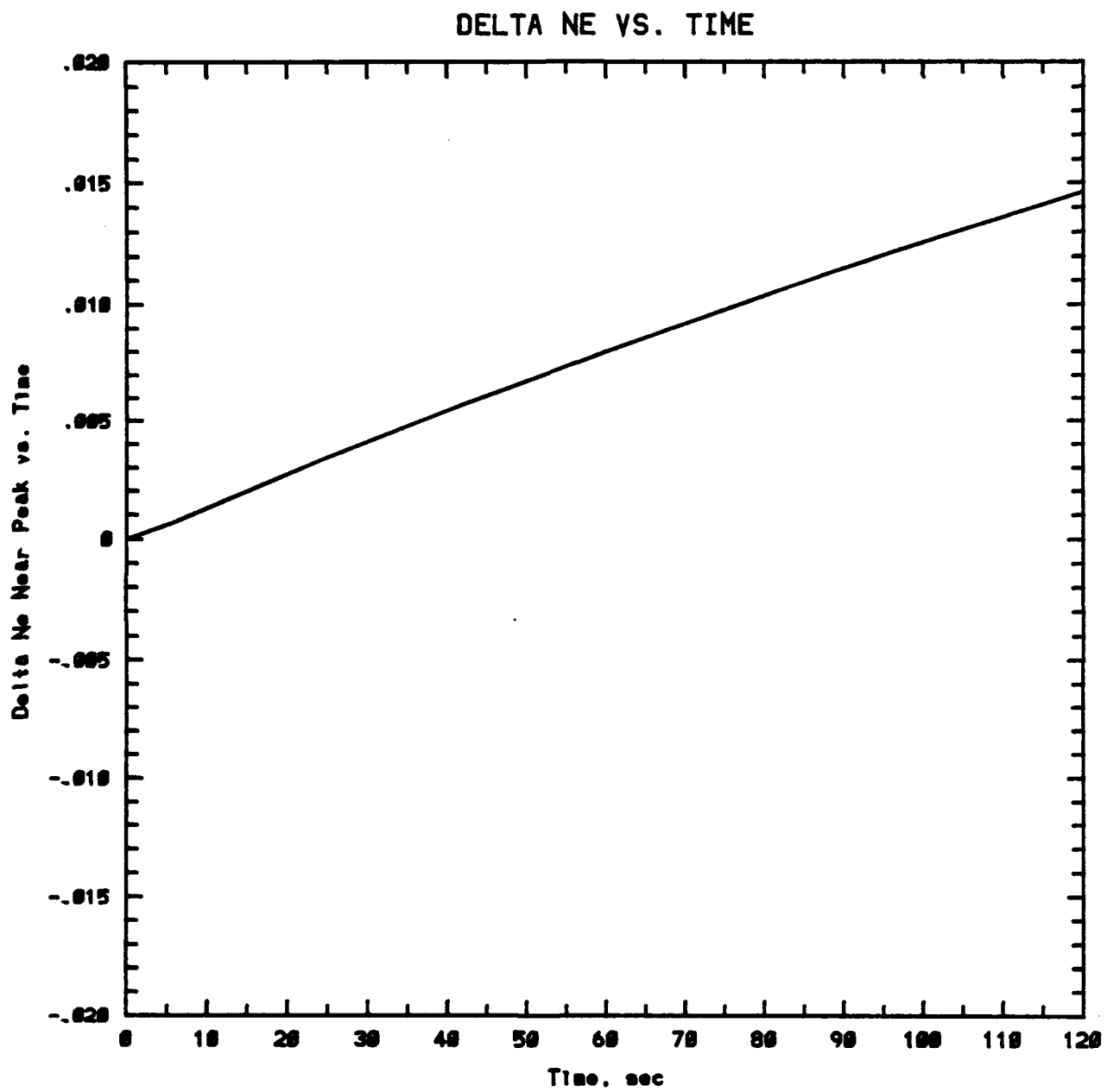


**Figure 8-24. Recombination Rate vs. Altitude for Case 0704
at 6 Second Intervals During Heating**

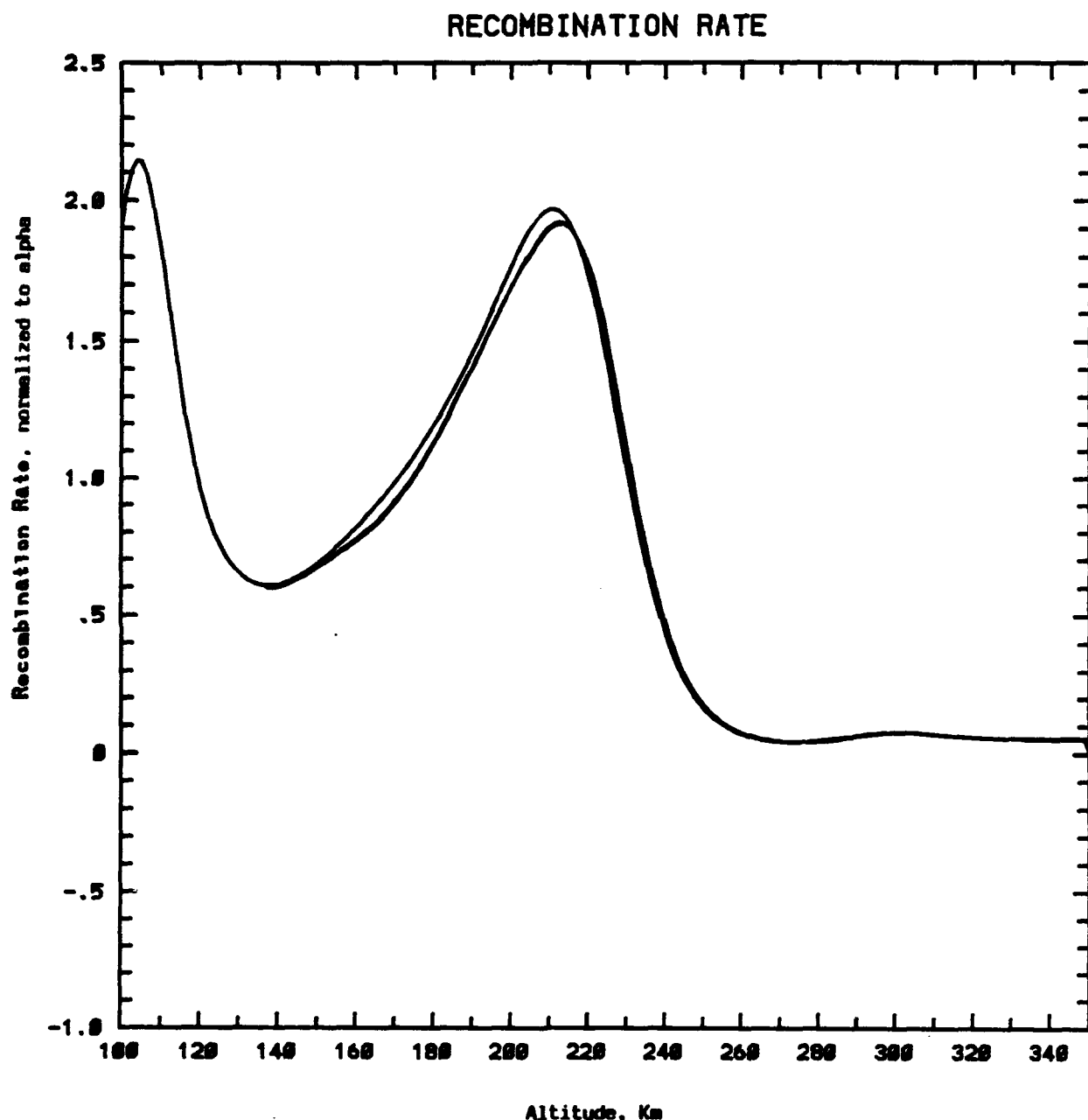


**Figure 8-25. Normalized Diffusion Coefficient vs. Altitude
for Case 0704 at 6 Second Intervals During Heating**

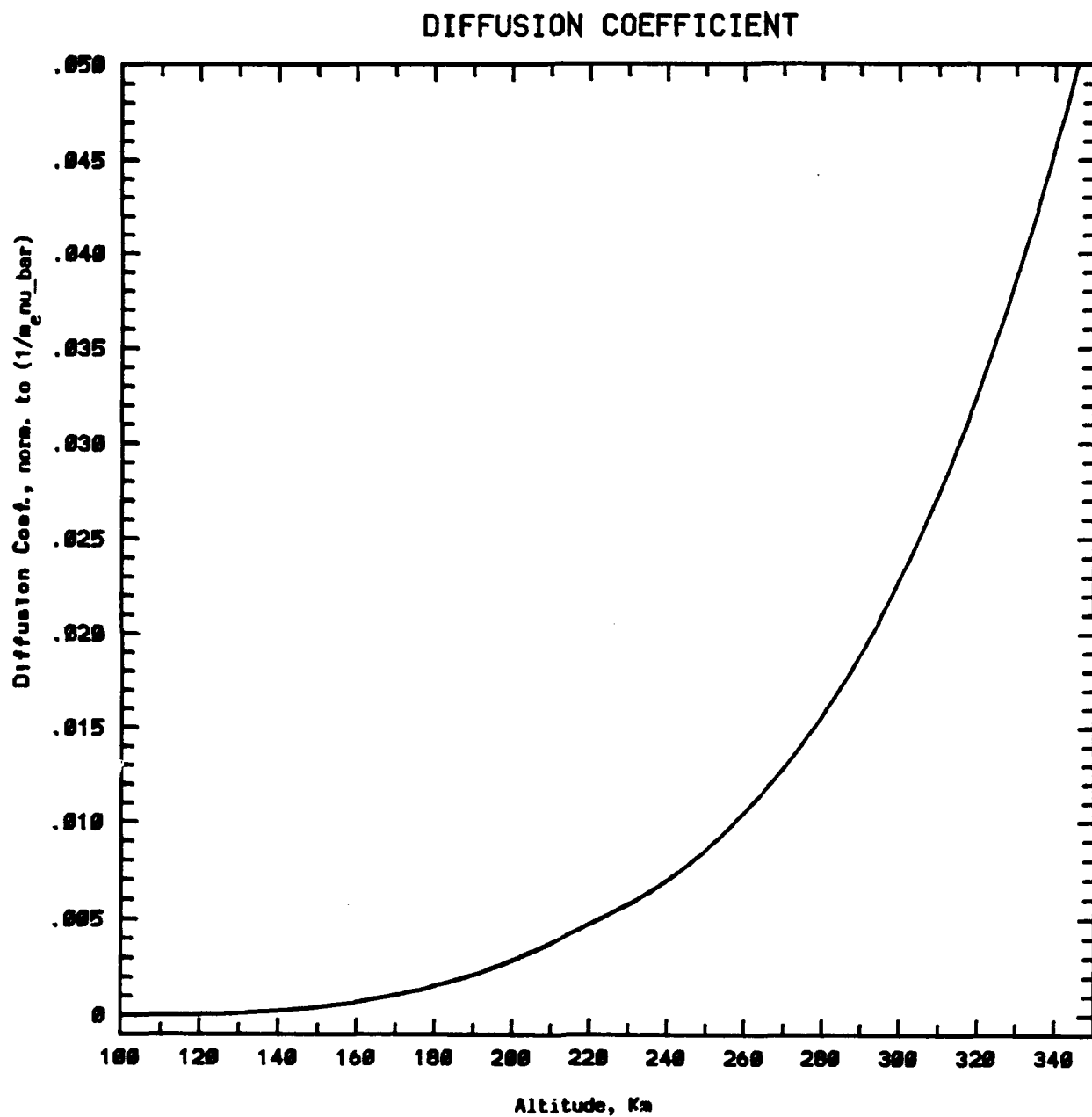


Figure 8-26. Normalized Electron Temperature Modification vs. Altitude for Case 0112 at 6 Second Intervals During Heating When Recombination Rate Is Constant in Time

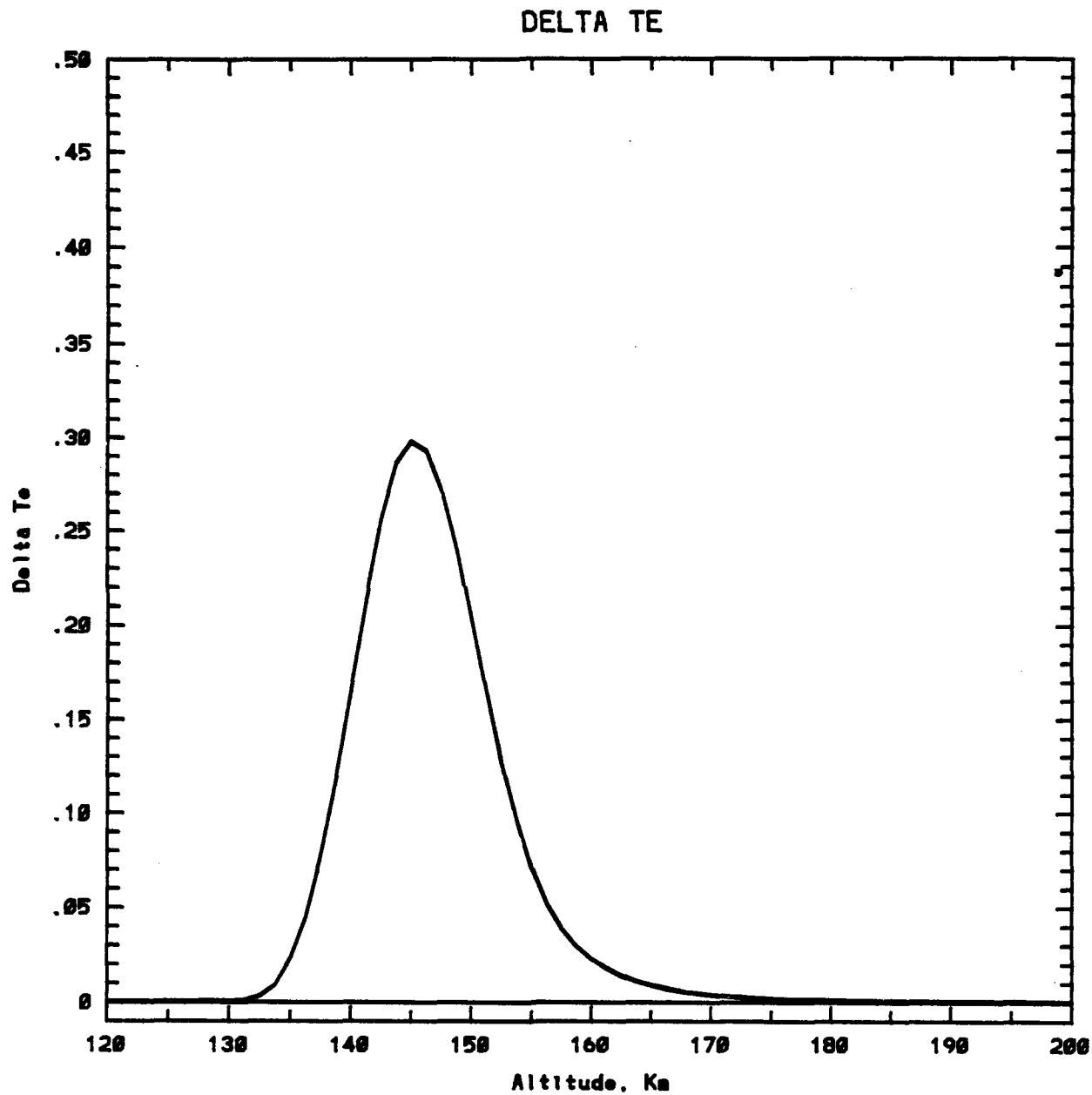
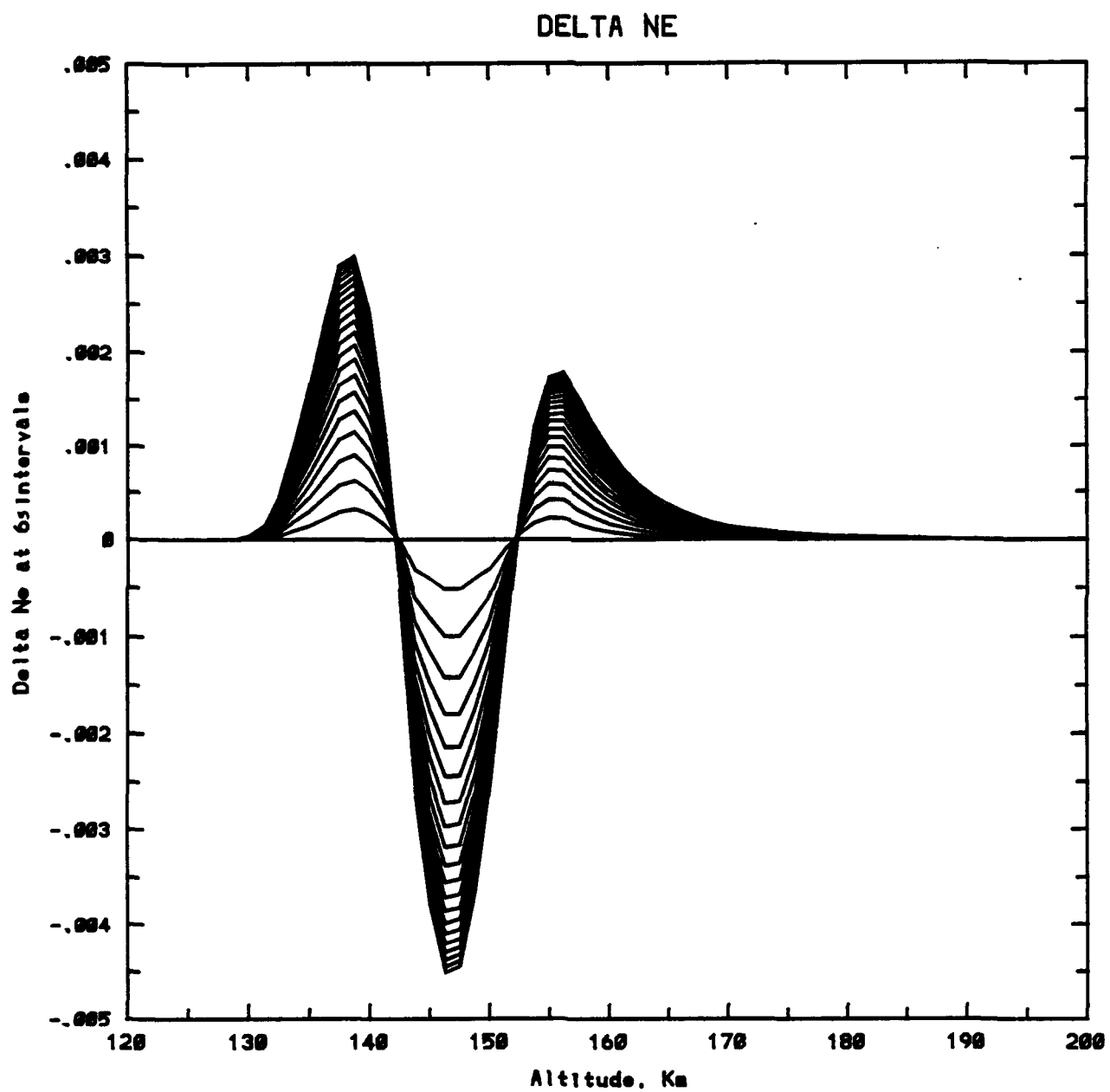
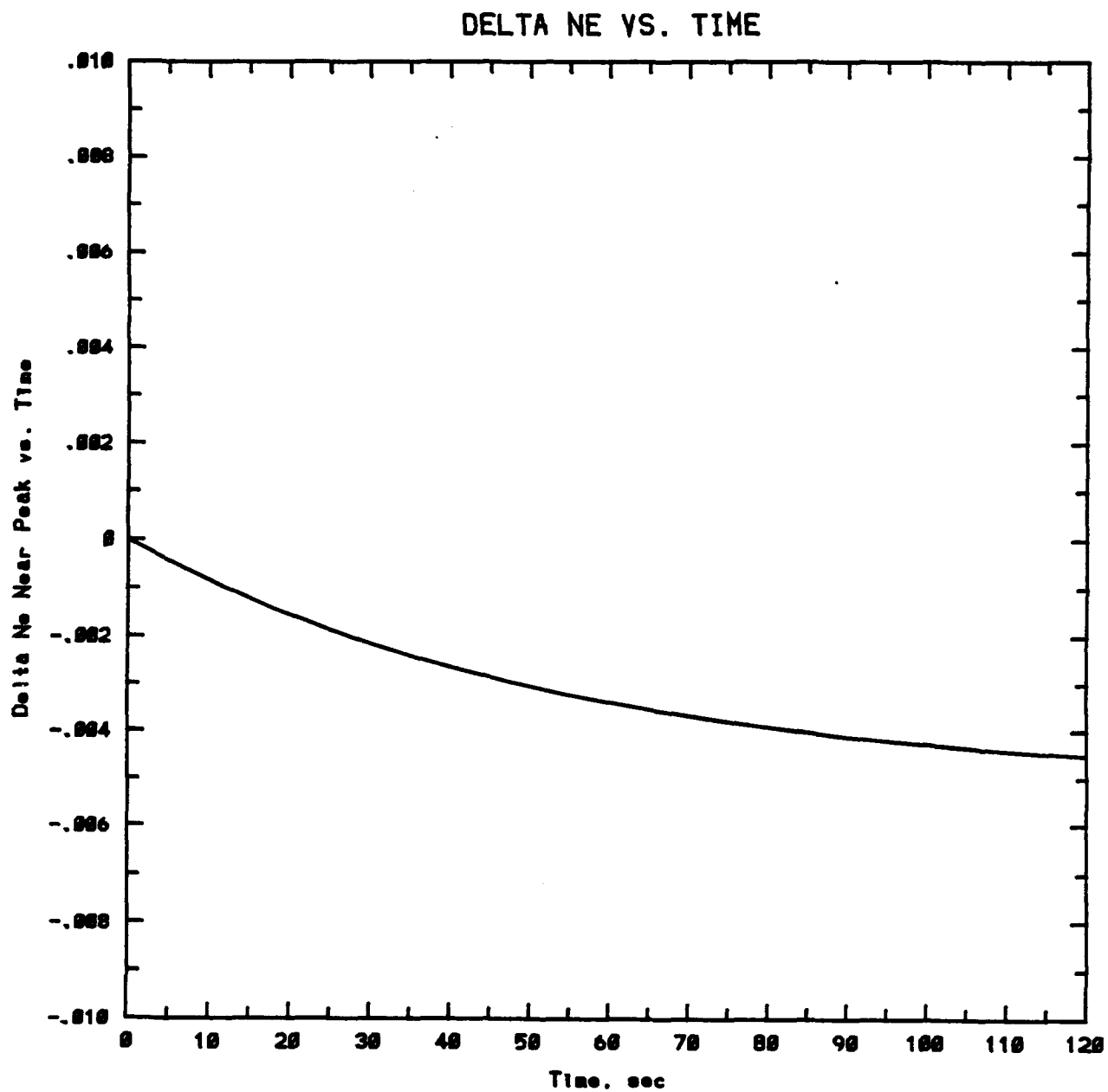


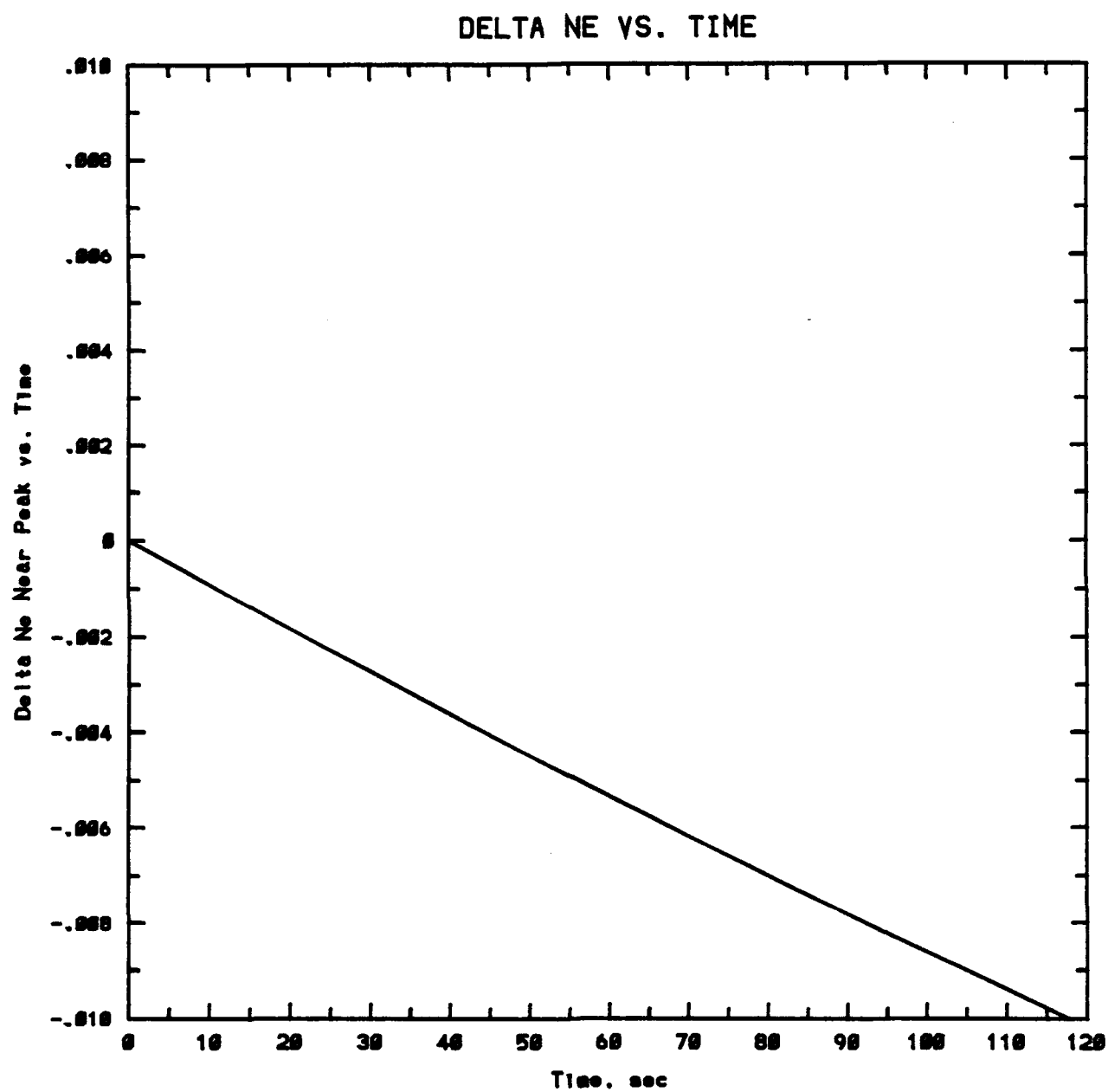
Figure 8-27. Normalized Electron Density Modification vs. Altitude for Case 0112 at 6 Second Intervals During Heating When Recombination Rate Is Constant in Time



**Figure 8-28. Normalized Electron Density Modification
vs. Time Near Peak of Q_{hy} Profile
for Case 0112 When Recombination Rate Is Constant in Time**



**Figure 8-29. Normalized Electron Density Modification
vs. Time Near Peak of Q_{hr} Profile
for Case 0112 When Recombination Rate Is Zero**



9. FEEDBACK OF IONOSPHERIC MODIFICATION TO THE RAY TRACING CODE

The transport code writes to an output file, "eos_oth.ou", the number of grid points along a field line, and the size of the grid point spacing; the number of field lines in a meridian plane; the number of meridian planes on which the modifications in density and temperature were calculated; the changes in temperature, $\Delta T_e = T_e(s, t) - T_e(s, t = 0)$; the changes in density, $\Delta n_e = n_e(s, t) - n_e(s, t = 0)$; the beginning point of each field line, s_0 ; and the end point of each field line, s_f . The grid point spacing and the number of grid points on each field line are identical, as is the number of field lines in each meridian plane.

The ray tracing code utilizes this information in the following manner. At each point along a geometric optics ray, an evaluation is performed to determine if that point lies within the box of modification specified by the points \underline{r}_1 , \underline{r}_2 , \underline{r}_3 , and \underline{r}_4 , which were explained in Section 8. If the point is outside the box of modification, then the ray tracing code proceeds as usual. If the point lies within the box of modification, then it is necessary to find the value of ΔT_e , Δn_e , the first derivatives of Δn_e , and the second derivatives of Δn_e at that point. A numerical interpolation scheme is implemented to find these quantities. The value of ΔT_e is used to update the collision frequency, and the value of Δn_e , as well as its derivatives, is used to update the dielectric tensor.

The interpolation is performed in the magnetic field frame of reference. Since a scalar quantity does not depend upon the reference frame, the values of ΔT_e and Δn_e are the same in the launch point frame and the magnetic field frame. However, the derivatives of Δn_e must be transformed to the launch point frame, and in that frame they are given by the expressions

$$(\nabla n)_{l.p. \text{ frame}} = \underline{R} \cdot (\nabla n)_{\bar{B} \text{ frame}} \quad (1)$$

$$(\nabla \nabla n)_{l.p. \text{ frame}} = \underline{R}^{-1} \cdot (\nabla \nabla n)_{\bar{B} \text{ frame}} \cdot \underline{R} \quad (2)$$

Once these values are determined and the dielectric tensor is updated, the ray tracing calculation proceeds as before.

9-1. Daytime Heating - Case 0112

It is worthwhile to examine the contour plots of Δn_e and its derivatives in the y-z plane of the launch point reference frame, which is nearly perpendicular to the HF beam. Figures 9-1a-d exhibit the behavior of these quantities in the box of modification.

The contours of Δn_e are positive, and centered about the HF beam on all meridian planes. The derivatives of Δn_e show the correct topological behavior, namely that they are positive below the center line of the density change, and negative above.

Figures 9-2 depict the paths of the rays after heating has occurred. The introduction of a "blob" of density to the ionosphere acts as a scatterer, and the rays deflect outward both in elevation and azimuthal angles. The point of entry into the ionosphere is clearly observed in Figure 9-2a, after which the ray paths change from their unperturbed form. Figure 9-2c shows a crossing of rays in the x-y plane. The rays above the $y=0$ line are deflected upward, and those below the $y=0$ line are deflected downward.

9-2. Nighttime Heating - Case 0704

Figures 9-3 are contour plots of Δn_e and its derivatives in the y-z plane of the launch point reference frame over the range of the box of modification. At lower altitudes, the density modification is positive definite everywhere. At higher altitudes, the density changes are negative at low z, and positive at high z, as discussed in Section 8.

Figures 9-4 show the ray paths after heating has taken place for the nighttime scenario in the x-z, y-z, and x-y planes, respectively. The ray trajectories in the x-z plane (Figure 9-4a) change very slightly from their unperturbed paths. There is a slight spreading present in the ray paths in both the y-z (Figure 9-4b) and the x-y (Figure 9-4c) planes. The reason that there is very little change in the paths of the rays is because the alterations in density and temperature which occurred are very small.

9-3. Iterative Self-Consistent Coupling

While this analysis only goes through one iteration, all of the tools required to perform an iterative self-consistent calculation have been developed. The procedure outlined in this report must be iterated until convergence in the ray paths is achieved. If convergence cannot be attained, then the duration time of ionospheric heating ($\Delta t_{\text{heating}}$) before feedback is performed needs to be shortened until convergence occurs.

**Figure 9-1a. Electron Density Modification Contours
in Y-Z Plane for Case 0112**

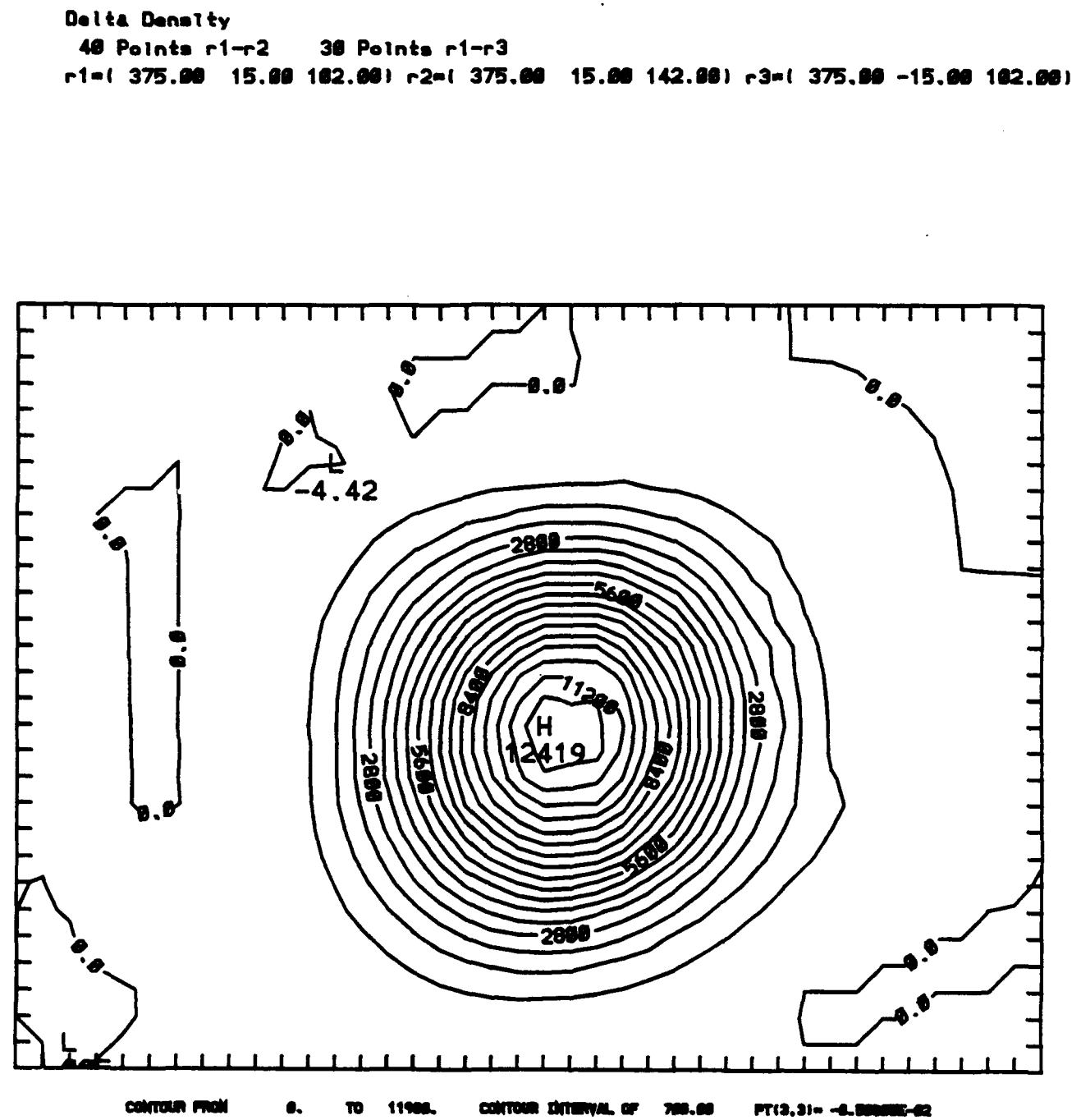
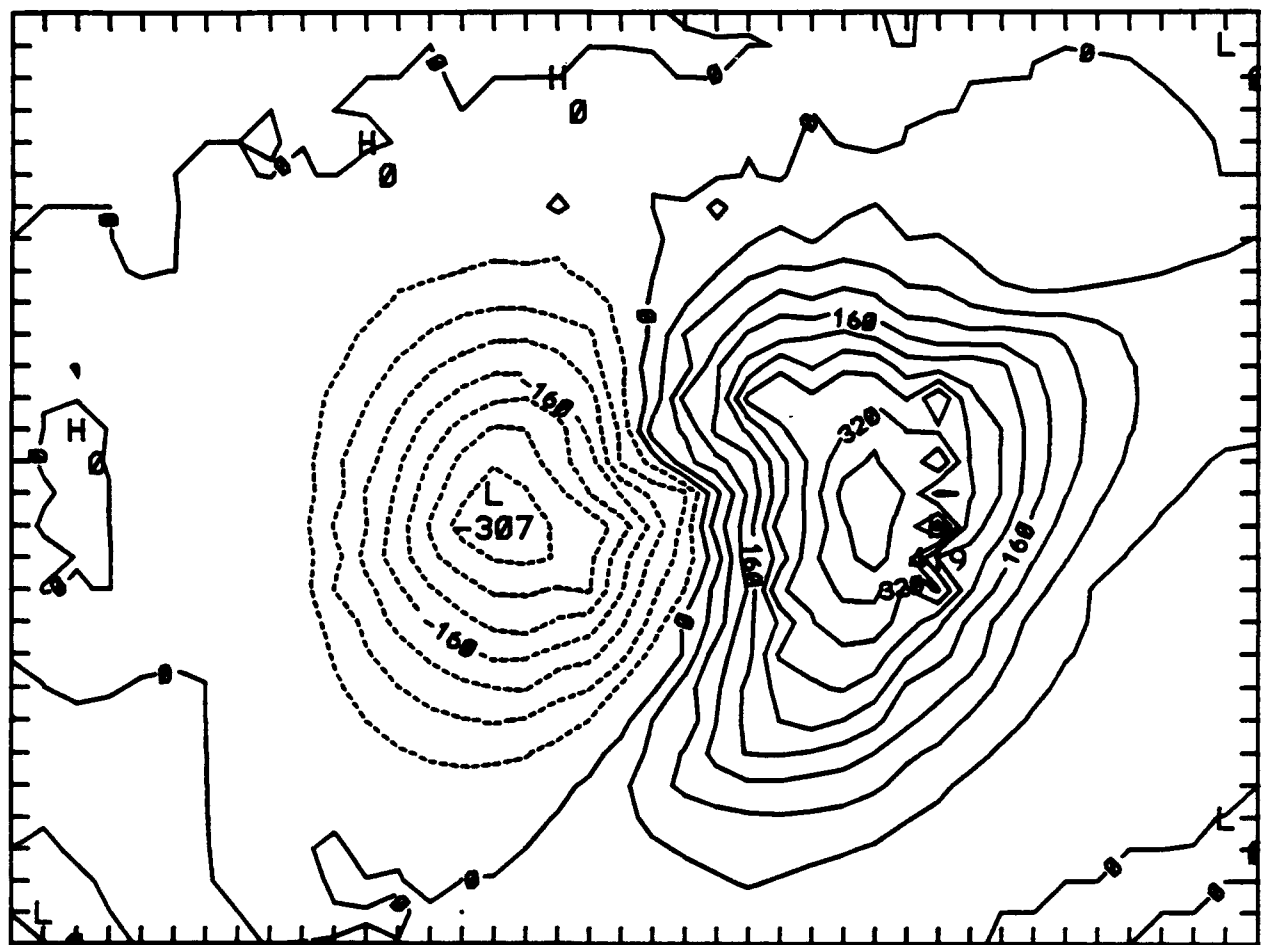


Figure 9-1b. Contours of X-Derivative of Electron Density Modification in Y-Z Plane for Case 0112

Delta Density grad x

48 Points r1-r2 30 Points r1-r3

$r1=(375.00 \ 15.00 \ 102.00) \ r2=(375.00 \ 15.00 \ 142.00) \ r3=(375.00 \ -15.00 \ 102.00)$



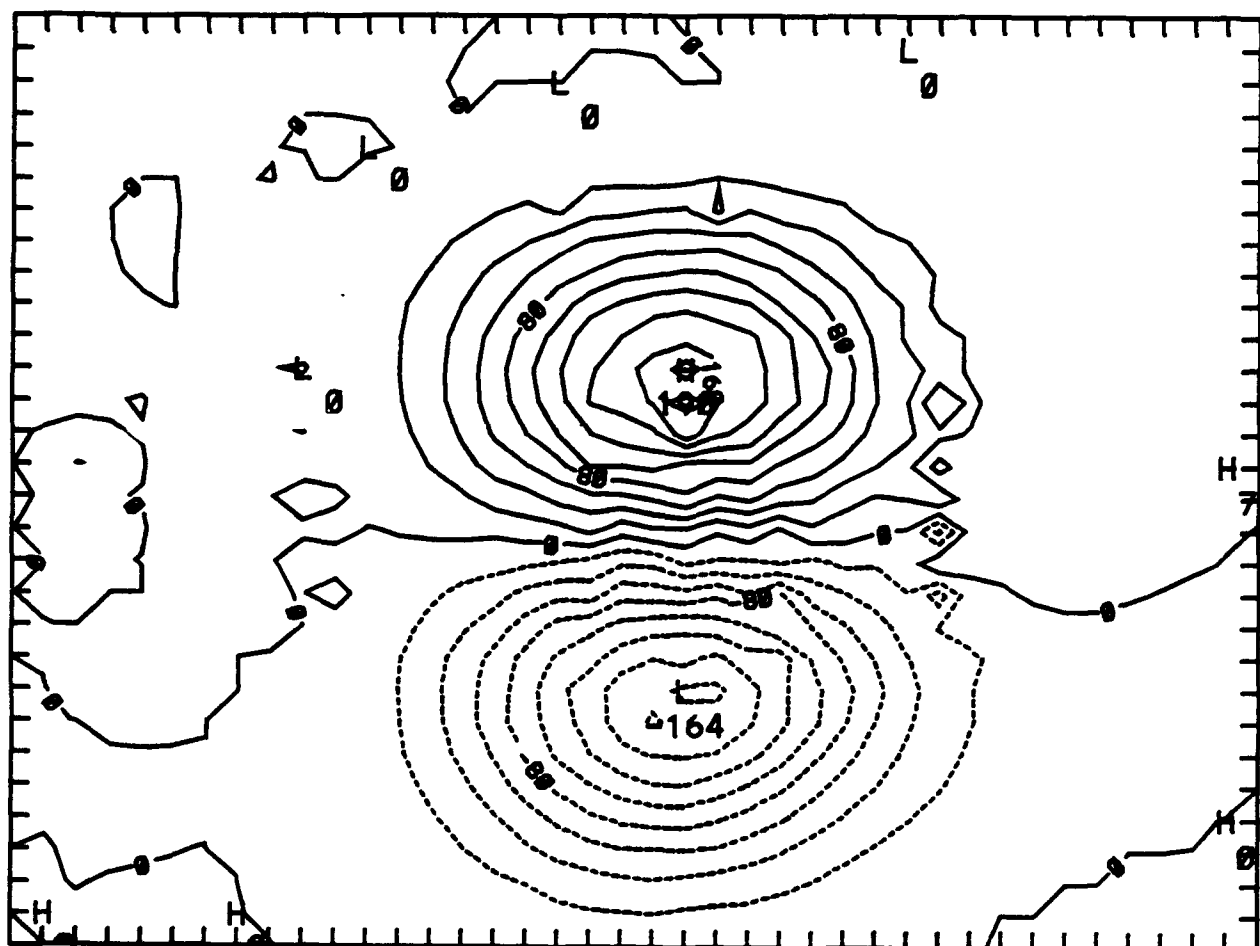
CONTOUR FROM -6.30000E-02 TO 6.40000E-02 CONTOUR INTERVAL OF 8.40000E-03 PT(3,3)= -8.14327E-03 LABELS SCALED BY 8.10000E+04

Figure 9-1c. Contours of Y-Derivative of Electron Density Modification in Y-Z Plane for Case 0112

Delta Density grad y

48 Points r1-r2 38 Points r1-r3

$r1=(375.00 \ 15.00 \ 182.00) \ r2=(375.00 \ 15.00 \ 142.00) \ r3=(375.00 \ -15.00 \ 182.00)$



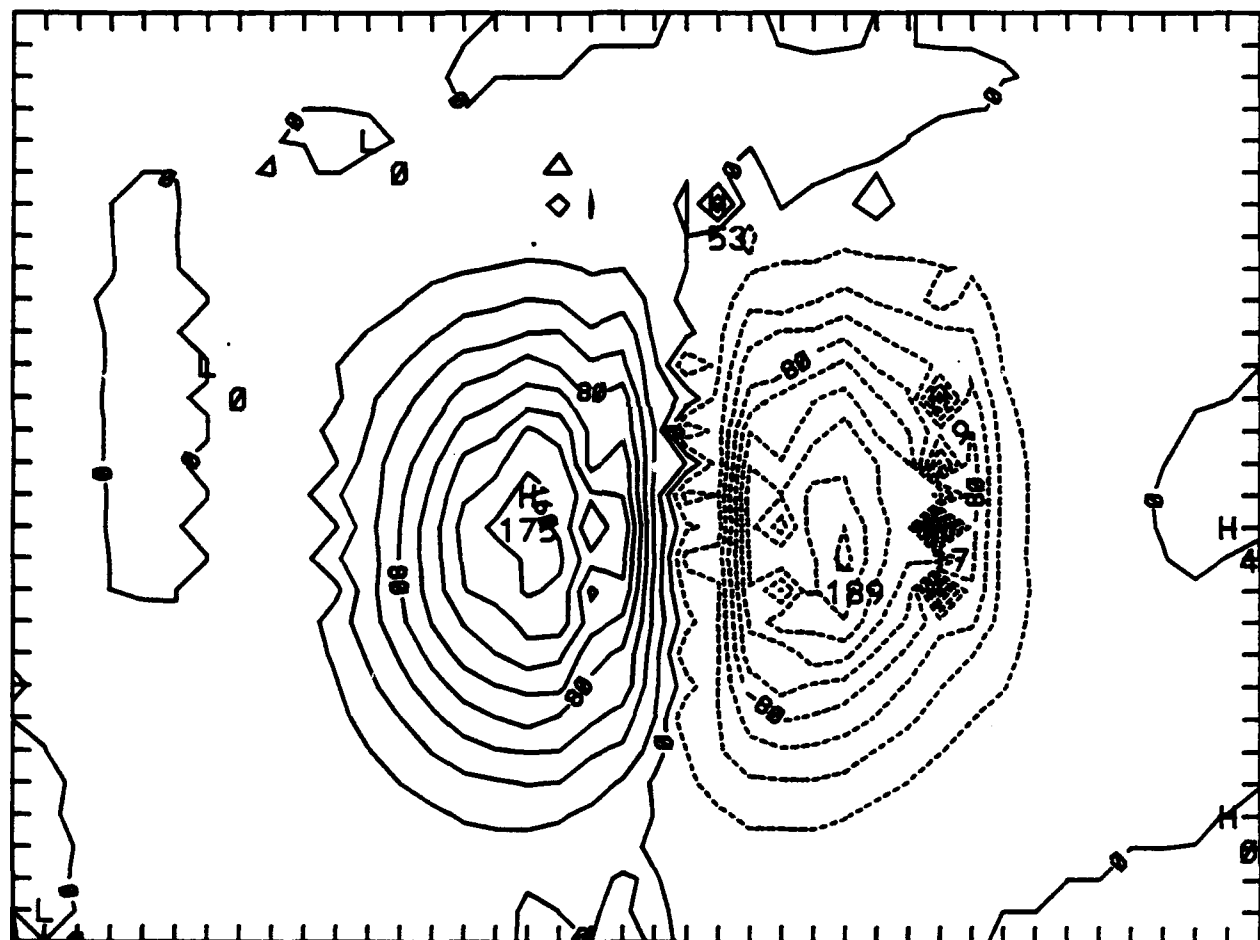
CONTOUR FROM -0.14000E-01 TO 0.10000E-01 CONTOUR INTERVAL OF 0.20000E-02 PT(3,3)= -0.23842E-03 LABELS SCALED BY 10000.

Figure 9-1d. Contours of Z-Derivative of Electron Density Modification in Y-Z Plane for Case 0112

Delta Density grad z

48 Points r1-r2 38 Points r1-r3

$r1=(375.00 \ 15.00 \ 182.00) \ r2=(375.00 \ 15.00 \ 142.00) \ r3=(375.00 \ -15.00 \ 182.00)$



CONTOUR FROM -8.16200E-01 TO 8.16200E-01 CONTOUR INTERVAL OF 8.20000E-02 PT(9,3)= 8.12940E-07 LABELS SCALED BY 10000.

**Figure 9-2a. Ray Paths in the X-Z Plane after Heating
for Case 0112**

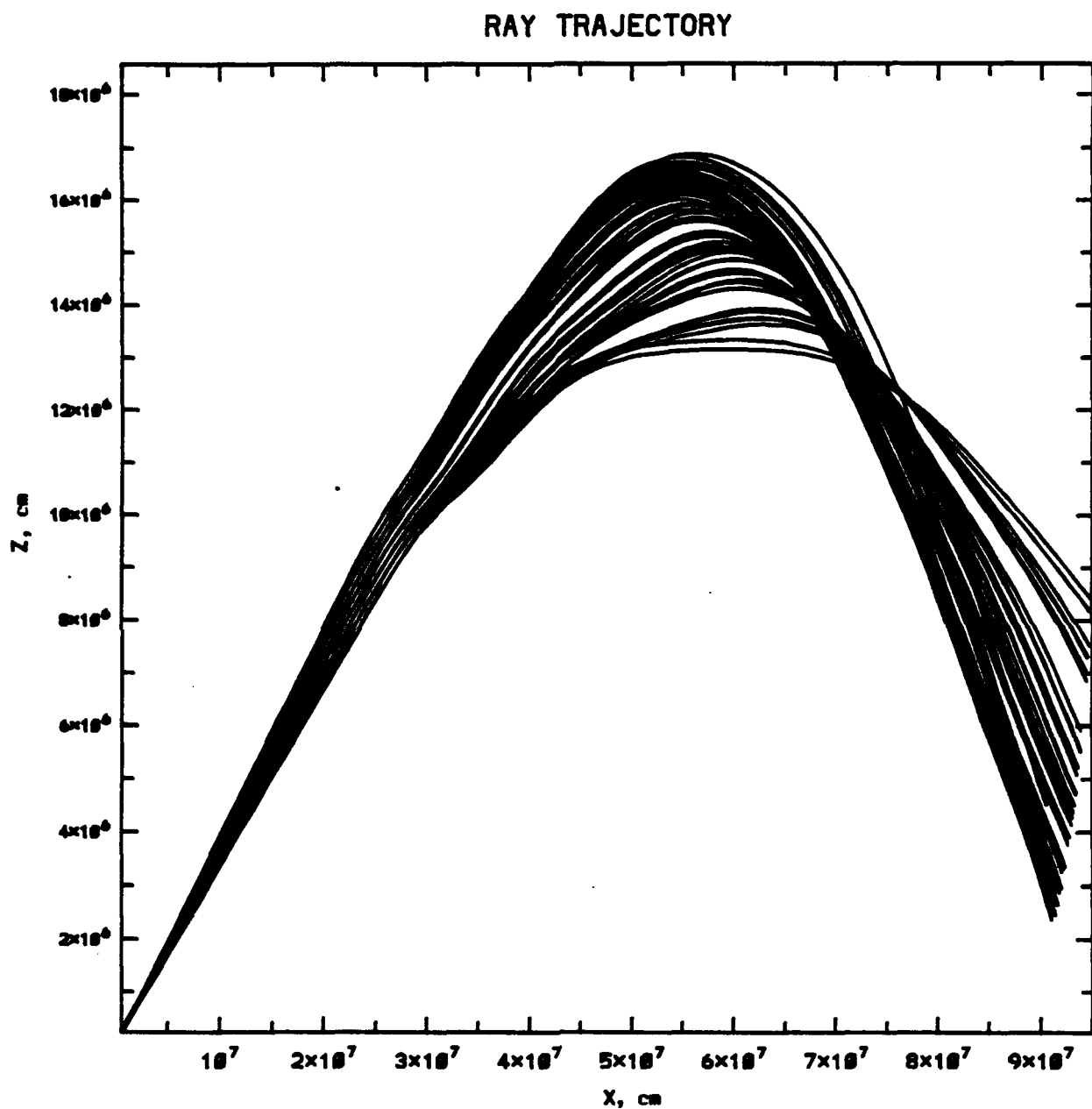


**Figure 9-2b. Ray Paths in the Y-Z Plane after Heating
for Case 0112**

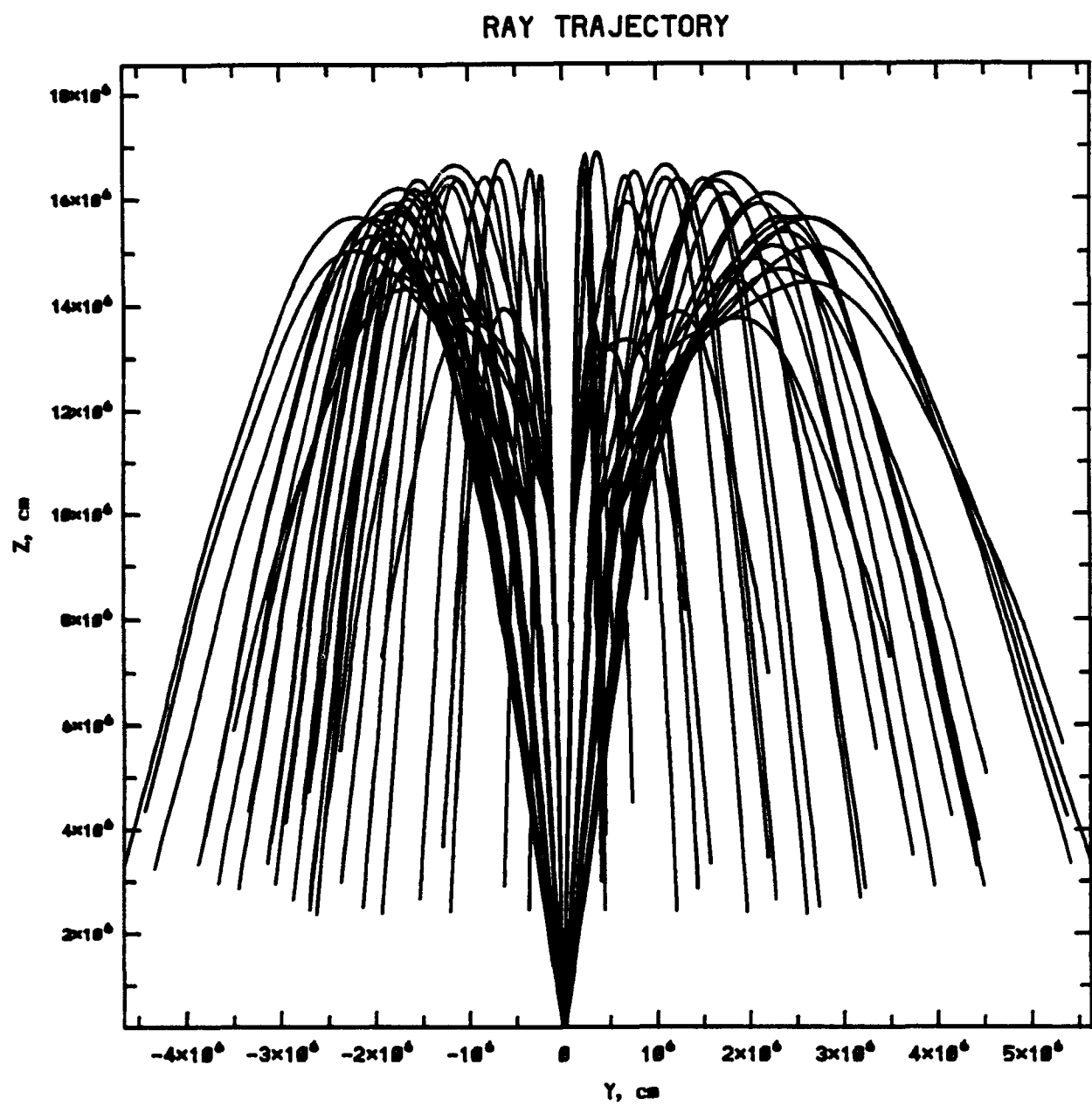


**Figure 9-2c. Ray Paths in the X-Y Plane after Heating
for Case 0112**

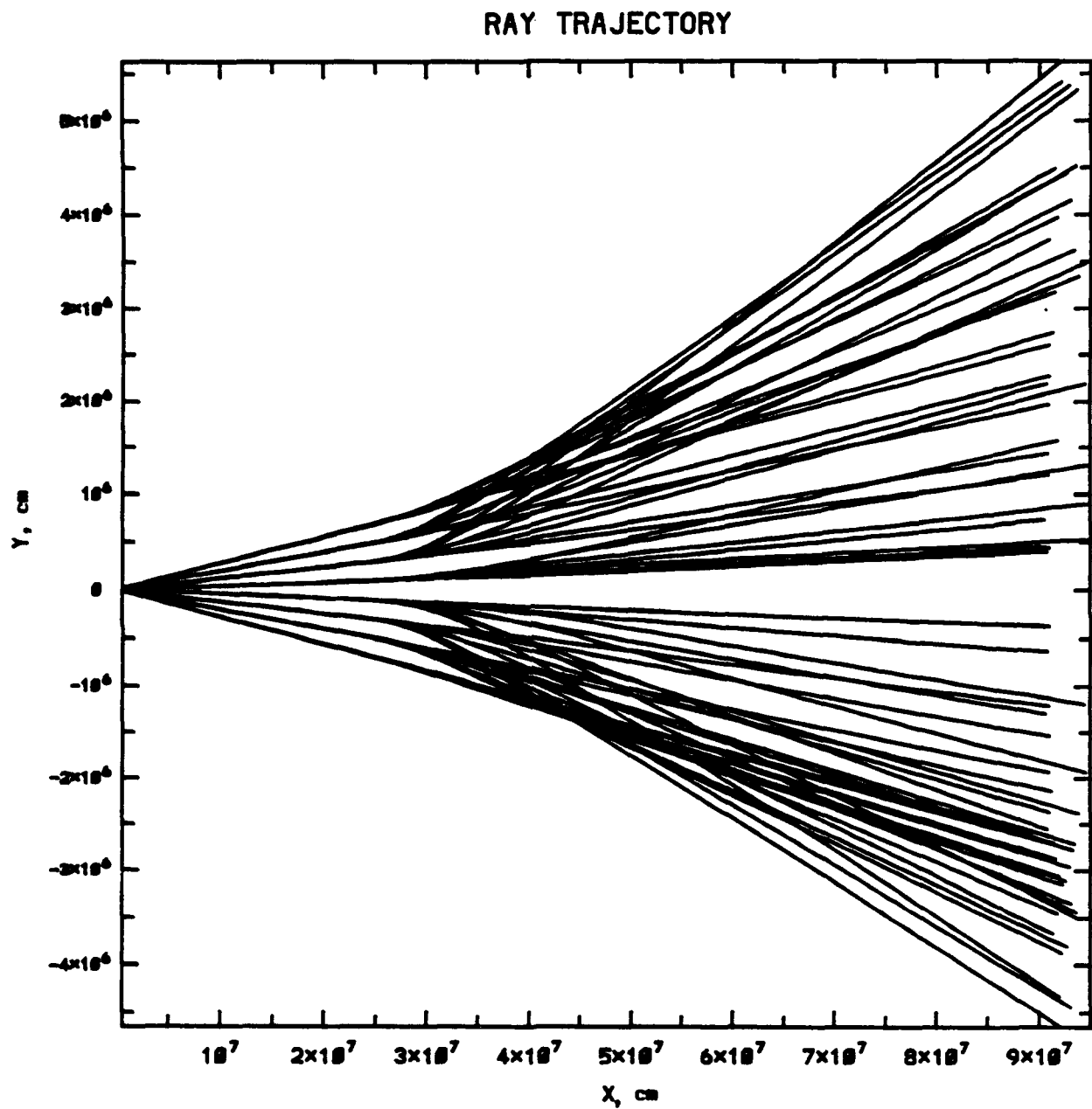


**Figure 9-3a. Electron Density Modification Contours
in the Y-Z Plane for Case 0704**

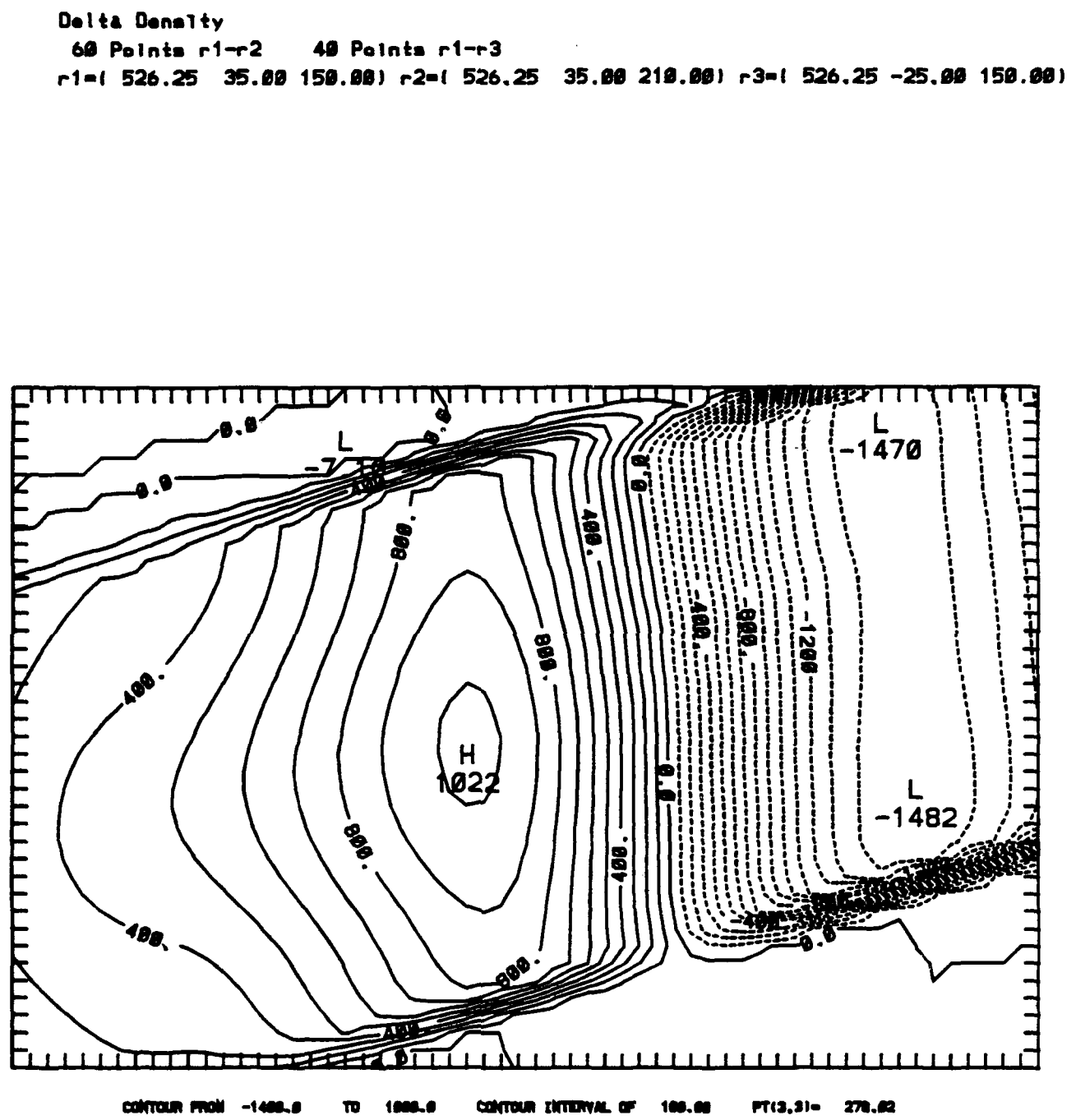
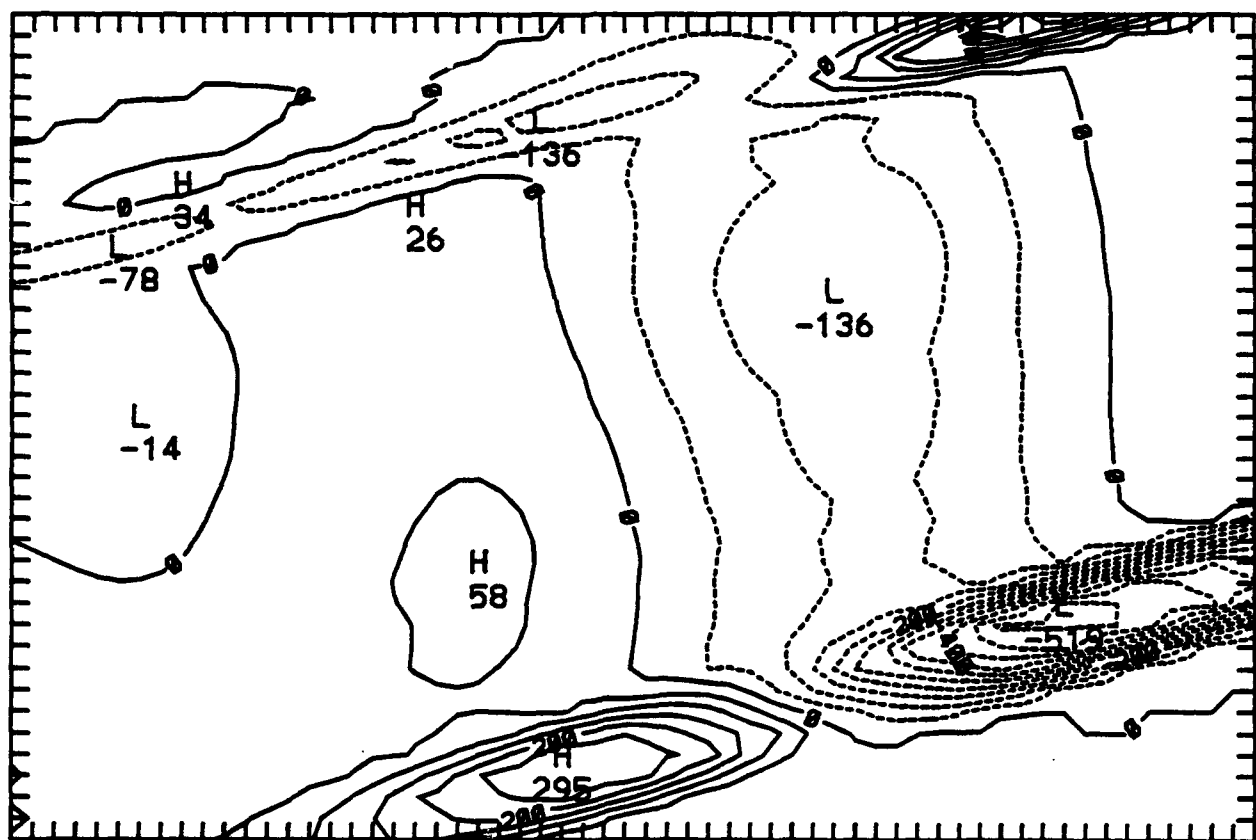


Figure 9-3b. Contours of X-Derivative of Electron Density Modification in Y-Z Plane for Case 0704

Delta Density grad x

60 Points r1-r2 48 Points r1-r3

r1=(526.25 35.00 150.00) r2=(526.25 35.00 210.00) r3=(526.25 -25.00 150.00)



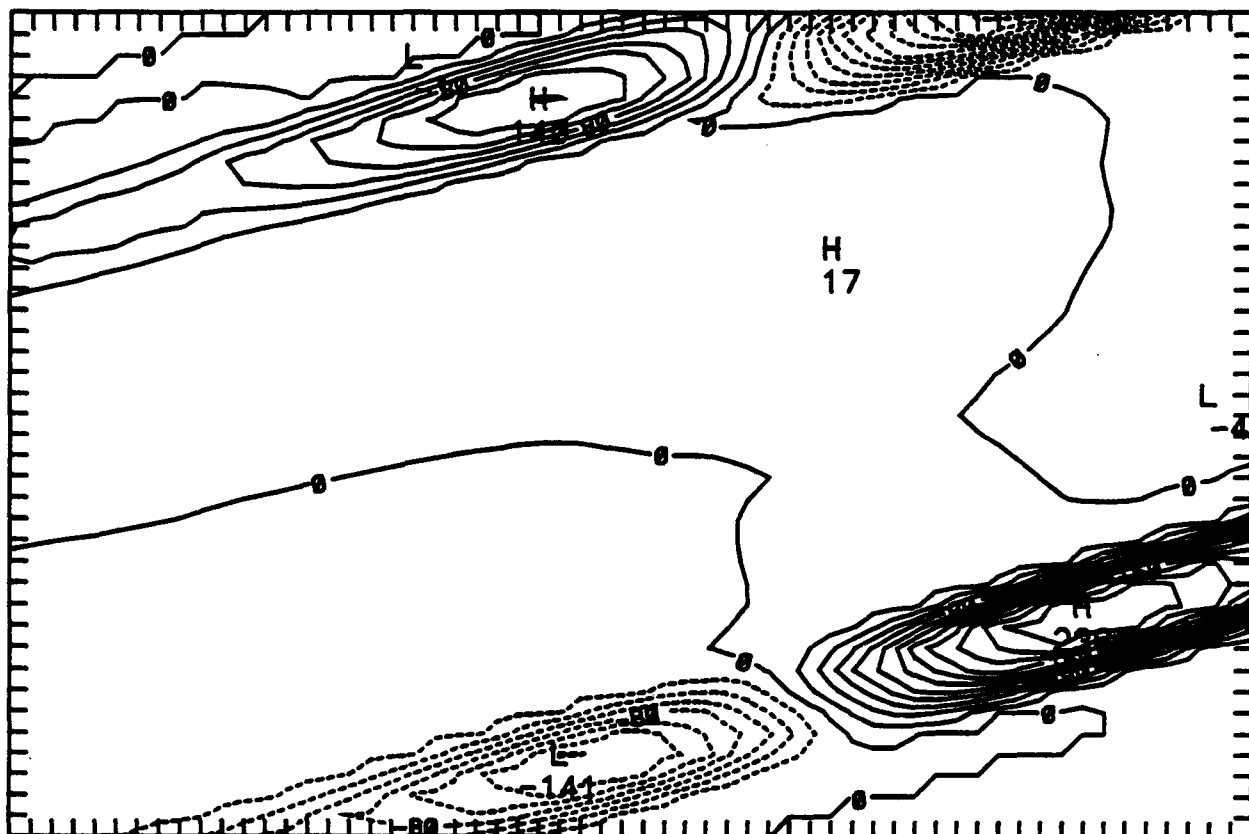
CONTOUR FROM -8.33333E-03 TO 8.33333E-03 CONTOUR INTERVAL OF 8.33333E-04 PT(3,3)= 8.11361E-04 LABELS SCALED BY 8.16666E-07

Figure 9-3c. Contours of Y-Derivative of Electron Density Modification in Y-Z Plane for Case 0704

Delta Density grad y

68 Points r1-r2 48 Points r1-r3

r1=(526.25 35.00 150.00) r2=(526.25 35.00 210.00) r3=(526.25 -25.00 150.00)



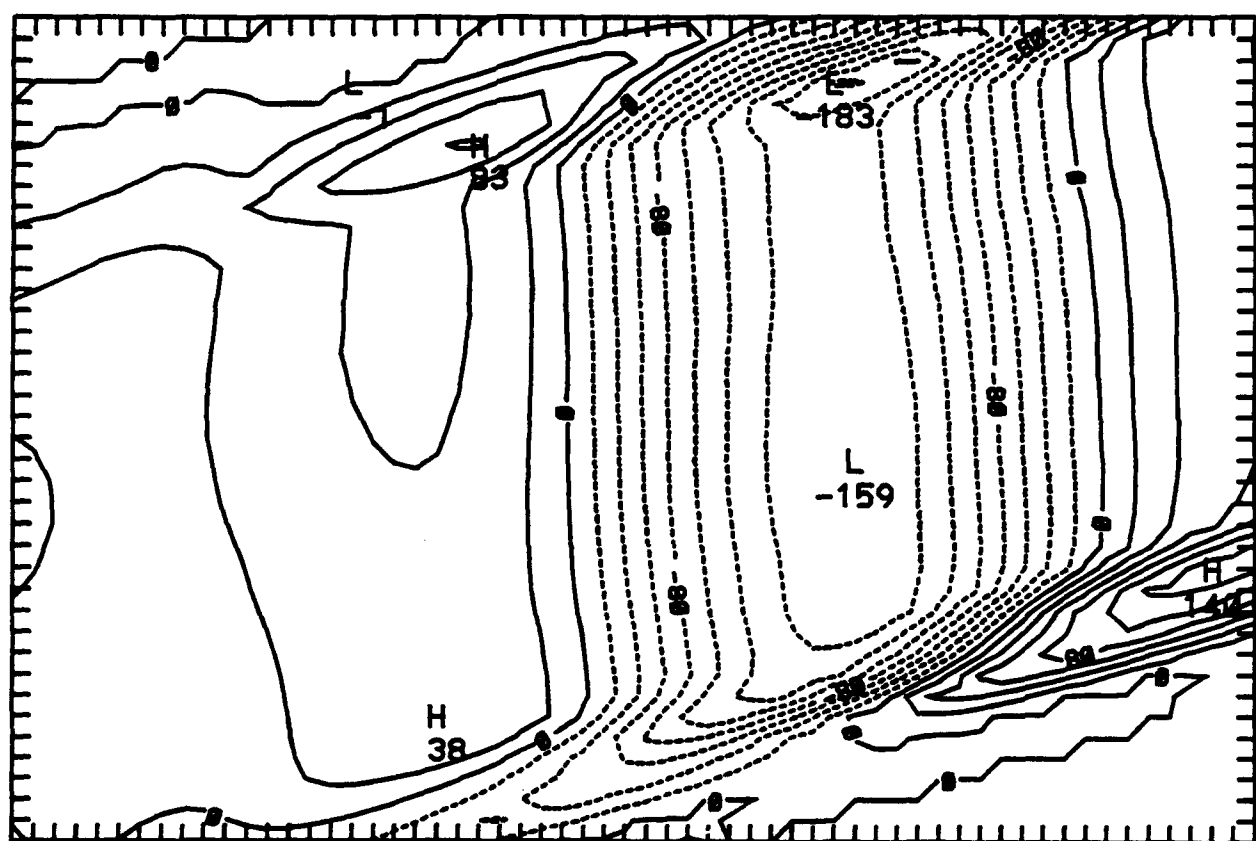
CONTOUR FROM -0.22888E-02 TO 0.22888E-02 CONTOUR INTERVAL OF 0.22888E-03 PT(3,3)= -0.64249E-04 LABELS SCALED BY 0.10000E+00

Figure 9-3d. Contours of Z-Derivative of Electron Density Modification in Y-Z Plane for Case 0704

Delta Density grad z

68 Points r1-r2 48 Points r1-r3

$r1=(526.25 \ 35.00 \ 150.00) \ r2=(526.25 \ 35.00 \ 210.00) \ r3=(526.25 \ -25.00 \ 150.00)$



CONTOUR FROM -8.16888E-02 TO 8.14888E-02 CONTOUR INTERVAL OF 8.38888E-03 PT(3,3)= 8.16888E-03 LABELS SCALED BY 8.16888E-03

**Figure 9-4a. Ray Paths in the X-Z Plane after Heating
for Case 0704**

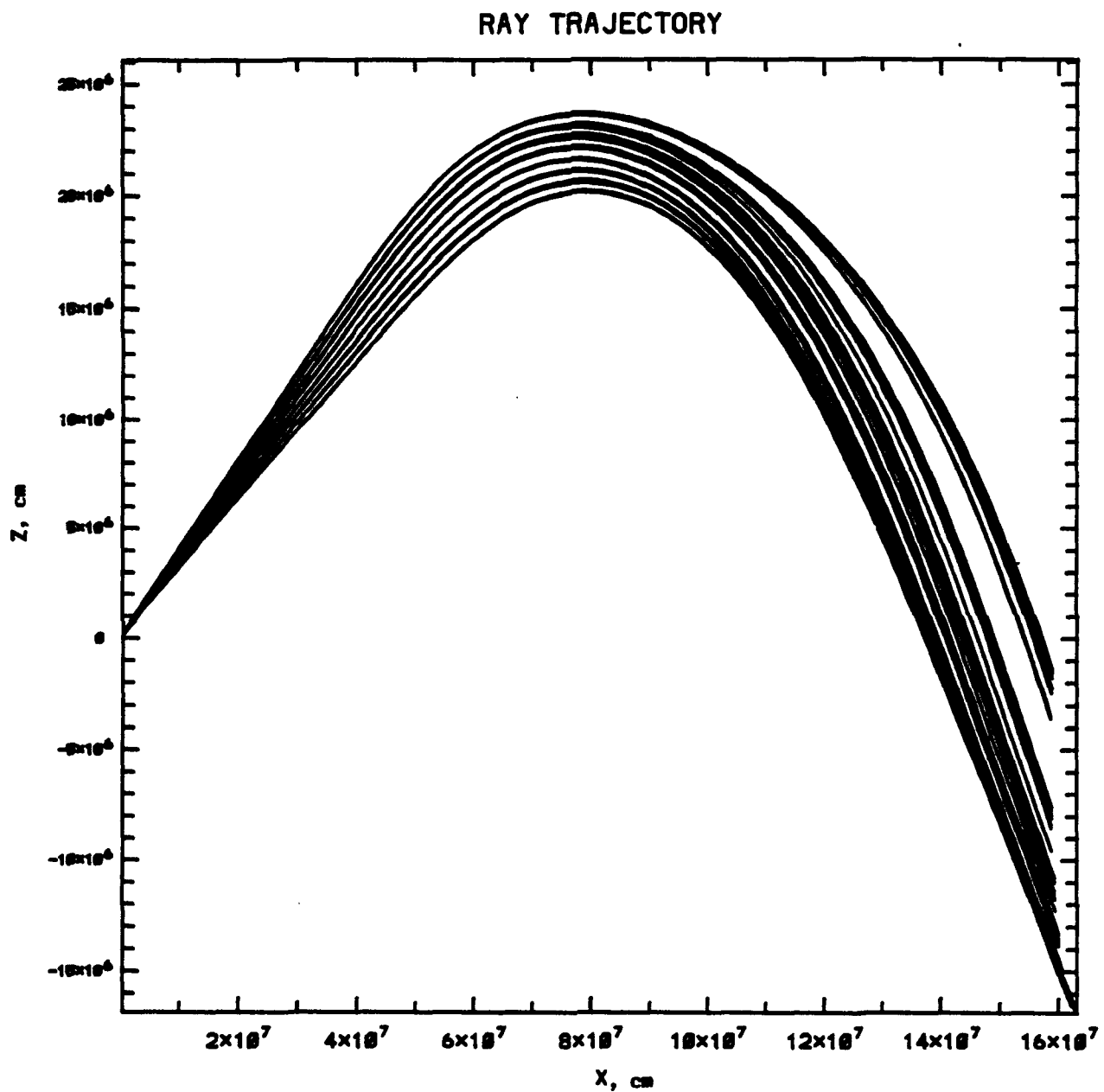


**Figure 9-4b. Ray Paths in the Y-Z Plane after Heating
for Case 0704**

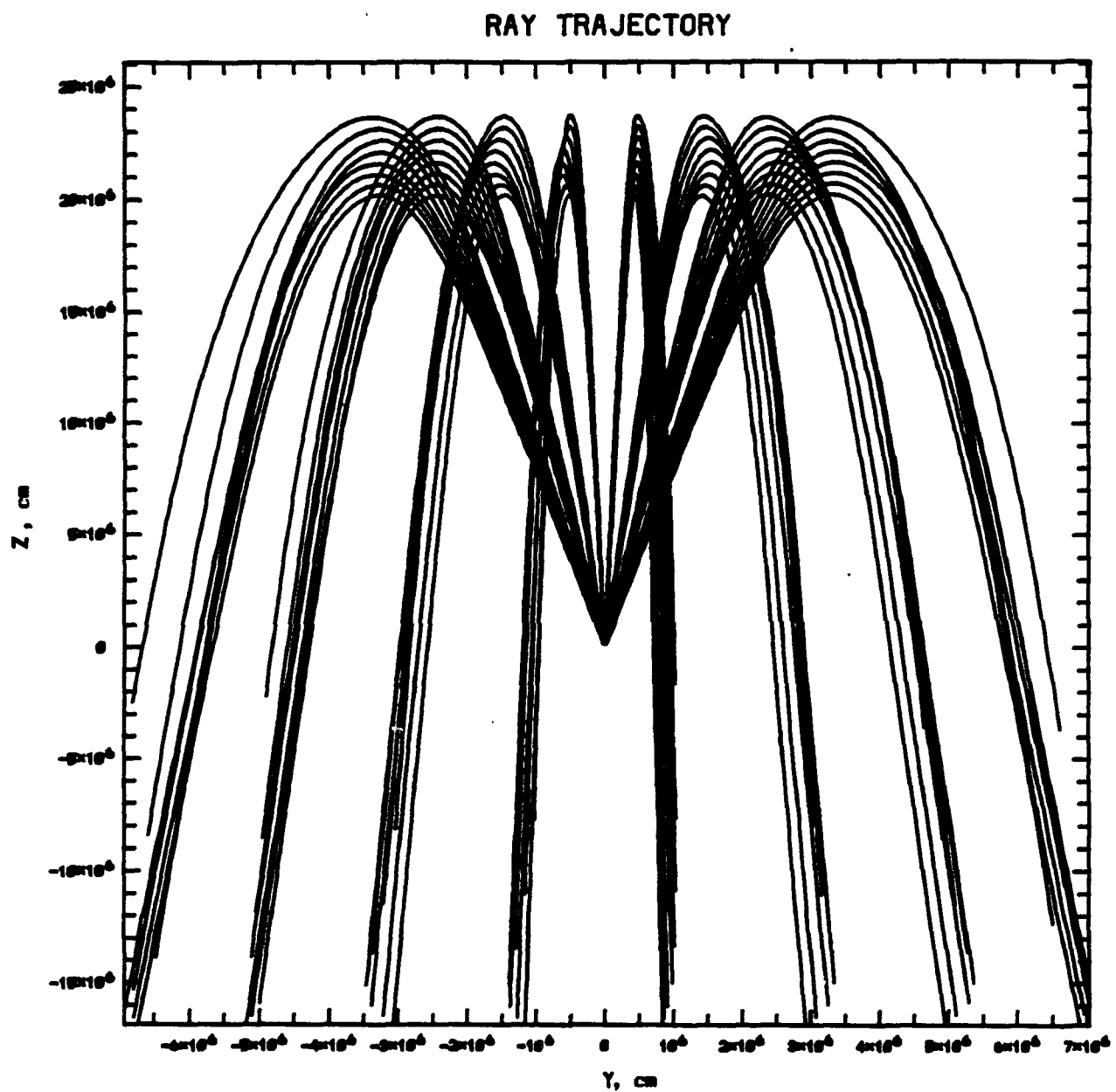
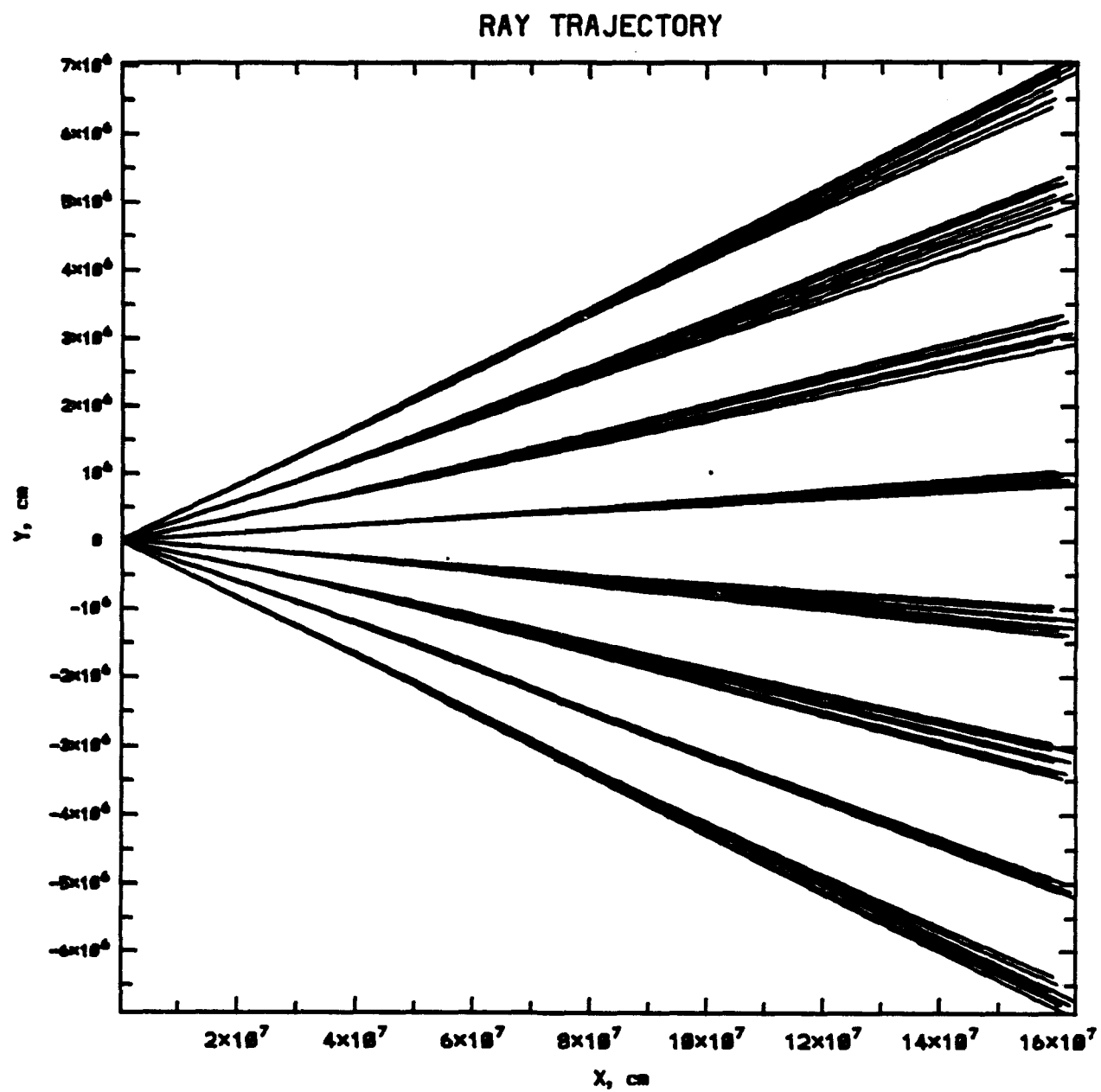


Figure 9-4c. Ray Paths in the X-Y Plane after Heating
for Case 0704



10. PROPAGATION EFFECTS ON RADAR SIGNALS

Ionospheric heating by a high power radar beam may result in strong, time-dependent refraction of the radar beam which will distort the radar footprint and introduce spurious doppler shifts in the radar signals. Self-focusing of the radar beam in the ionosphere may significantly enhance attenuation of the radar signal through ohmic dissipation. Ducting of radiation in the modified ionosphere resulting from localized heating may radically alter the propagation path. Parametric instabilities may also have important effects. They may induce ionospheric radar clutter effects due to backscattering of the primary radar signal from instability product waves, may enhance phase noise in the radar signal by dielectric fluctuation effects on forward propagation, and may cause additional, anomalous ionospheric attenuation of the primary radar signal. Furthermore, the parametric instabilities and self-focusing phenomena may interact with each other to further enhance their respective effects. A primary goal of the present endeavors is to determine the conditions under which such nonlinear phenomena can occur in ionospheric propagation, with special attention to direct ionospheric heating by the radar signal, and characterize their effects on radar signals and system performance.

When powerful HF wave signals are obliquely incident on the ionosphere two important phenomena can occur: transport and instabilities. The former issue, discussed in the previous three sections, addresses how bulk heating (caused by high incident power) changes the profiles of the background plasma. The latter pertains to the formation of plasma structures due to the onset of instabilities triggered by high incident power. For HF radar parameters, the thermal self-focusing instability is the most likely candidate.

The self-focusing of powerful radio waves has been the subject of numerous analytical and experimental investigations. During vertical HF ionospheric modification experiments performed by Duncan and Behnke^[3] in 1978 and by others later, structures were measured which drift through the illuminated HF beam at velocities between 15 to 60 m/s with a periodicity of 1 to 2 minutes (i.e., with a transverse scale size of a few kilometers). According to Perkins and Goldman^[22], in the F layer the threshold for onset of the self-focusing instability is given by

$$P_{C,F} = (1.5 \mu\text{W/m}^2) \left\{ \frac{10^6 \text{ cm}^{-3}}{n_e} \right\}^3 \left\{ \frac{T_e}{1000 \text{ K}} \right\}^4 \left\{ \frac{f}{15 \text{ MHz}} \right\}^3 C_F , \quad (1)$$

where

$$C_F = \left\{ \frac{\gamma}{10^{-1} \text{ s}^{-1}} \right\} \left\{ \frac{25 \text{ km}}{l} \right\} \left\{ \frac{\nu_{in}}{1 \text{ Hz}} \right\} . \quad (2)$$

If $10 \text{ km} \leq l \leq 50 \text{ km}$, then for $P_{C,F} = 3.48 \times 10^{-3} \text{ W/m}^2$, a value typical of the amount of power entering the F-layer at 150 km in altitude for the daytime scenario (case 0112), $6.5 \times 10^{-2} \text{ sec}^{-1} \leq \gamma \leq 3.25 \times 10^{-1} \text{ sec}^{-1}$. Thus the amount of time for the instability to develop is on the order of several seconds in the main beam region, and is shorter at higher altitudes where the electron density is larger and ion-neutral collision rates are smaller.

For the nighttime scenario, (case 0704), a typical power flux density at an altitude of 150 km near the center of the beam is $P_{C,F} = 4.57 \times 10^{-3} \text{ W/m}^2$. [Note: While the power flux density of the nighttime case is roughly equivalent to that of the daytime case,

the total amount of power crossing the meridian plane where the center of the HF beam is at 150 km in altitude is 660 kW for the nighttime case, as compared to 462 kW for the daytime case. However, the nighttime beam is slightly wider than the daytime beam ($4.5^\circ \times 4.5^\circ$ as compared to $3^\circ \times 3^\circ$), because the frequency of the nighttime scenario is 10 MHz as compared to 15 MHz for the daytime scenario, but the size of the antenna is the same for both cases. Thus the beam area is larger for case 0704 than for case 0112, which is what causes the power flux densities of the two cases to be the same order of magnitude even though the total power of the daytime case is $2/3$ that of the nighttime case.] If $10 \text{ km} \leq l \leq 50 \text{ km}$, then $8.0 \times 10^{-5} \text{ sec}^{-1} \leq \gamma \leq 4.0 \times 10^{-4} \text{ sec}^{-1}$. Thus the amount of time for the instability to develop is on the order of hours in the main beam region.

11. CONCLUSIONS

11-1. Developed Capability

The result of this work is a powerful and unique capability to numerically model the oblique propagation and heating of HF waves in the ionosphere. Geometrical optics ray tracing coupled with ionospheric E and F region transport models can self-consistently compute the nonlinear deformation of the HF beam due to heating of the ionosphere when the waves are radiated from high power, high gain transmitters. Such transmitters are found in some over-the-horizon radar systems as well as beamed short wave broadcasting stations.

The work reported here focused on developing and enhancing capabilities of a three dimensional geometrical optics ray tracing code that can propagate rays in an inhomogeneous, dissipative and anisotropic medium such as the ionosphere. The code calculates amplitude, polarization and phase of the wave fields along the rays, so that the total vector field, Poynting flux and power dissipated at a given point, or region, in the beam can be calculated. In addition, the code supports time dependence of the medium. Doppler shifts caused by temporal variations in the medium, such as drifts, are important in measurements of radar target and sea surface backscatter. Such drifts can be modeled by the code.

Similarly, the transport code enhancements focused on realistic modeling of the physics of ionospheric heating in the D, E and F regions. In order to be useful to users wanting to model a specific condition of the ionosphere, the code assumes the background ionosphere to be a given, either from empirical models such as IRI, measured ionograms at the transmitter site, or analytical profiles constructed to model specific phenomena such as drifting striations. The code then calculates the deformation of the background ionosphere caused by the ohmic dissipation of the HF beam. Changes in electron temperature and density modify the background equilibrium which in turn redistributes the ray path. This powerful prescription provides the most complete self-consistent modeling of the propagation and heating of powerful HF waves in the ionosphere currently available.

11-2. Major Findings

In order to demonstrate the capabilities of the model, sample cases were chosen to emphasize specific features that are uniquely handled by the codes.

Examples of ray tracing in an inhomogeneous and magnetized plasma were shown. When the HF beam frequency is not much higher than the electron gyrofrequency (i.e., 5 to 10 MHz) and the beam extends well into the region of high plasma frequency (reflection close to $f_o F2$), the effect of the anisotropy is significant and the beam splits into two distinct separate modes (sometimes referred to as ordinary and extraordinary modes). Under conditions where the HF beam frequency is high with respect to the electron gyrofrequency or the plasma frequency is small compared to the HF beam frequency (reflection in the lower ionosphere), the effect of the anisotropy is negligible.

Ducted modes are also of interest. Diurnal variations of the ionospheric profiles through different longitudes may cause a beam at grazing incidence to propagate for quite long distances. An example of such case was shown in our results.

A daytime heating case representative of a mid-latitude, high-sunspot number, winter

conditions was tested for heating using a powerful transmitter of about 95 dBW. The results of the transport analysis show that about 60% of the HF energy is absorbed ohmically in the lower ionosphere at the entrance point on the transmission path. Likewise, when the beam comes down from the ionosphere, high losses may be expected. The heating of the lower ionosphere causes the electron temperature to increase by over 70% and the density to increase by about 20%. Such a density enhancement can cause significant additional refraction and defocusing of the HF beam.

A similar summer nighttime case shows negligible absorption of the HF energy due to greatly reduced collisionality of the plasma. Consequently, electron temperature and density changes are also negligible. E-region transport is mainly local due to high collisionality. HF heating causes an increase in temperature which leads to an increase in density due to reduced recombination rates. In the F region, thermal conduction tends to dominate because of the absence of molecular ions which are responsible for recombination. Increase in electron temperature induces density cavities in order to relax pressure gradients.

In spite of heavy daytime absorption in the E region, F-region power densities are in excess of theoretical thresholds for thermal self-focusing instabilities. For the nighttime case, reduced absorption in the lower ionosphere is offset by the broader beamwidth resulting from selection of lower frequency with the same antenna gain. Therefore, F-region power densities in the nighttime case are comparable to those for the daytime case.

11-3. Future Work

Continuation of the work reported here may be carried out in a several directions. The research tools developed here are useful for direct simulation of HF radar systems. A detailed description of power deposition near caustic surfaces and in strong refraction zones should be developed to transcend the limitations of short-wavelength asymptotics in the wave propagation model. Some straightforward improvements in the ray tracing algorithm can lead to generally coherent phase information associated with radar waves, and this would allow the direct simulation of ionospheric effects on target and sea clutter doppler spectra in HF radars. Studies of propagation through striations may be carried out for realistic striation patterns. Cross-field transport caused by drifting striations can be accounted for by adding two dimensional effects to the transport analysis. Finally, a systematic numerical study of the thermal self-focusing instability could be carried out to explore and validate existing analytical results on the subject.

12. REFERENCES

1. *Radio Science*, Special Issue on Ionospheric Modification, **9**, 11, (1974).
2. I. J. Kantor, High Frequency Induced Enhancements of the Incoherent Scatter Spectrum at Arecibo, *J. Geophys. Res.*, **79**, 199, (1974).
3. L. M. Duncan and R. A. Behnke, Observations of Self-focusing Electromagnetic Waves in the Ionosphere, *Phys. Rev. Lett.*, **41**, 998, (1978).
4. D. T. Farley, C. LaHoz, and B. G. Fejer, Studies of the Self-focusing Instability at Arecibo, *J. Geophys. Res.*, **88**, 2093, (1983).
5. D. F. Dubois, H. A. Rose, and D. Russell, Power Spectra of Fluctuations in Strong Langmuir Turbulence, *Phys. Rev. Lett.*, **61**, 2209, (1988).
6. M. M. Shoucri, G. J. Morales, and J. E. Maggs, Ohmic Heating of the Polar F region by HF pulses, *J. Geophys. Res.*, **89**, 2907, (1984).
7. T. M. Smith, Plasma Geometric Optics Analysis and Computation, Ph. D. Dissertation, Yale University, Dec. (1983).
8. K. G. Budden, *The Propagation of Radio Waves*, Cambridge, Cambridge University Press, (1985).
9. C. M. Rush, Ionospheric Radio Propagation Models and Predictions – A Mini-Review, *IEEE Trans. Ant. and Prop.*, **AP-34**, 1163, (1986).
10. D. Bilitza, International Reference Ionosphere: Recent Developments, *Radio Sci.*, **21**, 343, (1986).
11. K. S. W. Champion, A. E. Cole, and A. J. Kantor, Standard Reference Atmospheres, Ch. 14 in *Handbook of Geophysics and the Space Environment*, A. S. Jursa ed., AFGL/AFSC, USA, (1985).
12. J. D. Hansen, Large Scale Ionospheric Modifications by High Power Radio Waves: Theory and Observation, UCLA-PPG Report No. 1298, April, (1990).
13. P. A. Bernhardt and L. M. Duncan, The Feedback-Diffraction Theory of Ionospheric Heating, *J. Atmos. and Terr. Phys.*, **44**, 1061, (1982).
14. G. P. Mantas, H. C. Carlson and C. H. LaHoz, Thermal Response of F region Ionosphere in Artificial Modification Experiments by HF Radio Waves, *J. Geophys. Res.*, **86**, 561, (1981).
15. G. Meltz and R. E. LeLevier, Heating the F Region by Deviative Absorption of Radio Waves, *J. Geophys. Res.*, **75**, 6406, (1970).
16. G. Meltz, L. H. Holway, and N. M. Tomljanovich, Ionospheric Heating by Powerful Radio Waves, *Radio Sci.*, **9**, 1049, (1974).
17. F. W. Perkins and R. G. Roble, Ionospheric Heating by Radio Waves: Predictions for Arecibo and the Satellite Power Station, *J. Geophys. Res.*, **83**, 1611, (1978).
18. R. W. Schunk and J. C. G. Walker, Theoretical Ion Densities in the Lower Ionosphere, *Planet. Space Sci.*, **21**, 1875, (1973).
19. R. W. Schunk and A. F. Nagy, Ionospheres of the Terrestrial Planets, *Rev. Geophys. Space Phys.*, **18**, 813 (1980).
20. C. G. Park and P. M. Banks, Influence of Thermal Plasma Flow on the Mid-Latitude Nighttime F₂ Layer: Effects of Electric Fields and Neutral Winds Inside the Plasmasphere, *J. Geophys. Res.*, **79**, 4661 (1974).
21. J. Douglas and B. F. Jones, On Predictor-Corrector Methods for Nonlinear Parabolic Differential Equations, *SIAM J. Appl. Math.*, **11** 195 (1963).

22. F. W. Perkins and M. V. Goldman, Self-Focusing of Radio Waves in an Underdense Ionosphere, *J. Geophys. Res.* **86**, 600 (1981).
23. P. M. Banks and G. Kockarts, Aeronomy, Parts A and B, Chapters 1, 9, 22, pp. 1, 184, 238, Academic Press, New York, 1973.
24. M. H. Rees and R. G. Roble, Observations and Theory of the Formation of Stable Auroral Red Arcs, *Rev. Geophys. Space Phys.* **13**, 201 (1975).
25. R. W. Schunk and A. F. Nagy, Electron Temperatures in the F Region of the Ionosphere: Theory and Observations, *Rev. Geophys. Space Phys.* **16**, 355 (1978).

APPENDIX A. COLLISIONAL RATES

The following is a summary of the collisional rates used in the transport model with reference to where they were obtained.

1. Electron-Neutral Collision:

a. (Ref. 23, 25)

$$\nu_{e,N_2} = 2.33 \times 10^{-11} n(N_2) [1 - 1.21 \times 10^{-4} T_e] T_e \text{ s}^{-1} .$$

b. (Ref. 23, 25)

$$\nu_{e,O_2} = 1.82 \times 10^{-10} n(O_2) [1 + .036 T_e^{1/2}] T_e^{1/2} \text{ s}^{-1} .$$

c. (Ref. 24)

$$\nu_{e,O} = 2.65 \times 10^{-10} n(O) T_e^{1/2} \text{ s}^{-1} .$$

d. (Ref. 23, 25)

$$\nu_{e,He} = 4.6 \times 10^{-10} n(He) T_e^{1/2} \text{ s}^{-1} .$$

e. (Ref. 23, 25)

$$\nu_{e,H} = 4.35 \times 10^{-9} n(H) [1 - 1.35 \times 10^{-4} T_e] T_e^{1/2} \text{ s}^{-1} .$$

2. Ion-Neutral Collisions

a. (Ref. 23, 25)

$$\nu_{O^+,N_2} = 6.82 \times 10^{-10} n(N_2) \text{ s}^{-1} .$$

b. (Ref. 23, 25)

$$\nu_{O^+,O_2} = 6.64 \times 10^{-10} n(O_2) \text{ s}^{-1} .$$

c. (Ref. 23, 25)

$$\nu_{O^+,O} = 3.67 \times 10^{-11} n(O) [(T_i + T_n)/2]^{1/2} \{1.0 - .064 \log_{10} [(T_i + T_n)/2]\}^2 \text{ s}^{-1} .$$

d. (Ref. 23, 25)

$$\nu_{O^+,He} = 1.32 \times 10^{-10} n(He) \text{ s}^{-1} .$$

e. (Ref. 25)

$$\nu_{O^+, H} = 4.13 \times 10^{-12} n(H) T_i^{1/2} [1.0 - .047 \log_{10}(T_i)]^2 \text{ s}^{-1} .$$

f. (Ref. 23, 25)

$$\nu_{O_2^+, N_2} = 4.13 \times 10^{-10} n(N_2) \text{ s}^{-1} .$$

g. (Ref. 25)

$$\begin{aligned} \nu_{O_2^+, O_2} &= 2.59 \times 10^{-11} n(O_2) [(T_i + T_n)/2]^{1/2} \\ &\{1.0 - .073 \log_{10}[(T_i + T_n)/2]\}^2 \text{ s}^{-1} . \end{aligned}$$

h. (Ref. 23, 25)

$$\nu_{O_2^+, O} = 2.31 \times 10^{-10} n(O) \text{ s}^{-1} .$$

i. (Ref. 23, 25)

$$\nu_{O_2^+, He} = 7.0 \times 10^{-11} n(He) \text{ s}^{-1} .$$

j. (Ref. 23, 25)

$$\nu_{O_2^+, H} = 6.5 \times 10^{-11} n(H) \text{ s}^{-1} .$$

k. (Ref. 23, 25)

$$\nu_{NO^+, N_2} = 4.34 \times 10^{-10} n(N_2) \text{ s}^{-1} .$$

l. (Ref. 25)

$$\nu_{NO^+, O_2} = 4.27 \times 10^{-10} n(O_2) \text{ s}^{-1} .$$

m. (Ref. 23, 25)

$$\nu_{NO^+, O} = 2.44 \times 10^{-10} n(O) \text{ s}^{-1} .$$

n. (Ref. 23, 25)

$$\nu_{NO^+, He} = 7.4 \times 10^{-11} n(He) \text{ s}^{-1} .$$

o. (Ref. 23, 25)

$$\nu_{NO^+, H} = 6.9 \times 10^{-11} n(H) \text{ s}^{-1} .$$

3. Electron-Ion Collisions

a. (Ref. 23, 24, 25)

$$\nu_{e,i} = \frac{54.5 n_i}{T_e^{3/2}} \text{ s}^{-1} .$$

APPENDIX B. ELECTRON COOLING RATES

The following is a summary of the electron cooling rates used in the transport model with reference to where they were obtained.

A. Cooling due to translational electron-neutral interactions

1. (Ref. 24, 25)

$$L_e(e, N_2) = 1.77 \times 10^{-19} n_{eN}(N_2) [1 - 1.21 \times 10^{-4} T_e] T_e (T_e - T_n) \text{ eV cm}^{-3} s^{-1}$$

2. (Ref. 24, 25)

$$L_e(e, O_2) = 1.21 \times 10^{-18} n_{eN}(O_2) [1 + .036 T_e^{1/2}] T_e^{1/2} (T_e - T_n) \text{ eV cm}^{-3} s^{-1}$$

3. (Ref. 25)

$$L_e(e, O) = 7.9 \times 10^{-19} n_{eN}(O) T_e^{1/2} (T_e - T_n) [1 + 5.7 \times 10^{-4} T_e] \text{ eV cm}^{-3} s^{-1}$$

4. (Ref. 24, 25)

$$L_e(e, H) = 9.63 \times 10^{-16} n_{eN}(H) T_e^{1/2} (T_e - T_n) [1 - 1.35 \times 10^{-4} T_e] \text{ eV cm}^{-3} s^{-1}$$

5. (Ref. 24, 25)

$$L_e(e, He) = 2.46 \times 10^{-17} n_{eN}(He) T_e^{1/2} (T_e - T_n) \text{ eV cm}^{-3} s^{-1}$$

B. Cooling due to rotational excitation of N_2 and O_2

1. (Ref. 24, 25)

$$L_e(e, N_{2\text{rot}}) = 2.9 \times 10^{-14} n_{eN}(N_2) (T_e - T_n) T_e^{-1/2} \text{ eV cm}^{-3} s^{-1}$$

2. (Ref. 23, 24, 25)

$$L_e(e, O_{2\text{rot}}) = 6.9 \times 10^{-14} n_{eN}(O_2) (T_e - T_n) T_e^{-1/2} \text{ eV cm}^{-3} s^{-1}$$

C. Cooling due to vibrational excitation of N_2 and O_2

1. (Ref. 25)

$$L_e(e, N_{2\text{vib}}) = 2.99 \times 10^{-12} n_{eN}(N_2) \exp[f(T_e - 2000)/(2000 T_e)]$$

$$\begin{aligned}
& \times \{[1 - \exp[g(T_n - T_e)/(T_e T_n)]\} \text{ } eV cm^{-3} s^{-1} \\
f & \equiv 1.06 \times 10^4 + 7.51 \times 10^3 \tanh[1.1 \times 10^{-3}(T_e - 1800)] \\
g & \equiv 3300 + 1.233(T_e - 1000) - 2.056 \times 10^{-4}(T_e - 1000)(T_e - 4000).
\end{aligned}$$

2. (Ref. 25)

$$\begin{aligned}
L_e(e, O_2 \text{vib}) &= 5.196 \times 10^{-13} n_e n(O_2) \exp[h(T_e - 700)/(700 T_e)] \\
&\times \{1 - \exp[2770(T_n - T_e)/(T_e T_n)]\} \text{ } eV cm^{-3} s^{-1} \\
h &\equiv 3300 - 839 \sin[1.91 \times 10^{-4}(T_e - 2700)].
\end{aligned}$$

D. Cooling due to fine structure excitation of O

1. (Ref. 25)

$$\begin{aligned}
L_e(e, O^3P) &= 8.629 \times 10^{-6} \frac{n_e n(O)}{Z} \sum_{i=1}^3 A_i (B!)_i T_e^{[B_i - 1/2]} \{ \epsilon_i (D_i - E_i) + 5.91 \times 10^{-9} \\
&\times (T_n - T_e) [(1 + B_i) D_i + (\frac{(EE)_i}{T_e} + 1 + B_i) E_i] \} \text{ } eV cm^{-3} s^{-1}
\end{aligned}$$

where

$$\epsilon_i = .02 \text{ (i = 1), } .028 \text{ (i = 2), } .008 \text{ (i = 3)}$$

$$D_i = \exp[-228/T_n] \text{ (i = 1), } \exp[-326T_n] \text{ (i = 2), } \exp[-326T_n] \text{ (i = 3)}$$

$$\begin{aligned}
E_i &= \exp[-228/T_e] \text{ (i = 1), } \exp[-326T_e] \text{ (i = 2), } \\
&\exp[-98/T_e - 228T_n] \text{ (i = 3)}
\end{aligned}$$

$$(EE)_i = 228 \text{ (i = 1), } 326 \text{ (i = 2), } 98 \text{ (i = 3)}$$

$$A_i = 8.58 \times 10^{-6} \text{ (i = 1), } 7.201 \times 10^{-6} \text{ (i = 2), } 2.463 \times 10^{-7} \text{ (i = 3)}$$

$$B_i = 1.019 \text{ (i = 1), } .8998 \text{ (i = 2), } 1.268 \text{ (i = 3)}$$

$$(B!)_i = 1.019 \text{ (i = 1), } .9169 \text{ (i = 2), } 1.1626 \text{ (i = 3)}$$

with

$$Z \equiv 5 + 3e^{-228/T_n} + e^{-326/T_n}$$

E. Cooling due to electronic excitation of O and O₂

1. (Ref. 25)

$$\begin{aligned}
L_e(e, O(^1D)) &= 1.57 \times 10^{-12} n_e n(O) \exp[d(T_e - 3000)/(3000 T_e)] \\
&\times \{1 - \exp[22,713(T_n - T_e)/(T_e T_n)]\} \text{ } eV cm^{-3} s^{-1},
\end{aligned}$$

where

$$d \equiv 2.4 \times 10^{-4} + 0.3(T_e - 1500) .$$

2. (Ref. 25)

$$L_e(e, O_2(^1\Delta_g)) = 1.143 \times 10^{-14} n_e n(O_2) \exp[f(T_e - 1500)/(1500T_e)] \\ \times \{1 - \exp[11,400(T_n - T_e)/(T_e T_n)]\} \text{ eV cm}^{-3} s^{-1} ,$$

where

$$f \equiv \{13,200 + 1410 \sin[.000241(T_e - 500)]\} \times \{1 + \exp[(T_e - 14,011)/1048]\} .$$

3. (Ref. 25)

$$L_e(e, O_2(^1\Sigma_g)) = 1.616 \times 10^{-16} n_e n(O_2) \exp[g(T_e - 1500)/(1500T_e)] \\ \times \{1 - \exp[11,400(T_n - T_e)/(T_e T_n)]\} \text{ eV cm}^{-3} s^{-1} ,$$

where

$$g \equiv \{19,225 + 560 \sin[.000383(T_e - 1000)]\} \times \{1 + \exp[(T_e - 16,382)/1760]\} .$$

APPENDIX C. CONFERENCE PRESENTATIONS

The following presentations and publications have resulted from contract sponsorship.

1. Modeling of High Frequency Propagation and Heating in the Ionosphere, AGARD Conference on Ionospheric Modification and Its Potential to Enhance or Degrade the Performance of Military Systems, Electromagnetic Wave Propagation Panel Symposium, Bergen, Norway, 28 - 31 May, 1990.
2. Modeling of High Frequency Propagation and Heating in the Ionosphere, in AGARD Conference Proceedings No. 485 on Ionospheric Modification and Its Potential to Enhance or Degrade the Performance of Military Systems, NTIS, Springfield, VA, 1990.
3. Oblique Ionospheric Heating by HF Waves, 1991 North American Radio Science Meeting, Commission H - Ionospheric Heating and Modification, London, ONT, Canada, June 24 - 28, 1991.
4. Oblique Ionospheric Heating by HF Waves, Annual Meeting of the American Physical Society, Division of Plasma Physics, Tampa, FL, November 4 - 8, 1991.
5. Modeling of High Frequency Propagation and Heating in the Ionosphere, Over-the-Horizon Radar Technology Conference, Electronic Systems Division and Rome Laboratories, Hanscom AFB, MA, November 5 - 7, 1991.

APPENDIX D. COMPUTER CODES

**To obtain further information concerning the computer codes (Appendix D)
for this report, contact:**

**RL (ERCP/Stanford Yukon)
Hanscom AFB MA 01731-5000**

(617) 893-5353

MISSION
OF
ROME LABORATORY

Rome Laboratory plans and executes an interdisciplinary program in research, development, test, and technology transition in support of Air Force Command, Control, Communications and Intelligence (C³I) activities for all Air Force platforms. It also executes selected acquisition programs in several areas of expertise. Technical and engineering support within areas of competence is provided to ESD Program Offices (POs) and other ESD elements to perform effective acquisition of C³I systems. In addition, Rome Laboratory's technology supports other AFSC Product Divisions, the Air Force user community, and other DOD and non-DOD agencies. Rome Laboratory maintains technical competence and research programs in areas including, but not limited to, communications, command and control, battle management, intelligence information processing, computational sciences and software producibility, wide area surveillance/sensors, signal processing, solid state sciences, photonics, electromagnetic technology, superconductivity, and electronic reliability/maintainability and testability.